UNIVERSITÄT BAYREUTH

Universität Bayreuth
Fakultät für Mathematik, Physik und Informatik
Biofluid Simulation and Modeling

Masterarbeit

zur Erlangung des akademischen Grades

Master of Science (M. Sc.)

Simulation of Stem Cells in Shear Thinning Bioinks

Vorgelegt von	Sebastian Johannes Müller
am	7. September 2018
Matrikelnummer	1277447

Erstprüfer	Prof. Dr. Stephan Gekle
Zweitprüfer	Prof. Dr. Walter Zimmermann

Zusammenfassung

Mit dem weltweit zunehmenden Bedarf an Transplantationen von Organen und Gewebe ist die Entwicklung von Behandlungsmethoden der regenerativen Medizin eine der großen Herausforderungen dieser Zeit. Eine vielversprechende Methode zur Herstellung von biologischem Gewebe bietet die additive Fertigung, d. h. der 3D-Druck von Gewebe oder Organen.
Mit speziellen Drucktechniken und darauf zugeschnittenen Biotinten – Mischungen aus Flüssigkeiten mit bestimmten Eigenschaften und Zellen – können dreidimensionale Strukturen automatisiert nach vorgefertigtem Muster hergestellt werden. Neben biochemischen Aspekten der Biotinten, beispielsweise ihrer Verträglichkeit mit den Zellen, spielen auch rheologische Eigenschaften eine wichtige Rolle: Während des Druckvorgangs treten hydrodynamische Kräfte auf, die die Zellen beschädigen oder gar zerstören können, noch bevor sie in die 3D-Struktur eingebaut werden.
Die in der Strömung auftretenden Scherkräfte sind vor allem in der Druckerdüse relevant, da die Flüssigkeit einen Übergang von festen zu freien Randbedingungen durchläuft und sich das Strömungsprofil stark ändert. Um nun die Strömungsprofile innerhalb und außerhalb der Düse anzugleichen und damit die Unterschiede am Übergang zu minimieren, können scherverdünnende Flüssigkeiten als Medium für die Zellen eingesetzt werden. Treten hohe Schergradienten auf, wie etwa an der Innenseite eines Kanals, verringert sich die Viskosität dieser Fluide, wodurch sie besser fließen. Sind die Schergradienten hingegen klein, wie in der Mitte der Strömung, steigt die Viskosität an und der Fluss wird gebremst. Dadurch entsteht ein breites Strömungsprofil, bei dem die Scherkräfte für Zellen in der Kanalmitte abnehmen.
Die Deformation der Zellen vor und während des Druckvorgangs ist experimentell nur schwer erfassbar und außerdem müssten sehr viele Experimente für verschiedene Zelltypen und Biotinten-Mischungen durchgeführt werden.
An dieser Stelle kann die Simulation des Systems hilfreich sein. Reduziert auf die wesentlichen Bestandteile, die rheologischen Eigenschaften des Fluids und die elastischen Eigenschaften der Zellen, kann das Verhalten von Zellen in Biotinten im Detail untersucht werden.

Im Rahmen dieser Masterarbeit wird die Simulationssoftware ESPResSo daher um einige scherverdünnende Viskositätsmodelle erweitert. Die darin implementierte *Lattice Boltzmann Methode* bietet dabei den Vorteil, dass lokal Scherraten berechnet werden können und die Parallelisierbarkeit des Algorithmus nicht beeinträchtigt wird. Außerdem wird ebenso die GPU-Implementierung um die Viskositätsmodelle erweitert, da diese gerade für kleinere Systeme erheblich schneller ist.
Um die Methode zu validieren, werden analytische Lösungen der Navier-Stokes-Gleichungen für das *power-law* und das *truncated power-law* Modell hergeleitet und die

Simulationsdaten anschließend damit verglichen.
Daraufhin werden Simulationen von kugelförmigen Zellen, die Stammzellen repräsentieren sollen, in einem zylindrischen Kanal mit scherverdünnendem Fluid durchgeführt und das Flussverhalten sowie die Verformung der Zellen mit mehreren Methoden analysiert. Es stellt sich heraus, dass die mittlere Deformation der Zellen entgegen der ursprünglichen Annahme mit zunehmender Scherverdünnung ebenfalls zunimmt. Der erwartete Effekt tritt hingegen nur für sehr hohe Scherverdünnung auf und auch nur dann, wenn die gesamte Zelle im Plateau-Bereich der Strömung liegt. Sobald die Zelle weiter von der Mitte abweicht, wird sie mindestens so stark deformiert wie in einem Newtonschen Fluid. Das liegt unter anderem daran, dass die Scherraten zum Rand des Kanals hin deutlich höher werden, wenn das Strömungsprofil ein zentrales Plateau besitzt.
Abschließend werden Simulationen durchgeführt, die den Übergang an der Düse eines 3D-Druckers modellieren sollen. Durch die Kombination von festen und freien Randbedingungen wird so zunächst das Strömungsprofil am Übergang betrachtet. Daraufhin wird eine einzelne sphärische Zelle mit unterschiedlichen radialen Startpositionen für verschiedene Scherverdünnungen simuliert und die Verformung analysiert. Auch hier ergibt sich dasselbe Bild – je höher die Scherverdünnung, desto mehr wird die Zelle am Übergang deformiert. Auch Zellen in der Kanalmitte, die vor dem Austritt aus der Düse weniger verformt sind, werden während des Übergangs für höhere Scherverdünnung stärker deformiert. Nach dem Übergang benötigen diese Zellen auch erheblich länger, um in ihre ursprüngliche Form zu relaxieren. Letztes ist auf das verwendete Viskositätsmodell zurückzuführen, da die Viskosität hinter dem Übergang für scherverdünnendere Flüssigkeiten grundsätzlich höher ist. Die höhere Deformation lässt sich in diesem Simulationssetup nur auf das Verhältnis von viskosen Fluidkräften zu elastischen Zellkräften zurückführen. Auch wenn die Unterschiede im Strömungsprofil für höhere Scherverdünnung kleiner sind, so sind dennoch radiale Strömungen vorhanden, die an der Zelle ziehen. Da die Kapillarzahl in diesen Fällen bis zu doppelt so groß ist als im Newtonschen Fluid, wird die Zelle dementsprechend stärker verformt. Diese Effekte werden voraussichtlich geringer, wenn der Kanal erheblich breiter gewählt wird und dadurch die radiale Strömung am Übergang auf den Rand konzentriert wird.
Es wird also gezeigt, dass die Deformation der Zellen in einer scherverdünnenden Flüssigkeit wie erwartet abnimmt, wenn sie mittig genug, d. h. im Plateau-Bereich der Strömung, fließen. Am Übergang einer Druckerdüse hingegen werden die Zellen signifikant stärker verformt als es in einem Newtonschen Fluid der Fall wäre.

Alle Simulationen in dieser Arbeit wurden mit der erweiterten Version von ESPResSo [1] gerechnet, Bilder aus den Simulationen wurden mit *ParaView* [2] erstellt und mit der Bildbearbeitungssoftware *GIMP* [3] bzw. mit dem LaTeX-Paket *TikZ* arrangiert. Datenanalyse wurde mit eigenen Skripten betrieben oder mit Funktionen der Software *Gnuplot* [4]. *Gnuplot* wurde weiterhin verwendet, um alle Plots zu erstellen.

Summary

Facing the world's growing demand on tissue and organ transplants, the research and development of methods of treatment in the field of regenerative medicine is a great challenge of our time. Very promising among techniques to fabricate biological tissues are additive manufacturing processes, i. e. the 3D printing of organs and tissues.
Special printing methods and tailored bioinks, i. e. mixtures of cells and fluids with certain properties, allow the fabrication of three dimensional structures in a reproducible, controlled and automated manner. Besides biochemical properties of these inks, e. g. their compatibility with living cells, the rheological properties play an important role: Hydrodynamic forces occurring during the printing process can damage or even destroy the cell before it is incorporated into the 3D structure.
Those shear forces are especially present inside the printer nozzle, where a transition from no-slip to free-slip boundary conditions happens and, thus, the flow profile strongly changes. To now level the different flow profiles in front of and behind the nozzle, fluids with shear thinning properties can be utilized as media for the cell. For these liquids, large shear rates result in a low viscosity, making the fluid flow better in the vicinity of a channel wall. Small shear rates, instead, make the fluid increasingly viscous and decelerate the flow in the channel center. Altogether, this results in a broad velocity profile, which reduces the shear forces for cells in the channel center.
Measuring cell deformations during a real printing process is challenging and would require a lot of experiments with different cell types and bioink formulations. At this point, simulations can help to look closely inside the system. Reducing the system to its geometry, the rheological model for the fluid and the elastic model for the cell, the behavior of cells in bioinks can be studied in detail.

Therefore, the simulation software ESPResSo has been extended with several shear thinning viscosity models during this thesis. Using the *Lattice Boltzmann method*, it is possible to calculate shear rates locally and, thus, the extension does not affect its advantageous parallelization capability. Furthermore, the respective GPU version has been extended, providing immense simulation speed up – especially for smaller systems.
For validating this method, analytical solutions to the Navier-Stokes equations are derived using the *power-law* and the *truncated power-law* viscosity model to subsequently compare them with the simulated data.
Afterwards, spherical cells – representing stem cells – are simulated in a cylindrical channel containing shear thinning fluid. The flow behavior and the cell deformation are investigated using different methods. Contrary to the primary assumption, it appears that the average deformation of the cell increases with increasing shear thinning strength. The expected effect, however, is solely observed for high shear thinning and centered cells. As the cell deviates from a central position, it deforms at least as much as in a Newtonian

fluid. That is a consequence of the higher shear rates near the channel wall and those, in turn, stem from the broad velocity profile.
Finally, simulations are performed in a system modeling a 3D printer nozzle. Combining both no-slip and free-slip boundary algorithms, the flow is studied at the transition. Afterwards, a spherical cell is included, starting at different radial offsets in the channel, and its deformation is analyzed with respect to the shear thinning strength of the liquid. The same behavior as before is observed – the higher the shear thinning, the greater deforms the cell during the transition. Even in the channel center, where the cell is significantly less deformed in front of the transition, it is stretched more in lateral direction while passing through it. The relaxation towards the cell's original shape after the transition also takes longer, which is a consequence of the incorporated viscosity model that causes large viscosities to occur in the free-slip region. The greater deformation during the transition, however, can be explained considering the ratio of viscous fluid forces and the cell's elastic restoring forces in this simulation setup. Although the flow profiles in front of and behind the transition are more similar for increased shear thinning, there exist radial flow components pulling on the cell. Due to the capillary number being up to twice as large as in the Newtonian fluid, the cell is deformed accordingly stronger. Those effects will probably reduce in a wider channel, where this radial flow is concentrated more towards the region around the boundary.
To summarize, it is shown that the expected decreasing deformation for cells in shear thinning fluids can only be observed for cells located in the plateau region of the flow. In contrast, the deformation of a cell passing the nozzle transition is significantly larger than in a Newtonian fluid, irrespective of its radial position.

All simulations in this thesis were performed with the extended version of ESPResSo [1]. Images from simulations were created using the visualization software *ParaView* [2] and they were arranged using *GIMP* [3] and the LaTeX package *TikZ*. Data analysis was performed using custom scripts and functionalities of the software *Gnuplot* [4]. *Gnuplot* was further used to create all plots shown in the present work.

Acknowledgements

First and foremost, I want to thank my supervisor Prof. Dr. Stephan Gekle for his continuous support and guidance throughout this whole thesis. He always has an open door for questions and ideas and I am very grateful for his motivation, his patience and his dedication to the research group in general. I am very looking forward to continuing my work on this fascinating topic as a PhD student in his group.

With a special mention to Carina Bezold and Christian Bächer, who introduced me in the simulation framework, provided good advise and who shared a lot of interesting and recreating lunch breaks with me.

My sincere thanks also goes to the rest of our research group: Gabriel Sitaru, who I share an enjoyable office atmosphere with, Axel Bourdick and Simon Streit, who spent relaxing coffee breaks and disussions aside work with me, and all the others that assisted.

I would also like to thank my family: My parents, my sister and my brothers for their interest in my work and support throughout my whole life.

And finally, last but by no means least, I want to thank Tanja for providing me with unfailing support and continuous encouragement throughout my years of study. Without her standing by my side during the ups and downs, sharing both the relaxing and the stressful times with me, this thesis would not have been possible. Therefore, I want to express my deepest gratitude.

Sebastian Johannes Müller, 2018

"*Every so often, you have to unlearn what you thought you already knew, and replace it by something more subtle.*"

Sir Terry Pratchett

Contents

Part I

Introduction

1 Motivation

Facing the world's steadily increasing demand for organ replacement and tissue regeneration, the emerging technology of 3D bioprinting comes with a tremendous potential. Possible applications span from substitutes for 2D cell cultures in drug testing to the automated fabrication of a functional, living organ.
The replacement of cell cultures for drug testing would enable the field of pharmaceutical medicine to test drugs *in vitro* and replace animal models with human tissues. This is important, because animals usually respond differently to drug candidates than humans do, and thus, can be ineffective as models of human disease.[5]
Another interesting opportunity offered by 3D bioprinting is the production of organic materials that are usually obtained from animals, e. g. leather and meat. The ability to print those on demand would be a huge step in livestock and food industry.
But the most outstanding application of biofabrication techniques would be the automated production of personalized, living tissues or even organs for replacement of damaged or deseased tissues or organs. Not only would that solve the problem of the limited offer but high demand of transplants, but also approach the lack of patient-compatible donor organs, as the cells used for printing can be cultivated from the patient's.[5]
However, biofabrication techniques are still at an early stage in research and development and various challenges need to be faced in all involved disciplines.

The two key elements that constitute biofabrication processes are the bioink and the bioprinter. Therefore, several techniques have been developed to print bioinks in a three-dimensional structure.
One of these methods is the inkjet printing, which belongs to the so called droplet based bioprinting techniques. Layering the bioink by placing picoliter droplets on a substrate, the final structure is built up. Other popular methods are laser-assisted bioprinting or stereolithography. The technique most relevant for this thesis is the so called *extrusion-based bioprinting*. In this method, 2D or 3D structures are created by continuously dispersing a highly viscous hydrogel-cell mixture through a micro nozzle.

Advantages of this method include the ability to print different bioink mixtures ranging from high cell density to tissue strands and the high cell viability of typically above 90 %.[5]

The bioinks, on the other hand, need to provide many properties, which are vital for a successful printing process.
First of all, and most important, is the biocompatibility with live cells. The materials in the biomaterial solution should not damage the cells or prohibit their functionality. Other desirable properties are biodegradation, tissue regeneration, *in situ* gelation and the permeability of nutrients and metabolic waste [6]. The printed structure should furthermore posess certain mechanical properties to attain stability and stiffness in its final shape.

Regarding the printability of a bioink using extrusion-based techniques, shear thinning properties are a crucial component to produce a continuous stream of the highly viscous fluid out of the nozzle. They are also necessary to compensate for the high shear stress developed during the printing process.
Considering a free liquid jet, the pressure must be constant in the whole fluid volume. Consequently, a plug flow is assumed. A liquid flowing through a pipe, instead, cannot exhibit a plug flow, because the fluid must fulfill the no-slip boundary condition at the inner surface of the pipe, i. e. the liquid moves with the same velocity as the wall.
Therefore, the cells are exposed to different hydrodynamic forces, either when the bioink is flowing inside the printer nozzle or outside.
A fluid with shear thinning properties exhibits a velocity profile with a broader maximum than a Newtonian fluid does. With increasing strength of the shear thinning, the flow in a constrained channel becomes more similar to a plug flow, which makes for minimizing the differences between the two flow regimes inside and outside the nozzle.
As a consequence, the deformation of cells passing the transition is expected to decrease when a shear thinning fluid is used.

This expectation is investigated in this work. As a first approach to simulating stem cells in bioinks, spherical cells are included into cylindrical channels filled with a shear thinning power-law fluid. The deformation of the cells is then analyzed with respect to their initial and radial position and the strength of the shear thinning. Also, different boundary conditions are utilized to model the supply channels and the nozzle of a 3D bioprinter.
The thesis has three parts: The first one is meant to provide the necessary theoretical background of the hydrodynamics with non-Newtonian fluids and of the simulation method. The second part serves as a short user guide, explaining the features that were added to ESPResSo during this work. The last part concentrates on the simulations performed during this work: The validation of the method and the deformation of cells in shear thinning fluids.

2 Nomenclature and notation

2.1 Declaration of symbols

The following tables list the frequently used symbols for physical quantities in this thesis and their meaning.

Coordinates:

Symbol	Meaning
x, y, z	Spatial coordinates (Cartesian)
r, ϕ, z	Spatial coordinates (cylindrical)
t	Temporal coordinate
ξ	Coordinate in velocity-space

Hydrodynamic quantities:

Symbol	Physical unit	Meaning
ϱ	$\frac{\mathrm{kg}}{\mathrm{m}^3}$	Fluid mass density
ν	$\frac{\mathrm{m}^2}{\mathrm{s}}$	Kinematic viscosity of the fluid
η	$\mathrm{Pa\,s}$	Dynamic viscosity of the fluid
p	Pa	Pressure
G	$\frac{\mathrm{Pa}}{\mathrm{m}}$	Pressure gradient $= \frac{\Delta p}{L}$
$\mathfrak{f}$	N $(\frac{\mathrm{N}}{\mathrm{m}^3})$	External force (density)
$\dot{\gamma}$	$\frac{1}{\mathrm{s}}$	Shear rate
u	$\frac{\mathrm{m}}{\mathrm{s}}$	Velocity
$\underline{\tau}$	Pa	Viscous stress tensor, deviatoric stress tensor
$\underline{\sigma}$	Pa	Stress tensor
$\underline{\epsilon}$	$\frac{1}{\mathrm{s}}$	Strain rate tensor
m	$\frac{\mathrm{m}^2}{\mathrm{s}^{2-\mathrm{n}}}$ $(\mathrm{Pa\,s^n})$	Kinematic (dynamic) consistency parameter of the power-law viscosity model
n	$-$	Exponent of the power-law viscosity model
Ω	$\frac{\mathrm{m}^3}{\mathrm{s}}$	Flow rate

Lattice Boltzmann quantities:

Symbol	Meaning
$f, f_i, \boldsymbol{f}$	Particle distribution function or populations
Δx	Lattice spacing
Δt	Time step
c_s	Lattice speed of sound $= \frac{\Delta x}{\sqrt{3}\Delta t}$
c	Discretized grid velocities
w_i	Velocity weights
τ	SRT relaxation time
$\underline{\mathrm{S}}$	MRT relaxation frequency matrix
ω_S	Relaxation frequency of shear moments
$\underline{\mathrm{M}}, \underline{\mathrm{M}}^{-1}$	Matrix for (inverse) transformation into moment space

Dimensionless numbers:

Symbol	Meaning
Re	Reynolds number
Ca	Capillary number
Ma	Mach number

2.2 Acronyms

The following abbreviations for important equations and methods will be used.

Acronym	written out
LB	Lattice Boltzmann
LBM	Lattice Boltzmann method
LBE	Lattice Boltzmann equation
NSE	Navier-Stokes equation(s)
CFD	Computational fluid dynamics
BGK	Bhatnagar-Gross-Krook
IBM	Immersed-Boundary method
COM	Center of mass

2.3 Mathematical notation and conventions

The following table lists the conventions and mathematical notation used in this thesis.

Notation	Meaning	Explanation
$\boldsymbol{a}$	$\begin{pmatrix} a_1 \\ \vdots \\ a_N \end{pmatrix}$	A column vector
$\boldsymbol{a}^\intercal$	$(a_1,\ \ldots,\ a_N)$	Transpose of a vector
a_α	$\alpha \in \{1, \ldots, N\}$	Greek symbols for vector components
$\underline{\mathrm{A}}$	$\begin{pmatrix} A_{11} & \ldots & A_{1N} \\ \vdots & \ddots & \vdots \\ A_{N1} & \ldots & A_{NN} \end{pmatrix}$	A matrix (or tensor in general)
$\underline{\mathrm{I}}$	$\begin{pmatrix} 1 & \ldots & 0 \\ \vdots & \ddots & \vdots \\ 0 & \ldots & 1 \end{pmatrix}$	Identity matrix
∂_α	$\frac{\partial}{\partial \alpha}$ or $\frac{\partial}{\partial x_\alpha}$	Abbreviation for partial derivatives
$\boldsymbol{\nabla}$	$(\partial_x,\ \partial_y,\ \partial_z)$	Nabla operator
$\boldsymbol{a} \cdot \boldsymbol{b}$	$\sum_{i=1}^{N} a_i b_i$	Scalar product
$a_\alpha b_\alpha$	$\sum_{i=1}^{N} a_i b_i = \boldsymbol{a} \cdot \boldsymbol{b}$	Einstein summation convention
$\boldsymbol{ab}$	$(\boldsymbol{ab})_{\alpha\beta} = a_\alpha b_\beta$	Outer vector product (dyadic product)

Part II

Hydrodynamic and kinetic theory

3 Overview

This part of the thesis is meant to sufficiently provide the theoretical background that is necessary to understand the rest of this work. The first chapters give an overview of the hydrodynamic background, the viscosity models and analytical solutions to the macroscopic quantities. The following chapters explain the theoretical background of the Lattice Boltzmann method, i. e. the kinetic theory. The last parts focus on the actual simulation method, which is the discretized form of the kinetic theory.

The first chapter outlines the hydrodynamic theory, i. e. the macroscopic behavior of flowing fluid, which is described by the Navier-Stokes equation (4.12). A brief derivation of the governing equation will be given in 4.1.
The next chapter focuses on different types of fluid behavior, e. g. Newtonian, non-Newtonian or viscoelastic fluids, which are distinguished by their viscous and elastic properties. It contains a more detailed explanation of the class of generalized Newtonian fluids – some of which were implemented during this thesis.
Knowing about the fluid properties, an analytical solution to the flow velocity profile can be found for selected models in simple geonetries and for stationary flow. The analytical solutions are used afterwards to benchmark the simulation method.

The kinetic theory as a mesoscopic theory is the basis of the Lattice Boltzmann method. Therefore, a brief overview is given in chapter 7.
The fundamentals of the simulation method are explained in the last chapter of this part. It includes the phase space discretization, discretization in time and space and the Chapman-Enskog analysis to obtain the Navier-Stokes equation from the Boltzmann equation. Furthermore, it provides some basic background to the numerical algorithms and the simulation procedure, with a special focus on the extensions added for this thesis. A brief idea of the immersed-boundary method and the cell model is given at the end of this part.

4 Basic hydrodynamic theory

The following chapter shall give a brief introduction to the underlying hydrodynamic theory. The derivation of the Navier-Stokes equation (eq. 4.12) is strongly oriented at the one in Krüger's book [7] and condensed here for the sake of completeness. For a more detailed description, see e. g. [8].

4.1 Derivation of the Navier-Stokes equations

Consider a fluid element within the volume V_0 with a mass density ϱ. The change of mass in this fluid element per unit time is given by the inflow and outflow of mass with the velocity $\boldsymbol{u}$ by

$$\frac{\partial}{\partial t}\int\limits_{V_0} \varrho \,\mathrm{d}V = -\oint\limits_{\partial V_0} \varrho \boldsymbol{u} \cdot \mathrm{d}\boldsymbol{A} \quad . \tag{4.1}$$

Applying the divergence theorem on the right hand side yields

$$\int\limits_{V_0} \frac{\partial \varrho}{\partial t}\,\mathrm{d}V = -\int\limits_{V_0} \boldsymbol{\nabla}\cdot(\varrho\boldsymbol{u})\,\mathrm{d}V \quad , \tag{4.2}$$

and, since V_0 is arbitrary, the *continuity equation* is obtained by the equality of the integrands:

$$\frac{\partial \varrho}{\partial t} = \boldsymbol{\nabla}\cdot(\varrho\boldsymbol{u}) = 0 \tag{4.3}$$

Analogously, the change of the momentum density $\varrho\boldsymbol{u}$ can be considered:

$$\frac{\mathrm{d}}{\mathrm{d}t}\int\limits_{V_0} \varrho\boldsymbol{u}\,\mathrm{d}V = \underbrace{-\oint\limits_{\partial V_0} \varrho\boldsymbol{u}\boldsymbol{u}\cdot\mathrm{d}\boldsymbol{A}}_{(1)} \underbrace{-\oint\limits_{\partial V_0} p\,\mathrm{d}\boldsymbol{A}}_{(2)} + \underbrace{\int\limits_{V_0} \mathfrak{f}\,\mathrm{d}V}_{(3)} \tag{4.4}$$

In opposite to the change of mass, momentum change can be not only due to inflow and outflow (1), but also due to differences in pressure (2) and external forces (3). Here, $\mathfrak{f}$ is considered a bodyforce with the physical unit $\frac{\mathrm{N}}{\mathrm{m}^3}$. This equation can be rewritten, again

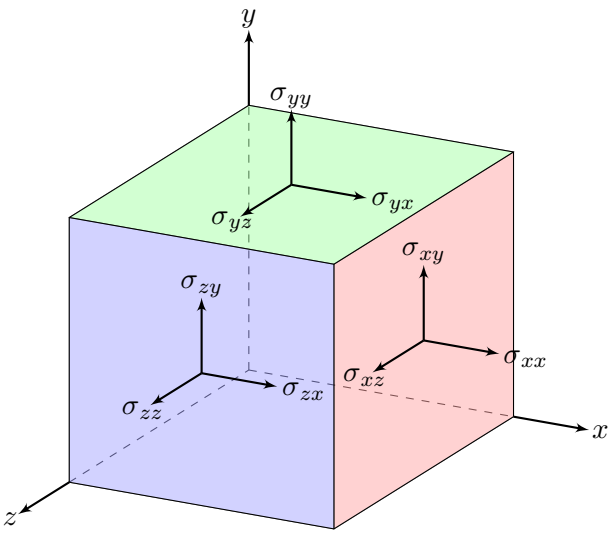

Figure 4.1: Components of the stress tensor in a Cartesian coordinate system shown at the faces of a cube.

using the divergence theorem, giving

$$\int_{V_0} \frac{\partial \varrho \boldsymbol{u}}{\partial t} \,\mathrm{d}V = -\int_{V_0} \boldsymbol{\nabla} \cdot (\varrho \boldsymbol{u}\boldsymbol{u}) \,\mathrm{d}V - \int_{V_0} \boldsymbol{\nabla} p \,\mathrm{d}V + \int_{V_0} \mathfrak{f} \,\mathrm{d}V \quad , \tag{4.5}$$

and, for an arbitrary volume V_0, one gains the *Euler equation*

$$\frac{\partial \varrho \boldsymbol{u}}{\partial t} + \boldsymbol{\nabla} \cdot (\varrho \boldsymbol{u}\boldsymbol{u}) = -\boldsymbol{\nabla} p + \mathfrak{f} \quad . \tag{4.6}$$

By defining the *momentum flux densiy tensor*,

$$\underline{\Pi} = \varrho \boldsymbol{u}\boldsymbol{u} - \underline{\sigma} \tag{4.7}$$

with the stress tensor $\underline{\sigma} = -p\underline{\mathrm{I}}$, one can transform the Euler equation into the more general *Cauchy momentum equation*

$$\frac{\partial \varrho \boldsymbol{u}}{\partial t} + \boldsymbol{\nabla} \cdot \underline{\Pi} = \mathfrak{f} \quad . \tag{4.8}$$

The components of the stress tensor are depicted in fig. 4.1. Considering the above definitions, this equation describes simple liquids with an isotropic stress. In a real fluid, dissipative and irreversible processes on molecular level result on an additional momentum transfer due to internal friction or viscosity. To account for these effects, the isotropic stress tensor from eq. (4.7) is extended by the *viscous stress tensor* or *stress deviator tensor* τ, defined by

$$\underline{\tau} = \eta \left[\boldsymbol{\nabla} \boldsymbol{u} + (\boldsymbol{\nabla} \boldsymbol{u})^{\mathsf{T}} - \tfrac{2}{3} (\boldsymbol{\nabla} \cdot \boldsymbol{u}) \underline{\mathrm{I}} \right] + \eta_{\mathrm{B}} (\boldsymbol{\nabla} \cdot \boldsymbol{u}) \underline{\mathrm{I}} \quad . \tag{4.9}$$

The first term, starting with the *shear viscosity* η is traceless and stands for the shear stress present in the fluid. The isotropic latter part represents the normal stress, its coefficient is usually referred to as *bulk (or volume) viscosity*.
Inserting the extended stress tensor,

$$\underline{\sigma} = \underline{\tau} - p\underline{\mathrm{I}} \quad , \tag{4.10}$$

into the Euler equation (4.6) yields the *Navier-Stokes equation* (NSE) for compressible fluids:

$$\begin{aligned} \frac{\partial \varrho \boldsymbol{u}}{\partial t} + \boldsymbol{\nabla} \cdot (\varrho \boldsymbol{u}\boldsymbol{u}) = &- \boldsymbol{\nabla} p + \boldsymbol{\nabla} \cdot \{\eta \left[\boldsymbol{\nabla}\boldsymbol{u} + (\boldsymbol{\nabla}\boldsymbol{u})^{\mathsf{T}}\right]\} \\ &+ \left(\eta_{\mathrm{B}} - \tfrac{2}{3}\eta\right) \boldsymbol{\nabla} (\boldsymbol{\nabla} \cdot \boldsymbol{u}) + \mathfrak{f} \end{aligned} \tag{4.11}$$

Regarding the fluid as incompressible, i. e. $\varrho = \text{const.}$, and substituting the rate of strain tensor, $\underline{\epsilon} = \frac{1}{2}\left[\boldsymbol{\nabla}\boldsymbol{u} + (\boldsymbol{\nabla}\boldsymbol{u})^{\mathsf{T}}\right]$, yields the *incompressible Navier-Stokes equation*, that is used for the analytical calculations in this thesis:

$$\varrho \left[\frac{\partial \boldsymbol{u}}{\partial t} + (\boldsymbol{u} \cdot \boldsymbol{\nabla})\, \boldsymbol{u}\right] = -\boldsymbol{\nabla} p + \boldsymbol{\nabla} \cdot (2\eta\, \underline{\epsilon}) + \mathfrak{f} \tag{4.12}$$

In this form, the Navier-Stokes equation includes Newton's postulate of viscosity, i. e. the viscous stress is directly propotional to the rate of strain:

$$\underline{\tau} = 2\eta\, \underline{\epsilon} \tag{4.13}$$

A further simplification of eq. (4.12),

$$\boldsymbol{\nabla} \cdot (2\eta\, \underline{\epsilon}) = \eta \boldsymbol{\Delta} \boldsymbol{u} \quad , \tag{4.14}$$

is possible if the viscosity η is considered constant. However, this is only given for Newtonian fluids and, at least in this thesis, the special case.

For completeness, the tables 4.1 and 4.2 list all components of the Navier-Stokes equation (4.12) as well as the continuity equation (4.3) for Cartesian and cylindrical coordinates. They also include the components of the viscous stress tensor in the respective coordinate system.

Table 4.1: Components of the incompressible NSE in Cartesian coordinates (x, y, z).

Incompressibility:

$$\frac{\partial u_x}{\partial x} + \frac{\partial u_y}{\partial y} + \frac{\partial u_z}{\partial z} = 0$$

x-Component:

$$\varrho\left(\frac{\partial u_x}{\partial t} + u_x\frac{\partial u_x}{\partial x} + u_y\frac{\partial u_x}{\partial y} + u_z\frac{\partial u_x}{\partial z}\right) = -\frac{\partial p}{\partial x} + \left(\frac{\partial \tau_{xx}}{\partial x} + \frac{\partial \tau_{yx}}{\partial y} + \frac{\partial \tau_{zx}}{\partial z}\right) + \varrho \mathfrak{f}_x$$

y-Component:

$$\varrho\left(\frac{\partial u_y}{\partial t} + u_x\frac{\partial u_y}{\partial x} + u_y\frac{\partial u_y}{\partial y} + u_z\frac{\partial u_y}{\partial z}\right) = -\frac{\partial p}{\partial y} + \left(\frac{\partial \tau_{xy}}{\partial x} + \frac{\partial \tau_{yy}}{\partial y} + \frac{\partial \tau_{zy}}{\partial z}\right) + \varrho \mathfrak{f}_y$$

z-Component:

$$\varrho\left(\frac{\partial u_z}{\partial t} + u_x\frac{\partial u_z}{\partial x} + u_y\frac{\partial u_z}{\partial y} + u_z\frac{\partial u_z}{\partial z}\right) = -\frac{\partial p}{\partial z} + \left(\frac{\partial \tau_{xz}}{\partial x} + \frac{\partial \tau_{yz}}{\partial y} + \frac{\partial \tau_{zz}}{\partial z}\right) + \varrho \mathfrak{f}_z$$

Viscous stress tensor:

$$\tau_{\alpha\beta} = \eta\left(\frac{\partial u_\alpha}{\partial \beta} + \frac{\partial u_\beta}{\partial \alpha}\right)$$

Table 4.2: Components of the incompressible NSE in cylindrical coordinates (r, ϕ, z).

Incompressibility:

$$\frac{1}{r}\frac{\partial}{\partial r}\left(r u_r\right) + \frac{1}{r}\frac{\partial u_\phi}{\partial \phi} + \frac{\partial u_z}{\partial z} = 0$$

r-Component:

$$\begin{aligned}\varrho\left(\frac{\partial u_r}{\partial t} + u_r\frac{\partial u_r}{\partial r} + \frac{u_\phi}{r}\frac{\partial u_r}{\partial \phi} - \frac{u_\phi^2}{r} + u_z\frac{\partial u_r}{\partial z}\right)\\ = -\frac{\partial p}{\partial r} + \left(\frac{1}{r}\frac{\partial}{\partial r}\left(r\tau_{rr}\right) + \frac{1}{r}\frac{\partial \tau_{\phi r}}{\partial \phi} - \frac{\tau_{\phi\phi}}{r} + \frac{\partial \tau_{zr}}{\partial z}\right) + \varrho \mathfrak{f}_r\end{aligned}$$

ϕ-Component:

$$\begin{aligned}\varrho\left(\frac{\partial u_\phi}{\partial t} + u_r\frac{\partial u_\phi}{\partial r} + \frac{u_\phi}{r}\frac{\partial u_\phi}{\partial \phi} - \frac{u_r u_\phi}{r} + u_z\frac{\partial u_\phi}{\partial z}\right)\\ = -\frac{1}{r}\frac{\partial p}{\partial \phi} + \left(\frac{1}{r^2}\frac{\partial}{\partial r}\left(r^2\tau_{r\phi}\right) + \frac{1}{r}\frac{\partial \tau_{\phi\phi}}{\partial \phi} + \frac{\partial \tau_{z\phi}}{\partial z} + \frac{\tau_{\phi r} - \tau_{r\phi}}{r}\right) + \varrho \mathfrak{f}_\phi\end{aligned}$$

z-Component:

$$\begin{aligned}\varrho\left(\frac{\partial u_z}{\partial t} + u_r\frac{\partial u_z}{\partial r} + \frac{u_\phi}{r}\frac{\partial u_z}{\partial \phi} + u_z\frac{\partial u_z}{\partial z}\right)\\ = -\frac{\partial p}{\partial z} + \left(\frac{1}{r}\frac{\partial}{\partial r}\left(r\tau_{rz}\right) + \frac{1}{r}\frac{\partial \tau_{\phi z}}{\partial \phi} + \frac{\partial \tau_{zz}}{\partial z}\right) + \varrho \mathfrak{f}_z\end{aligned}$$

Viscous stress tensor:

$$\tau = \eta\begin{pmatrix} 2\frac{\partial u_r}{\partial r} & \frac{\partial u_\phi}{\partial r} + \frac{1}{r}\frac{\partial u_r}{\partial \phi} - \frac{u_\phi}{r} & \frac{\partial u_r}{\partial z} + \frac{\partial u_z}{\partial r} \\ \frac{\partial u_\phi}{\partial r} + \frac{1}{r}\frac{\partial u_r}{\partial \phi} - \frac{u_\phi}{r} & \frac{2}{r}\frac{\partial u_\phi}{\partial \phi} + \frac{2u_r}{r} & \frac{1}{r}\frac{\partial u_z}{\partial \phi} + \frac{\partial u_\phi}{\partial z} \\ \frac{\partial u_r}{\partial z} + \frac{\partial u_z}{\partial r} & \frac{1}{r}\frac{\partial u_z}{\partial \phi} + \frac{\partial u_\phi}{\partial z} & 2\frac{\partial u_z}{\partial z} \end{pmatrix}$$

5 Non-Newtonian fluids

This chapter shall provide a brief overview of the models that are used to describe non-Newtonian fluid behavior. The first part explains the main characteristics of these models and how they differ regarding their theoretical description. The second part is about the inelastic viscosity models that are implemented during this work and how their properties correspond to the flow behavior of real fluids.

5.1 Introduction

One can define a liquid as a "material that will continuously change its shape (i. e. will flow) when subjected to a given stress, irrespective of how small that stress may be" [9]. Even in everyday life, one can observe a wide range of viscosities for different materials. Table 5.1 lists the order of magnitude of the viscosity for some familiar materials.
The *Newtonian postulate* defines the relationship of shear stress $\underline{\tau}$ and rate of strain $\underline{\epsilon}$ as

$$\underline{\tau} = 2\,\eta\underline{\epsilon} \quad . \tag{5.1}$$

The viscosity, in this case, is the proportionality constant η. However, what can be seen from the first two entries of the table, is the strong dependency of the viscosity on the temperature. This is not subject of this thesis, but it is important to state that a Newtonian fluid exhibits a constant viscosity only with respect to the shear rate. That means that other parameters, like the temperature or the pressure, can still have an effect on the flow properties of a Newtonian liquid. For many fluids, the viscosity follows an Arrhenius relationship, i. e.

$$\eta\,(T) = Ae^{-B/T} \tag{5.2}$$

where T denotes the absolute temperature and A and B are material constants.
Fluids that do not follow this Newtonian law of viscosity, however, are present in many different fields in everyday life: A lot of liquid foods exhibit special flow behaviour [10 – 12], as well as construction materials [13] or physiologically important fluids like blood [14]. It is necessary to investigate their rheological properties in order to optimize manufacturing processes or understand physiological phenomena.

Table 5.1: The order of magnitude of the dynamic viscosity given for some familiar materials. (from [9])

Liquid	η (Pa s)
Glass	10^{40}
Molten glass (500 °C)	10^{12}
Bitumen	10^{8}
Liquid honey	10^{1}
Glycerol	1
Water	10^{-3}
Air	10^{-5}

Figure 5.1: Different types of flow behavior: Shear thinning (pseudoplastic), shear thickening (dilatant) and Newtonian properties can be described by the stress – shear rate relationship of generalized Newtonian fluids. There are also fluids that require a finite yield stress before flowing, like the Bingham plastics.

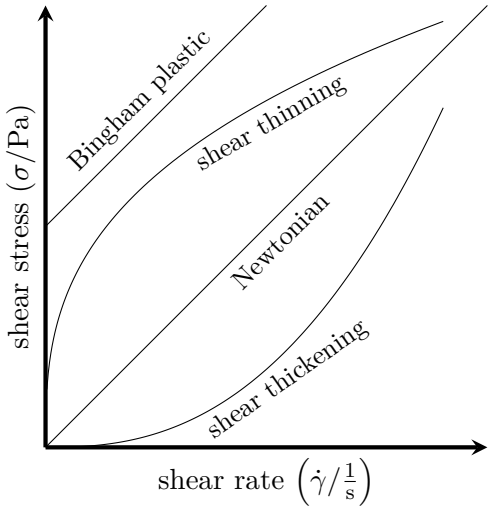

5.2 Types of non-Newtonian fluids

5.2.1 Inelastic models

There are several types of non-Newtonian fluids that can be distinguished by their behaviour. Starting from a Newtonian fluid, the viscous stress tensor is directly proportional to the strain rate tensor like

$$\underline{\tau} = \eta \left[\boldsymbol{\nabla u} + (\boldsymbol{\nabla u})^{\mathsf{T}}\right] = 2\,\eta \underline{\epsilon} \quad , \tag{5.3}$$

where the proportionality constant η denotes the constant dynamic viscosity of the fluid. Furhtermore, the rate of strain tensor is defined as

$$\underline{\epsilon} = \tfrac{1}{2} \left[\boldsymbol{\nabla u} + (\boldsymbol{\nabla u})^{\mathsf{T}}\right] \tag{5.4}$$

A generalization of this equation leads to the so called *generalized Newtonian fluids*, with the viscous stress following the equation

$$\underline{\tau} = \eta\left(\dot{\gamma}\right) \left[\boldsymbol{\nabla u} + (\boldsymbol{\nabla u})^{\mathsf{T}}\right] \quad , \tag{5.5}$$

η being a function of the rate of shear $\dot{\gamma}$. This function is usually referred to as *apparent viscosity*. The shear rate is defined via the second invariant of the strain rate tensor [15]

$$\dot{\gamma} = \sqrt{2\,\mathrm{II}_\epsilon} = \sqrt{2\,\epsilon_{\alpha\beta}\epsilon_{\alpha\beta}} \tag{5.6}$$

The generalized Newtonian fluids can also be seen as a special case of the *Reiner-Rivlin model*, which has constitutive equations of the form [9]

$$\underline{\tau} = 2\eta\left(\mathrm{II}_\epsilon, \mathrm{III}_\epsilon\right) \underline{\epsilon} + 4\zeta\left(\mathrm{II}_\epsilon, \mathrm{III}_\epsilon\right) \underline{\epsilon}^2 \quad . \tag{5.7}$$

Here, η and ζ are functions of the second and third principal invariant of the strain rate tensor, II_ϵ and III_ϵ respectively. This model is in general inelastic, although it predicts normal stresses if $\zeta \neq 0$. However, the behavior of the fluid does not match experimental results for steady simple shear flow in this case. Consequently, the generalized Newtonian fluids with $\zeta = 0$ and η only depending on the second Invariant of $\underline{\epsilon}$ have become more popular. [9, 16]

5.2.2 Time dependent models

In addition to the viscosity being dependent on the shear rate in a flow, it is also observed that it can depend on the duration of applied stress. Such materials are called *rheopex*, if the apparent viscosity increases with the duration of the stress, and *thixotropic* if it decreases, respectively. When the stress is removed, the material gradually recovers until the viscosity at zero shear is reached.
Examples for those types are printer ink or gypsum paste (rheopex), and yogurt, gelatin gels, wall paints and many colloidal suspensions (thixotropic).[15, 17]

5.2.3 Viscoelastic models

The term *viscoelastic* describes fluids that exhibit viscous as well as elastic behavior. The definition falls between the classical extremes of Hookean elastic response and Newtonian viscous behavior [9].
If the elastic behavior is modeled with a Hookean spring, the stress σ relates to the deformation ε as

$$\sigma = E\varepsilon \quad , \tag{5.8}$$

where E is the elastic modulus. Using the same terminology, Newton's postulate of viscosity reads

$$\sigma = \eta \frac{\partial \varepsilon}{\partial t} \quad . \tag{5.9}$$

The linear combination of these equations leads to the *Kelvin-Voigt model*, with its constitutive equation

$$\sigma = E\varepsilon + \eta \frac{\partial \varepsilon}{\partial t} \quad . \tag{5.10}$$

There exist numerous linear and also nonlinear viscoelastic models to describe the properties of different materials and a detailed introduction can be found in [9]. Some examples for such materials are whipped cream or silly putty.

5.2.4 Newtonian limits

Most real fluids have been observed to exhibit non-Newtonian behavior only in a limited range of shear rates. In the limits of very low ($\dot{\gamma} \to 0$) or high ($\dot{\gamma} \to \infty$) rates of shear, a constant viscosity is observed, i. e. Newtonian behavior.
A rather practical way of explaining the Newtonian limits of the viscosity for most real shear thinning liquids can be given by looking at a sufficiently high concentrated biopolymer dispersion. At very low shear rates, there is only little rearrangement in the configuration of the molecules, while it undergoes gradual rearrangement for intermediate shear rates resulting in power-law behavior. When all molecules are fully arranged, i. e. no further rearrangement is possible, the second Newtonian region is reached.[12]

5.3 Implemented inelastic models

This section provides an overview of the viscosity models that have been implemented during this thesis. All of them belong to the class of generalized Newtonian fluids and have different advantages and disadvantages regarding their applicability and analytical solvability, which are discussed in the following. The models and their parameters are chosen according to [18] and [19].
The viscosity-shear rate relationship of these models is depicted in fig. 5.2. The parameters

are chosen in a way that the power-law behavior is the same for all models, which makes for comparing the influence of the different parameters.

5.3.1 Power-law model

One of the simplest generalized Newtonian fluid models is the power-law model, defined by the *Ostwald-de Waele* relationship

$$\tau = m\,\dot{\gamma}^n = \eta\left(\dot{\gamma}\right)\,\dot{\gamma} \quad , \tag{5.11}$$

with η denoting the apparent viscosity as a function of the shear rate. The parameter m is usually referred to as *consistency parameter* or *consistency index*, as it has a physical unit of $\mathrm{Pa\,s^n}$ and no real physical meaning in this sense. For $n = 1$, the power-law model becomes Newtonian and the consistency parameter denotes the dynamic viscosity.
The model is capable of describing both shear thinning and shear thickening behavior of a fluid by the choice of the *power-law exponent* n:

$n < 1$	shear thinning (pseudoplastic)
$n = 1$	Newtonian
$n > 1$	shear thickening (dilatant)

This behavior is easy to see by a look at the apparent viscosity, which takes the form

$$\eta\left(\dot{\gamma}\right) = m\dot{\gamma}^{n-1} \quad . \tag{5.12}$$

Due to its simplicity, it is possible to find an analytical expression for the velocity profile by solving the Navier-Stokes equation for stationary flow in simple geometries. In this thesis, the flow profile for a power-law fluid in a cylinder is derived in 6.3.
However, this simplicity has its price: For $n < 1$ the viscosity of the fluid would reach zero in the limit of $\dot{\gamma} \to \infty$ and would become infinite for vanishing shear rates. This is not what is typically observed for real fluids, because physical and chemical processes at the molecular level make for Newtonian behavior in the limits of zero and infinite rates of shear. Thus, the power-law model is only a useful description for the viscosity of a fluid when the considered range of $\dot{\gamma}$ corresponds to the range that was used to fit the parameters to experimental data.
Nevertheless, its use in literature is widely spread from modeling physiological fluids like blood [20, 21] to construction materials like concrete [22].

5.3.2 Truncated power-law model

An approach to overcome the problem with the restricted range of applicability is to extend the power-law model with two Newtonian plateau regions for low and high shear rates. Let $\dot{\gamma}_0$ and $\dot{\gamma}_\infty$ be the limiting shear rates for Newtonian behavior, then the apparent

viscosity of the so called *truncated power-law model* takes the form

$$\eta(\dot{\gamma}) = \begin{cases} \eta_0 & \dot{\gamma} \leq \dot{\gamma}_0 \\ m\dot{\gamma}^{n-1} & \dot{\gamma}_0 < \dot{\gamma} < \dot{\gamma}_\infty \\ \eta_\infty & \dot{\gamma} \geq \dot{\gamma}_\infty \end{cases}, \tag{5.13}$$

where $\eta_0 = m\dot{\gamma}_0^{n-1}$ and $\eta_\infty = m\dot{\gamma}_\infty^{n-1}$ denote the constant viscosity in the range of low and high shear rates, respectively.
Similar to the power-law model, the truncated one also provides the possibility to derive an analytical expression for the steady flow profile in simple geometries, as shown in 6.4.

5.3.3 Sisko model

A simple extension to the power-law model that accounts for a finite viscosity in the limit of infinite shear rates is the Sisko model. However, a finite viscosity for low shear rates and $n < 1$ is not included, which can be easily seen by a look at the equation:

$$\eta(\dot{\gamma}) = m\dot{\gamma}^{n-1} + \eta_\infty \tag{5.14}$$

5.3.4 Carreau-Yasuda model

Another possibility to account for the Newtonian behavior in the limit of zero and infinite shear rate is given by the Carreau-Yasuda model, desribed by the equation

$$\eta(\dot{\gamma}) = \frac{\eta_0 - \eta_\infty}{(1 + (K\dot{\gamma})^{a_1})^{\frac{a_2}{a_1}}} + \eta_\infty \quad , \tag{5.15}$$

with a constant inverse shear rate K and two exponents a_1 and a_2, which determine the shape of the viscosity curve with respect to the shear rate.
This model offers a smoother transition between the Newtonian plateaus and the power-law behavior than the truncated power-law , and thus, is very well suited for describing the viscosity of a fluid over the full range of shear rates. However, it does so at the expense of simplicity: An analytical solution is only possible for a very limited set of parameters, i. e. $a_1 = a_2 = 1$ and $\eta_\infty = 0$.
The Carreau-Yasuda model is employed frequently, e. g. to describe the rheological properties of blood [20, 23] or polymer dispersions [24].

5.3.5 Carreau model

The above mentioned Carreau-Yasuda model is a combination or extension of earlier viscosity models, which are obtained by choosing special parameters. Setting $a_1 = 2$ and

$a_2 = a$ in eq. (5.15), one gets the equation for the Carreau model:

$$\eta(\dot{\gamma}) = \frac{\eta_0 - \eta_\infty}{\left(1 + (K\dot{\gamma})^2\right)^{\frac{a}{2}}} + \eta_\infty \quad . \tag{5.16}$$

5.3.6 Cross model

By choosing $a_1 = a_2 = a$ in eq. (5.15), the Cross model is obtained, with the apparent viscosity described by

$$\eta(\dot{\gamma}) = \frac{\eta_0 - \eta_\infty}{1 + (K\dot{\gamma})^a} + \eta_\infty \quad . \tag{5.17}$$

Figure 5.2: The viscosity of the inelastic models plotted with respect to the shear rate in a log-log-diagram. The parameters are chosen in a way that the power-law behavior for intermediate shear rates is the same for all models. The Carreau-Yasuda model has an additional free parameter a_1, the effect of which is shown by the three red lines.

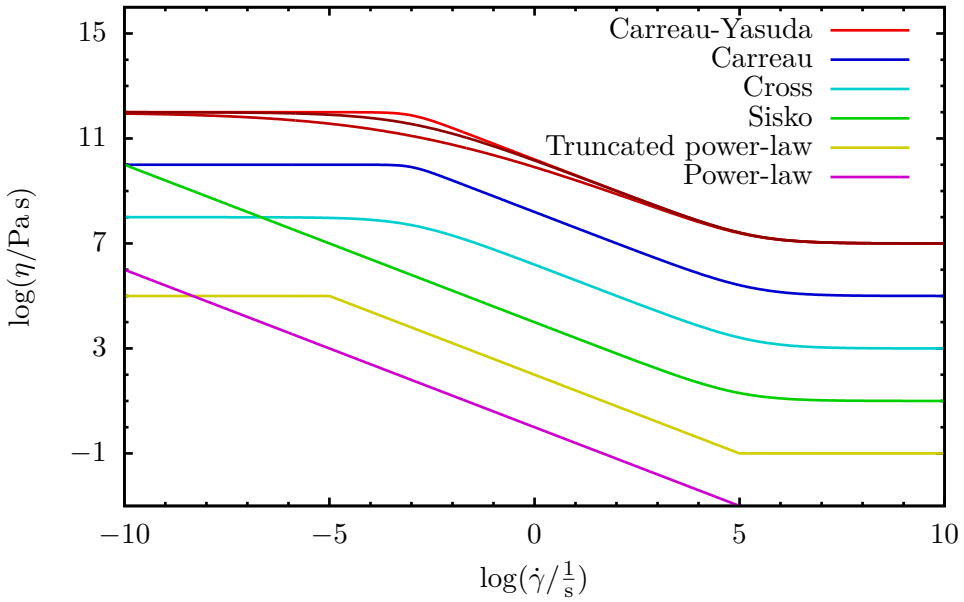

6 Derivation of analytical solutions to the NSE

In this chapter, the velocity and shear rate profile will be derived for the viscosity models that allow an analytical solution. In general, the more sophisticated a model is, the more complicated is the corresponding analytical solution. The equations used here are the continuity equation, the components of the Navier-Stokes equation and the viscous stress tensor for cylindrical coordinates, which are all listed in table 4.2.

6.1 Assumptions

The channel shall be a cylinder with radius R and length L that is oriented along the z-axis. Furthermore, the following assumptions are made for all derivations:

1. There are no external body forces present:

$$\mathbf{f} = \mathbf{0} \tag{6.1}$$

2. The flow is stationary:

$$\frac{\partial \boldsymbol{u}}{\partial t} = \mathbf{0} \tag{6.2}$$

3. The flow is fully developed, i. e. there is no variation in flow direction:

$$\frac{\partial (\dots)}{\partial z} = \mathbf{0} \tag{6.3}$$

4. The flow is axial symmetric and only in z-direction:

$$\frac{\partial \boldsymbol{u}}{\partial \phi} = 0 \tag{6.4}$$

$$u_r = u_\phi = 0 \tag{6.5}$$

The last assumption reduces the viscous stress tensor to just two components, which are

$$\tau_{zr} = \tau_{rz} = \frac{\partial u_z}{\partial r} \quad . \tag{6.6}$$

Inserting this and the assumptions into the components of the Navier-Stokes equation yields that the pressure gradient has its only non-zero component in z-direction:

$$\boldsymbol{\nabla} p = \frac{\partial p}{\partial z}\hat{\boldsymbol{e}}_z = \frac{\Delta p}{L}\hat{\boldsymbol{e}}_z \tag{6.7}$$

Thus, the remaining equation to solve is the z-component of the NSE, which reduces to

$$\frac{\partial p}{\partial z} = \frac{1}{r}\frac{\partial}{\partial r}\left(r\tau_{rz}\right) = \frac{1}{r}\frac{\partial}{\partial r}\left(r\eta\left(\dot{\gamma}\right)\frac{\partial u_z}{\partial r}\right) \quad , \tag{6.8}$$

with the shear rate $\dot{\gamma} := -\frac{\partial u_z}{\partial r} > 0$ and $G := \frac{\partial p}{\partial z} < 0$.

6.2 Boundary conditions

The first boundary condition is a no-slip condition at the channel wall, i. e. the fluid must have the same velocity as the wall, which is zero in this case:

$$\boldsymbol{u}\big|_{r=R} = \boldsymbol{0} \tag{6.9}$$

The second boundary condition is motivated by the channel symmetry: In the center, at $r = 0$, the profile shall be continuously differentiable. Thus, the maximum of the velocity has to be at the channel center and the radial derivative, i. e. the shear rate, vanishes:

$$\left.\frac{\partial u_z}{\partial r}\right|_{r=0} = \dot{\gamma}\big|_{r=0} = 0 \tag{6.10}$$

6.3 Power-law model

The viscosity as a function of the shear rate was defined in chap. 5.3.1 as

$$\eta\left(\dot{\gamma}\right) = m\dot{\gamma}^{n-1} \quad . \tag{6.11}$$

Inserting this into eq. (6.8) yields

$$G = \frac{1}{r}\frac{\partial}{\partial r}\left(rm\dot{\gamma}^{n-1}\frac{\partial u_z}{\partial r}\right) \tag{6.12}$$

$$\Leftrightarrow \quad -Gr = \frac{\partial}{\partial r}\left(rm\dot{\gamma}^{n}\right) \quad . \tag{6.13}$$

Integration over r and rearrangement leads to

$$\dot{\gamma}^n = -\frac{G}{2m}r + \frac{c_1}{rm} \quad . \tag{6.14}$$

The integration constant c_1 must vanish to fulfill the second boundary condition in eq. (6.10), thus an expression for the shear rate is given by

$$\dot{\gamma} = \left(-\frac{G}{2m}\right)^{\frac{1}{n}} r^{\frac{1}{n}} \quad . \tag{6.15}$$

Inserting the defintion of $\dot{\gamma}$ as derivative of the velocity and another integration give

$$\frac{\partial u_z}{\partial r} = -\left(-\frac{G}{2m}\right)^{\frac{1}{n}} r^{\frac{1}{n}} \tag{6.16}$$

$$\Leftrightarrow \quad u_z(r) = -\left(-\frac{G}{2m}\right)^{\frac{1}{n}} \frac{1}{1+\frac{1}{n}} r^{\frac{1}{n}+1} + c_2 \quad , \tag{6.17}$$

where the second integration constant c_2 is determined by the no-slip boundary condition in eq. (6.9):

$$c_2 = \left(-\frac{G}{2m}\right)^{\frac{1}{n}} \frac{1}{1+\frac{1}{n}} R^{\frac{1}{n}+1} \tag{6.18}$$

The analytical solutions for the power-law fluid are therefore given as:

$$u_z(r) = u_{\max}\left[1 - \left(\frac{r}{R}\right)^{\frac{1}{n}+1}\right] \quad , \tag{6.19}$$

$$\dot{\gamma}(r) = \left(-\frac{G}{2m}\right)^{\frac{1}{n}} r^{\frac{1}{n}} \tag{6.20}$$

with

$$u_{\max} = \left(-\frac{G}{2m}\right)^{\frac{1}{n}} \frac{1}{1+\frac{1}{n}} R^{\frac{1}{n}+1} \tag{6.21}$$

Here $u_{\max} = u_z(0)$ is the maximum velocity at the channel center.
As it is later used to tune simulation input parameters, the formula for the flow rate Ω is quickly derived in the following. It is defined as surface integral of the velocity field and

can be expressed in terms of the power-law exponent and the maximum velocity as:

$$\Omega = \int_0^{2\pi} \int_0^R r u_z(r) \, \mathrm{d}\phi \, \mathrm{d}r \tag{6.22}$$

$$\Omega(n) = \int_0^{2\pi} \int_0^R r u_{\max} \left[1 - \left(\frac{r}{R} \right)^{\frac{1}{n}+1} \right] \mathrm{d}\phi \, \mathrm{d}r \tag{6.23}$$

$$= \pi R^2 u_{\max} \left(1 - \frac{2}{3 + \frac{1}{n}} \right) \tag{6.24}$$

6.4 Truncated power-law model

$$\eta(\dot{\gamma}) = \begin{cases} \eta_0 = m\dot{\gamma}_0^{n-1} & \dot{\gamma} \leq \dot{\gamma}_0 \\ m\dot{\gamma}^{n-1} & \dot{\gamma}_0 < \dot{\gamma} < \dot{\gamma}_\infty \\ \eta_\infty = m\dot{\gamma}_\infty^{n-1} & \dot{\gamma} \geq \dot{\gamma}_\infty \end{cases} . \tag{6.25}$$

The solution to the truncated power-law model is a bit more complex, as the different cases in the viscosity model require to solve a system of partial differential equations that is connected through the boundary conditions of each equation. The solution for the velocity profile is made of three parts,

$$u_z(r) = \begin{cases} u_1(r) & r \leq r_0 \\ u_2(r) & r_0 < r < r_\infty \\ u_3(r) & r \geq r_\infty \end{cases} , \tag{6.26}$$

with u_1 and u_3 being the Newtonian regions and u_2 the power-law region in the range $[r_0\,,\, r_\infty]$, where r_0 and r_∞ are the radial positions at which the shear rate reaches the limits $\dot{\gamma}_0$ and $\dot{\gamma}_\infty$, respectively.
The equations to solve are:

$$G = \frac{1}{r}\frac{\partial}{\partial r}(-r\eta_0\dot{\gamma}_1) \qquad \text{with } \dot{\gamma}_1 = -\frac{\partial u_1}{\partial r} \tag{6.27}$$

$$G = \frac{1}{r}\frac{\partial}{\partial r}(-rm\dot{\gamma}_2^n) \qquad \text{with } \dot{\gamma}_2 = -\frac{\partial u_2}{\partial r} \tag{6.28}$$

$$G = \frac{1}{r}\frac{\partial}{\partial r}(-r\eta_\infty\dot{\gamma}_3) \qquad \text{with } \dot{\gamma}_3 = -\frac{\partial u_3}{\partial r} \tag{6.29}$$

Note that $\dot{\gamma}_{1,2,3}$ are functions of r as well, the abbreviation is used for better readability. To solve this system of second order differential equations, six boundary conditions are necessary. The first two correspond to the general boundary conditions defined by eq. (6.9) and eq. (6.10). The latter four ensure that $u_z(r)$ is continuously differentiable at r_0 and

Figure 6.1: Analytical solutions to the power-law model for the velocity, the shear rate and the viscosity in a cylindrical channel with radius R. The normalization is with respect to the maximum velocity at the channel center, the shear rate at the channel wall and the Newtonian viscosity ($n = 1.0$).

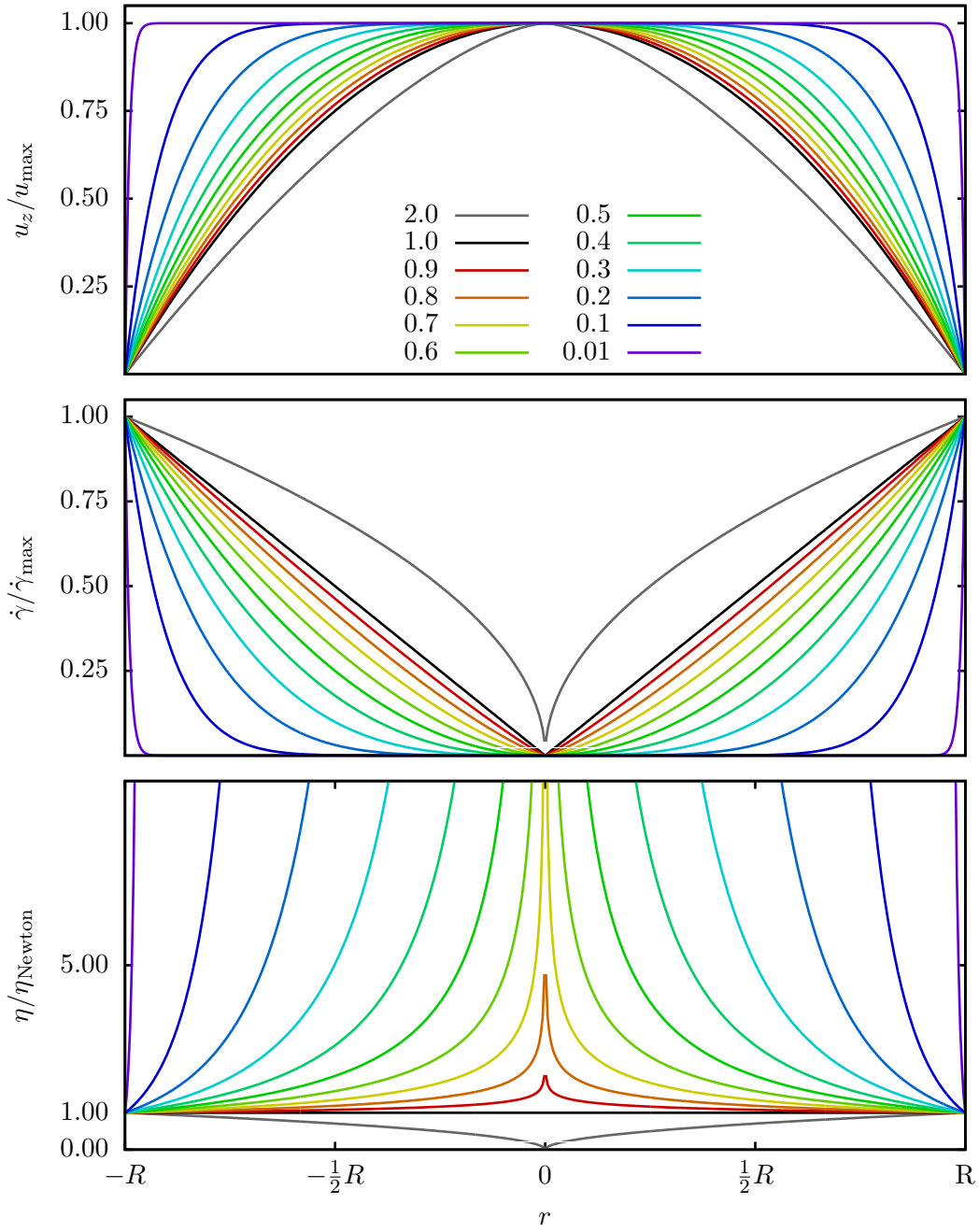

r_∞. The conditions are:

1. $\dot{\gamma}_1(0) = 0$
2. $u_3(R) = 0$
3. $\dot{\gamma}_1(r_0) = \dot{\gamma}_2(r_0)$
4. $\dot{\gamma}_2(r_\infty) = \dot{\gamma}_3(r_\infty)$
5. $u_1(r_0) = u_2(r_0)$
6. $u_2(r_\infty) = u_3(r_\infty)$

Starting with the central region ($0 \leq r \leq r_0$), one can integrate eq. (6.27) once to obtain a solution for the shear rate $\dot{\gamma}_1$:

$$G = \frac{1}{r}\frac{\partial}{\partial r}\left(-r\eta_0\dot{\gamma}_1\right) \tag{6.30}$$

$$\Leftrightarrow \quad \dot{\gamma}_1 = -\frac{Gr}{2\eta_0} - \frac{c_{1a}}{\eta_0 r} \tag{6.31}$$

$$\tag{6.32}$$

The integration constant c_{1a} is determined by the first boundary condition. $\dot{\gamma}_1$ is only finite for $r = 0$ if the constant is zero. Therefore, the analytical solution for the shear rate in the central Newtonian region is already defined and determines the expressions for the limiting shear rate $\dot{\gamma}_0$ and its radial position r_0:

$$\dot{\gamma}_1(0) = 0 \qquad \Rightarrow \quad c_{1a} = 0 \tag{6.33}$$

$$\dot{\gamma}_0 = \dot{\gamma}_1(r_0) = -\frac{Gr_0}{2\eta_0} \tag{6.34}$$

$$\Rightarrow \quad r_0 = -\frac{2m\dot{\gamma}_0^n}{G} \tag{6.35}$$

Another integration yields the expression for the velocity,

$$u_1(r) = -\left(-\frac{G}{4\eta_0}\right)r^2 - c_{1b} \quad , \tag{6.36}$$

where the second constant c_{1b} will be derived later using the fifth condition.
The solution for the power-law region is similar to the derivation of the velocity profile with the power-law model:

$$G = \frac{1}{r}\frac{\partial}{\partial r}\left(-rm\dot{\gamma}_2^n\right) \tag{6.37}$$

$$\Leftrightarrow \quad \dot{\gamma}_2 = \left(-\frac{Gr}{2m} - \frac{c_{2a}}{mr}\right)^{\frac{1}{n}} \tag{6.38}$$

The integration constant c_{2a} is determined by the third condition and using the expression for r_0 (eq. 6.35):

$$\dot{\gamma}_2(r_0) = \dot{\gamma}_0 \tag{6.39}$$

$$\Leftrightarrow \quad \left(-\frac{Gr_0}{2m} - \frac{c_{2a}}{mr_0}\right)^{\frac{1}{n}} = \dot{\gamma}_0 \tag{6.40}$$

$$\Leftrightarrow \quad \left[\left(-\frac{G}{2m}\right)\left(-\frac{2m\dot{\gamma}_0^n}{G}\right) + \left(-\frac{c_{2a}}{mr_0}\right)\left(-\frac{G}{2m\dot{\gamma}_0^n}\right)\right]^{\frac{1}{n}} = \dot{\gamma}_0 \tag{6.41}$$

$$\Leftrightarrow \quad \left(\dot{\gamma}_0^n + c_{2a}\frac{G}{2m^2\dot{\gamma}_0^n}\right)^{\frac{1}{n}} = \dot{\gamma}_0 \tag{6.42}$$

$$\Rightarrow \quad c_{2a} = 0 \tag{6.43}$$

Thus, the analytical expression for the shear rate in the power-law region is defined and $\dot{\gamma}_\infty$ at the radial position r_∞ are determined as

$$\dot{\gamma}_\infty = \dot{\gamma}_2(r_\infty) = \left(-\frac{Gr_\infty}{2m}\right)^{\frac{1}{n}} \tag{6.44}$$

$$\Rightarrow \quad r_\infty = -\frac{2m\dot{\gamma}_\infty^n}{G} \quad . \tag{6.45}$$

The velocity profile is obtained after integration:

$$u_2(r) = -\left(-\frac{G}{2m}\right)^{\frac{1}{n}} \frac{1}{1+\frac{1}{n}} r^{1+\frac{1}{n}} - c_{2b} \tag{6.46}$$

The wall region is again Newtonian. Thus, the derivation of u_3 is similar to the one of u_1:

$$G = \frac{1}{r}\frac{\partial}{\partial r}\left(-r\eta_\infty\dot{\gamma}_3\right) \tag{6.47}$$

$$\Leftrightarrow \quad \dot{\gamma}_3 = -\frac{Gr}{2\eta_\infty} - \frac{c_{3a}}{\eta_\infty r} \tag{6.48}$$

$$\tag{6.49}$$

The forth condition determines the integration constant c_{3a} using eq. (6.45) like

$$\dot{\gamma}_3(r_\infty) = \dot{\gamma}_\infty \tag{6.50}$$

$$\Rightarrow \quad -\frac{Gr_\infty}{2\eta_\infty} - \frac{c_{3a}}{\eta_\infty r_\infty} = \dot{\gamma}_\infty \tag{6.51}$$

$$\Rightarrow \quad \left(-\frac{G}{2m\dot{\gamma}_\infty^{n-1}}\right)\left(-\frac{2m\dot{\gamma}_\infty^n}{G}\right) + \left(-\frac{c_{3a}}{m\dot{\gamma}_\infty^{n-1}}\right)\left(-\frac{G}{2m\dot{\gamma}_\infty^n}\right) = \dot{\gamma}_\infty \tag{6.52}$$

$$\Rightarrow \quad \dot{\gamma}_\infty + c_{3a}\frac{G}{2m^2\dot{\gamma}_\infty^{2n-1}} = \dot{\gamma}_\infty \tag{6.53}$$

$$\Rightarrow \quad c_{3a} = 0 \quad . \tag{6.54}$$

A last integration yields the flow profile in the wall region:

$$u_3(r) = -\left(-\frac{G}{4\eta_\infty}\right) r^2 - c_{3b} \tag{6.55}$$

Here, the no-slip boundary condition at $r = R$ can be applied to find c_{3b}, i. e.

$$u_3(R) = 0 \tag{6.56}$$

$$\Leftrightarrow \quad -\left(-\frac{G}{4\eta_\infty}\right) R^2 - c_{3b} \tag{6.57}$$

$$\Leftrightarrow \quad c_{3b} = -\left(-\frac{G}{4\eta_\infty}\right) R^2 \tag{6.58}$$

$$\Rightarrow \quad u_3(r) = \left(-\frac{G}{4\eta_\infty}\right)\left(R^2 - r^2\right) \tag{6.59}$$

With the velocity fully defined in the Newtonian wall region, the remaining integration constants of the power-law and central region can be calculated using the last conditions. The sixth condition determines c_{2b} as follows:

$$u_2(r_\infty) = u_3(r_\infty) \tag{6.60}$$

$$\Leftrightarrow \quad -\left(-\frac{G}{2m}\right)^{\frac{1}{n}} \frac{1}{1+\frac{1}{n}} r_\infty^{1+\frac{1}{n}} - c_{2b} = \left(-\frac{G}{4\eta_\infty}\right)\left(R^2 - r_\infty^2\right) \tag{6.61}$$

$$\Rightarrow \quad c_{2b} = -\left(-\frac{G}{4\eta_\infty}\right)\left(R^2 - r_\infty^2\right) - \left(-\frac{G}{2m}\right)^{\frac{1}{n}} \frac{1}{1+\frac{1}{n}} r_\infty^{1+\frac{1}{n}} \tag{6.62}$$

The fifth condition determines c_{1b}:

$$u_1(r_0) = u_2(r_0) \tag{6.63}$$

$$\Leftrightarrow \quad -\left(-\frac{G}{4\eta_0}\right) r_0^2 - c_{1b} = -\left(-\frac{G}{2m}\right)^{\frac{1}{n}} \frac{1}{1+\frac{1}{n}} r_0^{1+\frac{1}{n}} - c_{2b} \tag{6.64}$$

$$\Rightarrow \quad c_{1b} = -\left(-\frac{G}{4\eta_0}\right) r_0^2 + \left(-\frac{G}{2m}\right)^{\frac{1}{n}} \frac{1}{1+\frac{1}{n}} r_0^{1+\frac{1}{n}} + c_{2b} \tag{6.65}$$

$$= -\left(-\frac{G}{4\eta_0}\right) r_0^2 - \left(-\frac{G}{4\eta_\infty}\right)\left(R^2 - r_\infty^2\right) + \left(-\frac{G}{2m}\right)^{\frac{1}{n}} \frac{1}{1+\frac{1}{n}} \left(r_0^{1+\frac{1}{n}} - r_\infty^{1+\frac{1}{n}}\right) \tag{6.66}$$

For conclusion, the radial velocity and the shear rate profile for the truncated power-law viscosity model are given by:

$$u_z(r) = \begin{cases} \left(-\frac{G}{4\eta_0}\right)\left(r_0^2 - r^2\right) + \zeta_1 + \zeta_2 & r \le r_0 \\ \left(-\frac{G}{2m}\right)^{\frac{1}{n}} \frac{1}{1+\frac{1}{n}} \left(r_\infty^{1+\frac{1}{n}} - r^{1+\frac{1}{n}}\right) + \zeta_1 & r_0 < r < r_\infty \\ \left(-\frac{G}{4\eta_\infty}\right)\left(R^2 - r^2\right) & r \ge r_\infty \end{cases} \tag{6.67}$$

$$\dot{\gamma}(r) = \begin{cases} -\frac{G}{2\eta_0} r & r \le r_0 \\ \left(-\frac{G}{2m}\right)^{\frac{1}{n}} r^{\frac{1}{n}} & r_0 < r < r_\infty \\ -\frac{G}{2\eta_\infty} r & r \ge r_\infty \end{cases} \tag{6.68}$$

where

$$\zeta_1 = \left(-\frac{G}{4\eta_\infty}\right)\left(R^2 - r_\infty^2\right) \tag{6.69}$$

$$\zeta_2 = \left(-\frac{G}{2m}\right)^{\frac{1}{n}} \frac{1}{1+\frac{1}{n}} \left(r_\infty^{1+\frac{1}{n}} - r_0^{1+\frac{1}{n}}\right) \tag{6.70}$$

$$r_0 = -\frac{2m\dot{\gamma}_0^n}{G} \tag{6.71}$$

$$r_\infty = -\frac{2m\dot{\gamma}_\infty^n}{G} \tag{6.72}$$

$$\tag{6.73}$$

Figure 6.2: Analytical solutions to the truncated power-law model for the velocity, the shear rate and the viscosity in a cylindrical channel with radius R. The normalization is with respect to the maximum velocity at the channel center, the shear rate at the channel wall and the highest Newtonian viscosity, i. e. the channel center viscosity for $n < 1$ and the wall viscosity for $n > 1$. The gray vertical lines indicate the transition points from power-law to Newtonian regions.

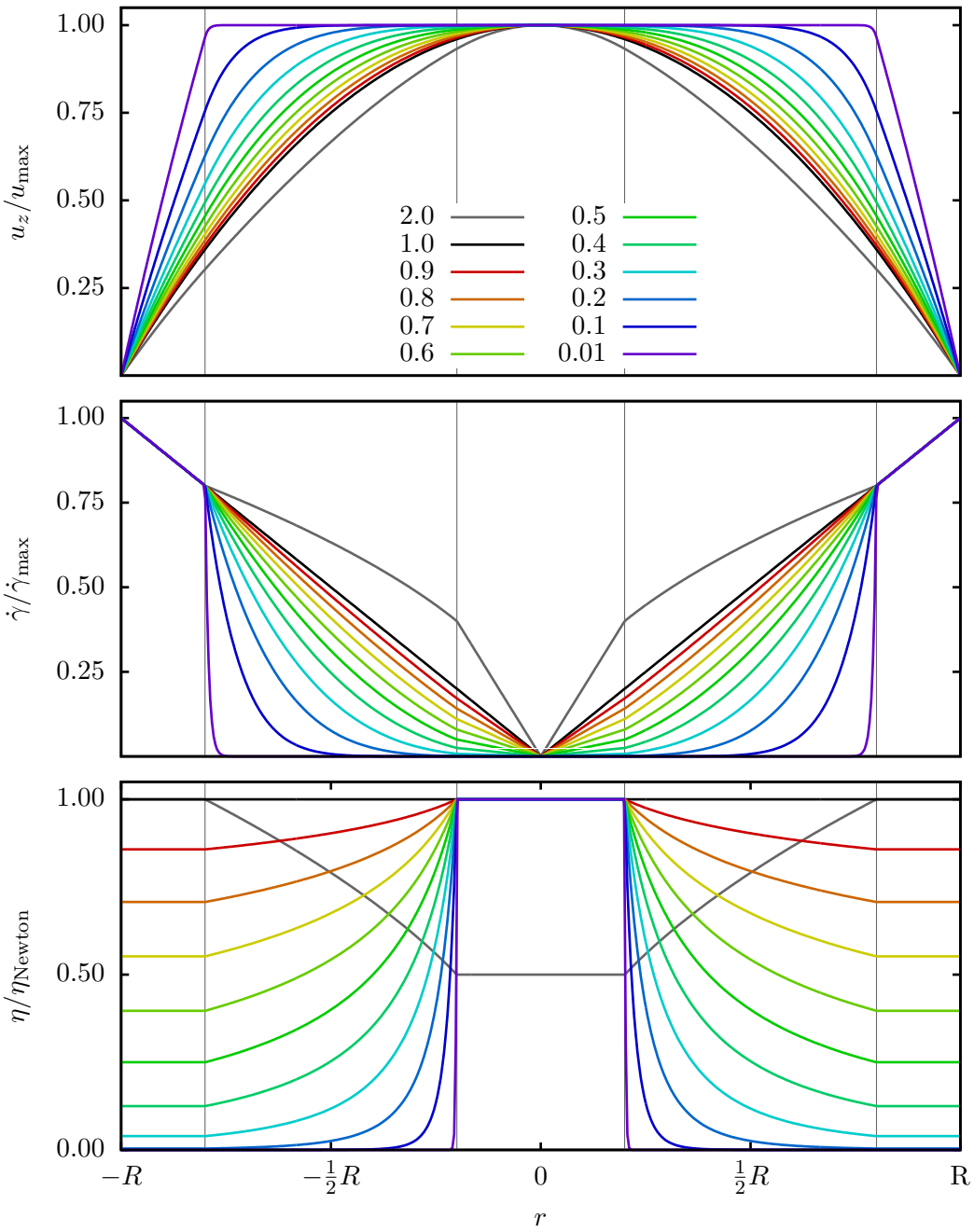

7 Basic kinetic theory

This chapter is meant to give a very brief overview of the underlying kinetic theory that is employed by the Lattice Boltzmann method to do computational fluid dynamics (CFD). Further explanations on the non-equilibrium thermodynamics can be found in [25] or [26], an introduction especially to the Boltzmann equation is given, for example, in [27]. The following parts are mostly summarized according to [26] and [7].

7.1 The Boltzmann equation

The kinetic theory lies between the microscopic and the macroscopic scale. In the macroscopic scale, the physical quantities of interest are usually measurable in an experiment. In contrast, microscopic theories are based on the motion of individual particles, e. g. the temporal evolution of position and momentum of every single molecule in a liquid or gas. The *mesoscopic* kinetic theory, however, describes the evolution of particle distributions in phase space that include the microscopic quantities, and macroscopic variables are obtained using multiscale analysis techniques like the Chapman-Enskog analysis method [28].
The core quantity, therefore, is the particle distribution function

$$f\left(\boldsymbol{x}, \boldsymbol{\xi}, t\right) \quad \text{, with} \quad [f] = \frac{\mathrm{kg\,s^3}}{\mathrm{m^6}} \quad . \tag{7.1}$$

It represents the density of particles at position $\boldsymbol{x}$ and time t that have a velocity $\boldsymbol{\xi} \in R^3$. The Boltzmann equation, which describes the time evolution of the distribution function f originates from the statistical mechanics, providing a complete treatment of dynamical processes in a monoatomic gas at sufficiently low density.
The general form of the Boltzmann equation is

$$\frac{\partial f}{\partial t} + \boldsymbol{\xi} \cdot \boldsymbol{\nabla}_x f + \frac{1}{m} \mathfrak{f}\left(x\right) \cdot \boldsymbol{\nabla}_\xi f = \left(\frac{\partial f}{\partial t}\right)_{\text{collision}} \quad , \tag{7.2}$$

where $\boldsymbol{\nabla}_x = \left(\partial_x, \partial_y, \partial_z\right)$ is the usual spatial gradient and $\boldsymbol{\nabla}_\xi = \left(\partial_{\xi_x}, \partial_{\xi_y}, \partial_{\xi_z}\right)$ the gradient in velocity space. $\mathfrak{f}\left(x\right)$ is an external force on a molecule of molecular mass m. The central term that determines the actual physics described by this equation is the so called *collision integral* $\left(\frac{\partial f}{\partial t}\right)_{\text{collision}}$, which is approximated to obtain kinetic models.
In this thesis, focus is put to the BGK approximation made by Bhatnagar, Gross and Krook [29], which leads to the hydrodynamic equations, i. e. the mass (continuity equation (4.3))

and momentum (NSE (4.12)) conservation.
The BGK approximation reads

$$\left(\frac{\partial f}{\partial t}\right)_{\text{collision}} = -\frac{1}{\tau}\left(f - f^{\text{eq}}\right) \quad , \tag{7.3}$$

which describes the evolution of the distribution function f towards its equilibrated form f^{eq}. The coefficient τ is the average time between collisions and often referred to as *relaxation time*, its inverse τ^{-1} is called *relaxation frequency*.
The macroscopic variables can be found by calculating the moments of the distribution function. The fluid *mass density* is given by the first moment, i. e.

$$\varrho\left(\boldsymbol{x}, t\right) = \int f\left(\boldsymbol{x}, \boldsymbol{\xi}, t\right) \, \mathrm{d}\boldsymbol{\xi} \quad , \tag{7.4}$$

the *momentum density* by its second moment, i. e.

$$\varrho\left(\boldsymbol{x}, t\right) \boldsymbol{u}\left(\boldsymbol{x}, t\right) = \int \boldsymbol{\xi} f\left(\boldsymbol{x}, \boldsymbol{\xi}, t\right) \, \mathrm{d}\boldsymbol{\xi} \quad , \tag{7.5}$$

and the *total energy density* by the third moment of f, i. e.

$$\varrho\left(\boldsymbol{x}, t\right) E\left(\boldsymbol{x}, t\right) = \int \left\|\boldsymbol{\xi}\right\|^2 f\left(\boldsymbol{x}, \boldsymbol{\xi}, t\right) \, \mathrm{d}\boldsymbol{\xi} \quad . \tag{7.6}$$

Furthermore, the *velocity average* of any quantity q is defined as

$$\langle q \rangle \coloneqq \frac{1}{\varrho\left(\boldsymbol{x}, t\right)} \int q f\left(\boldsymbol{x}, \boldsymbol{\xi}, t\right) \, \mathrm{d}\boldsymbol{\xi} \quad \textit{and} \tag{7.7}$$

$$\langle q \rangle_{\text{eq}} \coloneqq \frac{1}{\varrho\left(\boldsymbol{x}, t\right)} \int q f^{\text{eq}}\left(\boldsymbol{x}, \boldsymbol{\xi}, t\right) \, \mathrm{d}\boldsymbol{\xi} \tag{7.8}$$

in the equilibrium. The equilibrium distribution function f^{eq} is constructed using the assumption that it must be isotropic in velocity space in a reference frame moving with the velocity $\boldsymbol{\Xi}$. It is further chosen in a way that the actual hydrodynamic fields equal those in the local equilibrium:

$$\varrho = \langle 1 \rangle = \langle 1 \rangle_{\text{eq}} \tag{7.9}$$

$$\boldsymbol{u} = \langle \boldsymbol{\xi} \rangle = \langle \boldsymbol{\xi} \rangle_{\text{eq}} \tag{7.10}$$

$$\langle \left\|\boldsymbol{\xi} - \boldsymbol{\Xi}\right\|^2 \rangle = \langle \left\|\boldsymbol{\xi} - \boldsymbol{\Xi}\right\|^2 \rangle_{\text{eq}} \tag{7.11}$$

The last quantity describes the *internal energy density*. Thus, the local equilibrium distribution function is given as the three dimensional Gaussian distribution

$$f^{\text{eq}}\left(\boldsymbol{x}, \boldsymbol{\xi}, t\right) = \varrho\left(\boldsymbol{x}, t\right) \left(\frac{1}{2\pi RT}\right)^{\frac{3}{2}} e^{-\frac{\left\|\boldsymbol{\xi} - \boldsymbol{\Xi}\right\|^2}{2RT}} \quad , \tag{7.12}$$

with R denoting the ideal gas constant and T the temperature.
Now, the hydrodynamic equations can be derived from the BGK equation, i. e. the

Boltzmann equation (7.2) using the BGK approximation (7.3), on multiplying it with some function q and integrating over velocity space. That yields

$$\frac{\partial}{\partial t}\varrho\langle q\rangle = -\boldsymbol{\nabla}\cdot\varrho\langle\boldsymbol{\xi}q\rangle + \varrho\langle\boldsymbol{\xi}\cdot\boldsymbol{\nabla}q\rangle - \frac{1}{\tau}\varrho\left(\langle q\rangle - \langle q\rangle_{\mathrm{eq}}\right) \quad , \tag{7.13}$$

where $\boldsymbol{\nabla}$ denotes the usual spatial gradient and the dependency on $(\boldsymbol{x}, t)$ are left implicit for simplicity.
Using now the conditions of the equilibrium distribution from eq. (7.9) and choosing $q = 1$, the last term drops out, i. e. the collision term has no effect, and the continuity equation is obtained:

$$\frac{\partial}{\partial t}\varrho = -\boldsymbol{\nabla}\cdot(\varrho\boldsymbol{u}) \tag{7.14}$$

The momentum conservation is derived using $q = \boldsymbol{\xi}$, which yields

$$\frac{\partial}{\partial t}(\varrho\boldsymbol{u}) = -\boldsymbol{\nabla}\cdot\int\boldsymbol{\xi}\boldsymbol{\xi}f\,\mathrm{d}\boldsymbol{\xi} \quad . \tag{7.15}$$

Introducing the relative velocity $\boldsymbol{v} \coloneqq \boldsymbol{\xi} - \boldsymbol{\Xi}$ gives the desired equation,

$$\frac{\partial}{\partial t}(\varrho\boldsymbol{u}) = -\boldsymbol{\nabla}\cdot(\varrho\boldsymbol{u}\boldsymbol{u}) - \boldsymbol{\nabla}\cdot\underline{\sigma} \quad , \tag{7.16}$$

with the *stress tensor* defined by

$$\underline{\sigma} \coloneqq \int\boldsymbol{v}\boldsymbol{v}f\,\mathrm{d}\boldsymbol{\xi} \quad . \tag{7.17}$$

7.2 Chapman-Enskog procedure

To obtain the macroscopic Navier-Stokes equations from the BGK equation, a technique called the *Chapman-Enskog analysis* is utilized. The idea behind this method is that different physical phenomena are observed on different time scales.
Here, only the general background will be presented. A detailed introduction to the Chapman-Enskog procedure for the continuous Boltzmann equation can be read in [27]. The derivation of macroscopic quantities from the discretized Lattice Boltzmann equation can be found in [30].
As the method is a multiscale analysis with respect to the time, the time derivative is expressed in orders of the Knudsen number[1] β:

$$\partial_t = \beta\partial_{t_0} + \beta^2\partial_{t_1} + \mathcal{O}\left(\beta^3\right) \tag{7.18}$$

Spatial variations are all of the same order, thus one can rewrite the gradient simply as

$$\boldsymbol{\nabla} = \beta\boldsymbol{\nabla} \quad . \tag{7.19}$$

[1] The Knudsen number is the ratio of mean free path to a characteristic length in the system.

The distribution function is expanded about the equilibrium $f^{\mathrm{eq}} = f^{(0)}$:

$$f = f^{(0)} + \beta f^{(1)} + \beta^2 f^{(2)} + \mathcal{O}\left(\beta^3\right) \tag{7.20}$$

If these definitions are inserted into a Taylor expanded BGK equation, the macroscopic equations can be obtain by sorting the resulting term by the powers of β.
The first order,for example, yields the continuity equation, the second order the NSE. The equations for higher momenta of the distribution function can be obtained by extending the expansion to higher orders of β.

8 Numerical methods

In this chapter, the fundamentals of the Lattice Boltzmann method are briefly explained. The first part describes the basic principles that are employed to obtain the *Lattice Boltzmann equation* (LBE) from the kinetic theory. The second part gives a simple overview the *multiple relaxation time* (MRT) Lattice Boltzmann method that is used in the thesis. A special focus is put on the quantities that are necessary to include the inelastic viscosity models of chap. 5 into the numerical scheme. The content is mostly taken and summarized from the book of Timm Krüger et. al. [7]. The last part is about the immersed boundary method utilized to include cell motion into the simulation and the respective cell model.

8.1 Derivation of the Lattice Boltzmann equation

As stated already before, the simulation method is a discretized form of the BGK equation. The derivation will not be provided in its whole mathematical beauty, but rather in a simple form to offer the basic idea behind it.
Starting point is the BGK equation,

$$\frac{\partial f}{\partial t} + \boldsymbol{\xi} \cdot \boldsymbol{\nabla}_x f + \frac{1}{m} \mathfrak{f}(x) \cdot \boldsymbol{\nabla}_\xi f = -\frac{1}{\tau}\left(f - f^{\mathrm{eq}}\right) \quad , \tag{8.1}$$

where the external force term $\mathfrak{f}$ is set to zero. Note, that the collision term in this form is only valid for the *single relaxation time* Lattice Boltzmann scheme and will later be replaced by the MRT BGK operator. In the following, index notation will be used as it makes the numerical procedure more clear. The above equation then reads

$$\partial_t f + \xi_\alpha \partial_{x_\alpha} f = -\frac{1}{\tau}\left(f - f^{\mathrm{eq}}\right) \quad . \tag{8.2}$$

8.1.1 Velocity space discretization

In contrast to many other CFD methods, not only space and time need to be discretized for the Lattice Boltzmann method, but also the velocity space. This is done by defining a set of allowed velocities or directions that the populations can stream towards.
These *velocity sets* are usually denoted by DdQq, with the number of spatial dimensions d and the number of dimensions in velocity space q. The discretized velocities or *grid velocities* will be denoted by $\boldsymbol{c}_i$, where $i \in \{0, \ \ldots, \ q-1\}$.
Furthermore, the space is divided into a uniform grid in all dimensions, the distance between two grid nodes denoted by Δx. The $\boldsymbol{c}_i$ are therefore chosen such that they point from one lattice point to another, usually adjacent or diagonal, and c_0 points to the

current node, i. e. the resting particle distribution. Fig. 8.1 shows the D3Q19 velocity set that is used in this work.
Velocity space discretization is done mathematically using a Hermite series expansion[2] of the particle distribution function, i. e.

$$f(\boldsymbol{x}, \boldsymbol{\xi}, t) \approx \omega(\boldsymbol{\xi}) \sum_{n=0}^{N} \frac{1}{n!} \boldsymbol{a}^{(n)}(\boldsymbol{x}, t) \cdot \boldsymbol{H}^{(n)}(\boldsymbol{\xi}) \quad , \tag{8.3}$$

where $\boldsymbol{a}^{(n)}(\boldsymbol{x}, t)$ are the series coefficients and $\omega(\boldsymbol{\xi}) = (2\pi)^{-\frac{1}{2}} e^{-\frac{1}{2}\|\boldsymbol{\xi}\|^2}$ is a *weight function* or *generating function* used to obtain the Hemite polynomial of n-th order via

$$\boldsymbol{H}^{(n)}(\boldsymbol{\xi}) = (-1)^n \frac{1}{\omega(\boldsymbol{\xi})} \boldsymbol{\nabla}^{(n)} \omega(\boldsymbol{\xi}) \quad . \tag{8.4}$$

The special properties of the Hermite polynomials, e. g. the orthogonality, make the series expansion possible. Applying the mathematical procedure that is described in detail in [7], one finds the particle distribution function discretized in velocity space as

$$f_i(\boldsymbol{x}, t) = \frac{w_i}{\omega(\boldsymbol{c}_i)} f(\boldsymbol{x}, \boldsymbol{c}_i, t) \quad , \tag{8.5}$$

and its equilibrium form

$$f_i^{\mathrm{eq}}(\boldsymbol{x}, t) = w_i \varrho(\boldsymbol{x}, t) \left(1 + \frac{c_{i\alpha} u_\alpha(\boldsymbol{x}, t)}{{c_\mathrm{s}}^2} + \frac{u_\alpha(\boldsymbol{x}, t)\, u_\beta(\boldsymbol{x}, t) \left(c_{i\alpha} c_{i\beta} - {c_\mathrm{s}}^2 \delta_{\alpha\beta} \right)}{2{c_\mathrm{s}}^2} \right) \quad , \tag{8.6}$$

where w_i are weighting factors for each of the velocity directions i that depend on the chosen velocity set. The parameter c_s denotes the lattice speed of sound which is defined by the space and time discretization as

$$c_\mathrm{s} = \frac{1}{\sqrt{3}} \frac{\Delta x}{\Delta t} \quad . \tag{8.7}$$

The remaining variables ρ and u_α are the fluid mass density and the macroscopic fluid velocity (x_α-component), respectively, and need to be calculated from the moments of the discretized particle distribution function. f_i and f_i^{eq} are usually referred to as *population of particles moving in direction* $\boldsymbol{c}_i$, or just *populations*, when speaking abut the numerical quantity.
The calculation of the moments of the populations after velocity discretization reduces to

[2] An expansion up to the 3rd order, i. e. ($N = 3$, is sufficient to fulfill the moment conservation up to Navier-Stokes hydrodynamics.

simple finite sums that are straight forward to implement:

$$\varrho = \sum_i f_i = \sum_i f_i^{\mathrm{eq}} \tag{8.8}$$

$$\varrho \boldsymbol{u} = \sum_i f_i \boldsymbol{c}_i = \sum_i f_i^{\mathrm{eq}} \boldsymbol{c}_i \tag{8.9}$$

8.1.2 Discretization in space and time

After discretization, the discrete-velocity BGK equation reads

$$\partial_t f_i + c_{i\alpha} \partial_\alpha f_i = -\frac{1}{\tau} \left(f_i - f_i^{\mathrm{eq}} \right) \quad . \tag{8.10}$$

The left hand side can be converted into a total derivative with respect to the variable Λ, using the method of characteristics:

$$\frac{\mathrm{d}f_i}{\mathrm{d}\Lambda} = \left(\frac{\partial f_i}{\partial t} \right) \underbrace{\frac{\mathrm{d}t}{\mathrm{d}\Lambda}}_{=1} + \left(\frac{\partial f_i}{\partial x_\alpha} \right) \underbrace{\frac{\mathrm{d}x_\alpha}{\mathrm{d}\Lambda}}_{=c_{i\alpha}} = -\frac{1}{\tau} \left(f_i - f_i^{\mathrm{eq}} \right) = \Omega_i \tag{8.11}$$

The abbreviation for the BGK operator $\Omega_i(\boldsymbol{x}, t)$ is introduced for better readability of the equations. Integration from $\Lambda = 0$ with $t(\Lambda = 0) = t_0$ and $\boldsymbol{x}(\Lambda = 0) = \boldsymbol{x}_0$ to $\Lambda = \Delta t$ yields

$$f_i \left(\boldsymbol{x}_0 + \frac{\partial \boldsymbol{x}}{\partial \Lambda} \Delta\Lambda, t_0 + \frac{\partial t}{\partial \Lambda} \Delta\Lambda \right) - f_i(\boldsymbol{x}_0, t_0) = \int_0^{\Delta t} \Omega_i \left(\boldsymbol{x}_0 + \frac{\partial \boldsymbol{x}}{\partial \Lambda} \Lambda, t_0 + \frac{\partial t}{\partial \Lambda} \Lambda \right) \mathrm{d}\Lambda \quad , \tag{8.12}$$

replacing the derivatives in the coordinate functions and further considering that the integration starting point is arbitrary gives

$$f_i(\boldsymbol{x} + \boldsymbol{c}_i \Delta t, t + \Delta t) - f_i(\boldsymbol{x}, t) = \int_0^{\Delta t} \Omega_i(\boldsymbol{x} + \boldsymbol{c}_i \Lambda, t + \Lambda) \, \mathrm{d}\Lambda \quad . \tag{8.13}$$

From this point, the right hand side has to be approximated. The most simple way is the approximation of the collision operator by a single point $\Omega_i(\boldsymbol{x}, t)$, which yields the *Lattice Boltzmann equation* for the BGK operator

$$f_i(\boldsymbol{x} + \boldsymbol{c}_i \Delta t, t + \Delta t) - f_i(\boldsymbol{x}, t) = -\frac{\Delta t}{\tau} \left[f_i(\boldsymbol{x}, t) - f_i^{\mathrm{eq}}(\boldsymbol{x}, t) \right] \quad . \tag{8.14}$$

The first term on the left-hand side are the so-called *post-collision populations*, usually denoted by $f_i^\star$, the second term are the *pre-collision populations*, abbreviated as just f_i.

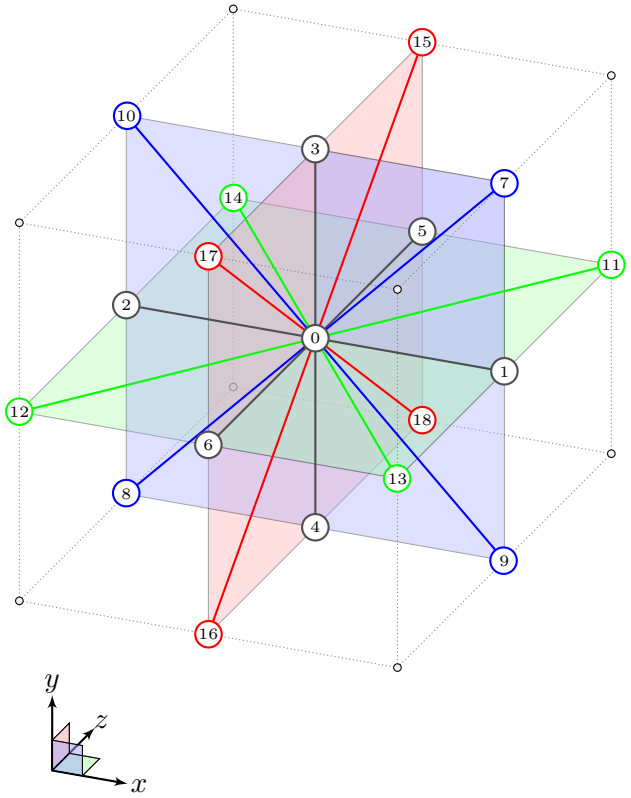

Figure 8.1: Discretized velocities in the D3Q19 velocity set shown for a $3 \times 3 \times 3$ cube. The numbers in the circles correspond to the indices of the populations used in the ESPResSo software package.

This notation shortens the LBE to

$$f_i^\star = f_i - \frac{\Delta t}{\tau}\left(f_i - f_i^{\mathrm{eq}}\right) \quad , \tag{8.15}$$

which is a form of the equation that can directly be implemented, as the right-hand side contains all known variables at a given time step that are needed to calculate the populations for the next time step.

8.2 LBM with external forces

As yet, The presence of external forces in the simulated system has been neglected for simplicity. The mathematical treatment utilizes the same means for discretization as in the derivation of the LBE. A structured derivation is given in [7], in the present work, only the additional terms in the important equations are presented.
Let $\mathfrak{f} = \mathfrak{f}(\boldsymbol{x}, t)$ be the external force density, then the calculation of the velocity field

includes an additional term, while the density calculation stays the same:

$$\varrho = \sum_i f_i \tag{8.16}$$

$$\boldsymbol{u} = \frac{1}{\varrho} \sum_i f_i \boldsymbol{c}_i + \frac{\mathfrak{f}}{2\varrho} \Delta t \tag{8.17}$$

The Lattice Boltzmann equation (8.15) is extended with a source term, giving

$$f_i^\star = f_i - \frac{\Delta t}{\tau} \left(f_i - f_i^{\mathrm{eq}} \right) + \Delta t S_i \quad , \tag{8.18}$$

with the last term defined as

$$S_i = \left(1 - \frac{\Delta t}{2\tau} \right) w_i \left(\frac{c_{i\alpha}}{{c_\mathrm{s}}^2} + \frac{\left(c_{i\alpha} c_{i\beta} - {c_\mathrm{s}}^2 \delta_{\alpha\beta} \right) u_\beta}{{c_\mathrm{s}}^4} \right) \mathfrak{f}_\alpha \quad . \tag{8.19}$$

Note that the velocity discretized forcing term $\mathfrak{f}_i$ is related to the source term via

$$S_i = \left(1 - \frac{\Delta t}{2\tau} \right) \mathfrak{f}_i \quad . \tag{8.20}$$

8.3 Multiple relaxation time Lattice Boltzmann

It was stated before that the actual collision operator of the simulation method in this thesis is not the BGK operator with a single relaxation frequency $\omega = \tau^{-1}$, but rather an extended version of this scheme [31]. The main extension to the LBE is that the populations are mapped to moment space before collision and transformed back before streaming.
The transformation into moment space is performed using the $q \times q$-matrix $\underline{\mathrm{M}}$ and calculating the k-th moment from the populations via

$$m_k = \sum_i M_{ki} f_i \quad , \tag{8.21}$$

or, using the vector notation for the populations $\boldsymbol{f} = (f_0, \ \ldots, \ f_{q-1})^\mathsf{T}$,

$$\boldsymbol{m}\left(\boldsymbol{x}, t\right) = \underline{\mathrm{M}} \boldsymbol{f}\left(\boldsymbol{x}, t\right) \quad \text{and} \tag{8.22}$$

$$\boldsymbol{m}^{\mathrm{eq}}\left(\boldsymbol{x}, t\right) = \underline{\mathrm{M}} \boldsymbol{f}^{\mathrm{eq}}\left(\boldsymbol{x}, t\right) \quad . \tag{8.23}$$

The transformation matrix can be constructed using different methods, e. g. the Gram-Schmidt procedure or, again, Hermite polynomials. Ten of the calculated models are connected to hydrodynamic quantities, i. e. the density, the three velocity components and the six components of the symmetrical stress tensor. The remaining modes are often referred to as *ghost* or *non-hydrodynamic* moments, as they do not affect the Navier-Stokes hydrodynamics.

The Lattice Boltzmann equation can be rewritten the following way to include the mode transformation:

$$\boldsymbol{f}^\star - \boldsymbol{f} = -\underbrace{\underline{\mathrm{M}}^{-1}\underline{\mathrm{M}}}_{=\underline{\mathrm{I}}}\omega\left(\boldsymbol{f} - \boldsymbol{f}^{\mathrm{eq}}\right)\Delta t \tag{8.24}$$

$$= -\underline{\mathrm{M}}^{-1}\omega\left[\underline{\mathrm{M}}\boldsymbol{f} - \underline{\mathrm{M}}\boldsymbol{f}^{\mathrm{eq}}\right]\Delta t \tag{8.25}$$

$$= -\underline{\mathrm{M}}^{-1}\underbrace{\omega\underline{\mathrm{I}}}_{=\underline{\mathrm{S}}}\left(\boldsymbol{m} - \boldsymbol{m}^{\mathrm{eq}}\right)\Delta t \tag{8.26}$$

$$= -\underline{\mathrm{M}}^{-1}\underline{\mathrm{S}}\left(\boldsymbol{m} - \boldsymbol{m}^{\mathrm{eq}}\right)\Delta t \tag{8.27}$$

The *relaxation (frequency) matrix* $\underline{\mathrm{S}} = \mathrm{diag}\left(\omega,\ \ldots,\ \omega\right)$ is a diagonal $q \times q$-matrix with the diagonal elements being the relaxation frequency ω of the BGK operator. The term $\underline{\mathrm{S}}\left(\boldsymbol{m} - \boldsymbol{m}^{\mathrm{eq}}\right)$ describes the full relaxation of the moments, i. e. the collision, and $\underline{\mathrm{M}}^{-1}$ transformes the collided moments back into population space.
The idea behind MRT is now, straightforward, replacing the single relaxation frequency ω by multiple ones for the different hydrodynamic and ghost moments:

$$\underline{\mathrm{S}} = \mathrm{diag}\left(\omega_0,\ \omega_1,\ \ldots,\ \omega_{q-1}\right) \tag{8.28}$$

This makes for controlling the relaxation of the conserved quantities, i. e. density and momentum, and the rest, e. g. the shear moments, separately.
Chapman-Enskog analysis of the LBE recovers that pressure p, (shear) viscosity η and bulk viscosity η_{B} are connected to the simulation parameters as follows: [7, 32]

$$p = \varrho {c_{\mathrm{s}}}^2 \tag{8.29}$$

$$\eta = \varrho {c_{\mathrm{s}}}^2\left(\frac{1}{\omega_{\mathrm{S}}} - \tfrac{1}{2}\right) \tag{8.30}$$

$$\eta_{\mathrm{B}} = \varrho {c_{\mathrm{s}}}^2\left(\frac{1}{\omega_{\mathrm{B}}} - \tfrac{1}{2}\right) - \frac{\eta}{3} \tag{8.31}$$

$$\tag{8.32}$$

Here, ω_{B} denotes the relaxation frequency of the bulk moments.
In order to include the shear thinning fluid models of this thesis, only the relaxation frequency of the shear moments ω_{S} has to be modified, which is explained in the next section.

8.4 Inlusion of Shear Thinning fluid models

Several inelastic viscosity models have been introduced in 5.3 and all of them depend on the rate of shear $\dot{\gamma}$ as variable and a set of different, fixed, parameters.
This section explains how the shear rate can be obtained in Lattice Boltzmann simulations, and further, that it can be obtained locally. There exist several methods to obtain the strain rate tensor ϵ in Lattice Boltzmann simulations, two of which are analyzed in detail

in [33]. A further analysis of the strain rate in Lattice Boltzmann simulations is given in [30] and [30]. In this thesis, the Chai-method [34] is utilized and outlined in the following. The MRT Lattice Boltzmann equation reads

$$\boldsymbol{f}^{\star} - \boldsymbol{f} = -\underline{\mathrm{M}}^{-1}\underline{\mathrm{SM}}\left(\boldsymbol{f} - \boldsymbol{f}^{\mathrm{eq}}\right)\Delta t \quad , \tag{8.33}$$

or, for every velocity component i

$$f_i^{\star} - f_i = -\sum_j \left(\underline{\mathrm{M}}^{-1}\underline{\mathrm{SM}}\right)_{ij}\left(f_j - f_j^{\mathrm{eq}}\right)\Delta t \quad . \tag{8.34}$$

This mixture of the matrix and component notation is not completely consistent with this thesis, but it used in the main reference [34] and underlines the way of implementing the strain rate calculation. Its correctness is easily verified by inserting the BGK operator for the relaxation matrix $\underline{\mathrm{S}} = \omega\underline{\mathrm{I}} = \frac{1}{\tau}\underline{\mathrm{I}}$. This reduces the matrix multiplications to $\left(\underline{\mathrm{M}}^{-1}\underline{\mathrm{SM}}\right)_{ij} = \frac{1}{\tau}\delta_{ij}$ and the sum remains to be the SRT BGK operator $\frac{1}{\tau}\left(f_i - f_i^{\mathrm{eq}}\right)$.
The second order accurate [30] equation for the components of the strain rate tensor is given by

$$\epsilon_{\alpha\beta} = -\frac{1}{2\varrho {c_{\mathrm{s}}}^2 \Delta t}\sum_i c_{i\alpha}c_{i\beta}\sum_j \left(\underline{\mathrm{M}}^{-1}\underline{\mathrm{SM}}\right)_{ij}\left(f_j - f_j^{\mathrm{eq}}\right) \quad , \tag{8.35}$$

where $\alpha, \beta = x, y, z$ denote the spatial components and $i, j \in [0, \ldots, q-1]$ the velocity space components. The last sum on the right hand side is given by the Lattice Boltzmann equation, thus,

$$\epsilon_{\alpha\beta} = \frac{1}{2\varrho {c_{\mathrm{s}}}^2 \Delta t^2}\sum_i c_{i\alpha}c_{i\beta}\left(f_i^{\star} - f_i\right) \quad . \tag{8.36}$$

Using the equations from 5.2.1, the strain rate tensor can then be used to calculate the shear rate $\dot{\gamma}$ via

$$\dot{\gamma} = \sqrt{2\,\mathrm{II}_{\epsilon}} = \sqrt{2\sum_{\alpha}\sum_{\beta}\epsilon_{\alpha\beta}\epsilon_{\alpha\beta}} \quad , \tag{8.37}$$

and the local viscosity $\eta\left(\dot{\gamma}\right)$ can be determined.
Inverting eq. (8.29) finally yields an expression for the shear relaxation frequency,

$$\omega_{\mathrm{S}} = \left(\frac{2\eta}{\varrho {c_{\mathrm{s}}}^2} + 1\right)^{-1} \quad , \tag{8.38}$$

that is used for the relaxation of the moments during the next time step.

8.5 Boundary conditions

In the simulations in this thesis, geometries with different boundary conditions are used. The numerical algorithms presented in the following are implemented in the simulations package ESPResSo . A 2-dimensional depiction of the lattice near a boundary is shown in the figures 8.2 and 8.3. The domain is divided into two parts: fluid nodes and solid nodes. The boundaries algorithms ensure that the restrictions on the normal and tangential velocity components are fulfilled on the solid nodes. The actual position of the physical wall is approximately midway between solid and fluid nodes. This choice makes the method formally second order accurate [7].

8.5.1 Bounce-back algorithm

The realization of the no-slip boundary condition, i. e. vanishing velocity components tangential and normal to the boundary at the wall, is done using the bounce-back algorithm described in the following. If a component of the post-collision populations $f_i^\star$ is streaming towards a boundary node, the populations are bounced back towards the lattice node they have come from and their directions are inverted, as depicted in fig. 8.2 by the blue arrows.

8.5.2 Extended bounce-back algorithm

For a free-slip boundary condition, i. e. when the normal velocity component vanishes but the tangential component is finite, an extended version of the bounce-back algorithm is used. Similar to the bounce-back, the populations streaming towards a wall invert their direction perpendicular to the wall. But instead of bouncing back to the initial lattice node, they still propagate in tangential direction. As shown in fig. 8.3, the populations are reflected specularly at the physical boundary [7].

Figure 8.2: Decpiction of the bounce-back algorithm shown in 2D for simplicity. Post-collision populations that move towards a wall during the propagation are bounced back to the node they have come from and their direction is reversed to obtain the post-streaming populations. Red arrows denote populations that are not affected by the bounce-back algorithm and blue arrows denote populations that are bounced back.

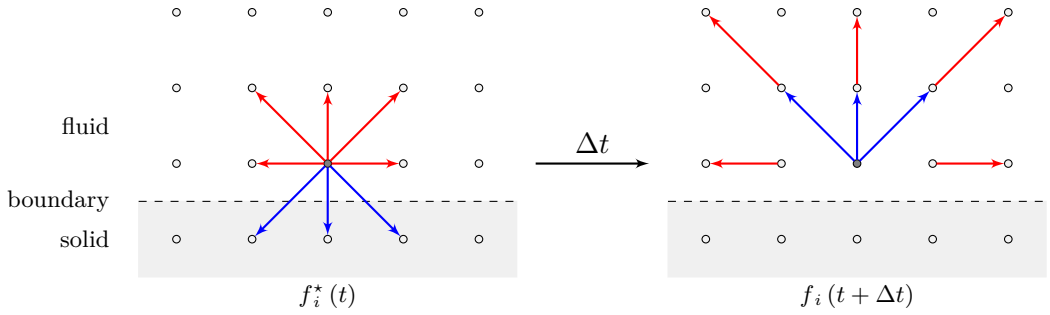

Figure 8.3: Decpiction of the extended bounce-back algorithm. Post-collision populations that move towards a wall during the propagation are reflected from the wall towards the next node, i. e. only the perpendicular component of their direction is inverted.

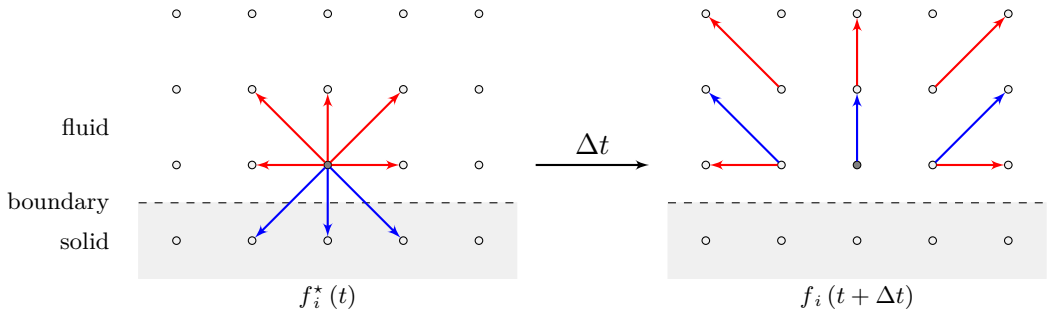

8.6 Lattice Boltzmann Simulation

Knowing the theory behind the method and all important equations given in the last sections, a brief outline of an actual simulation step shall be provided in the following the depiction in fig. 8.4.
A hydrodynamic simulation begins, of course, with the correct initialization of all parameters and simulation variables, which is not gone into for this thesis but described rich in detail in [7].
In every subsequent time step, the following steps are performed:

1. First of all, the time t is updated, incrementing it by the time step Δt
2. Then, the additional force terms $\mathfrak{f}$ are computed. Hydrodynamic forces can be either due to real external forces, i. e. gravity or, as it is implemented in ESPResSo , a pressure gradient interpreted as body force. Or contributions can be a consequence of particle-fluid interactions, e. g. when cells are included into the fluid simulation. In the present work, cell motion and cell-fluid interaction are computed using the immersed-boundary method (IBM).
3. Given the force contributions, the hydrodynamic moments can be calculated from the pre-collision populations f_i and $\mathfrak{f}$. This includes the computation of the fluid mass density ϱ, the macroscopic velocity field $\boldsymbol{u}$ and, especially important for this thesis, the strain rate tensor $\underline{\epsilon}$.
   As described above, the strain rate tensor is used to update the shear relaxation frequency ω_S according to the local shear rate and the chosen viscosity model.
4. The equilibrium populations are computed from the macroscopic fields.
5. Then, the source terms that enter the collision are calculated.
6. Afterwards, the main parts of the Lattice Boltzmann algorithm are performed, i. e. collision and propagation. The realization of the collision depends on the chosen LB scheme:
   - Using SRT, the collision is performed in population space.
   - For MRT, at first, the populations are mapped onto the hydrodynamic moment space. Then they are relaxed regarding their individual relaxation frequency. Finally they are transformed back to obtain the post-collision populations $f_i^\star$.
7. During the last step, the post-collision populations $f_i(\boldsymbol{x}, t)$ are propagated towards their respective direction $\boldsymbol{c}_i$ and assigned to the pre-collision populations of the next time step $f_i(\boldsymbol{x} + \boldsymbol{c}_i \Delta t, t + \Delta t)$.
8. The final step also includes the treatment of boundary conditions using the respective algorithms.

After the streaming step, there is usually done some output of the desired data that was computed during the time step. The steps are performed for each time step until the maximum number of time steps is reached or a convergence criterion is fulfilled.

Figure 8.4: Depiction of the calculations that are performed during one Lattice Boltzmann time step, differentiating between SRT and MRT method. The additional calculations that are added to the original algorithm in this thesis are highlighted.

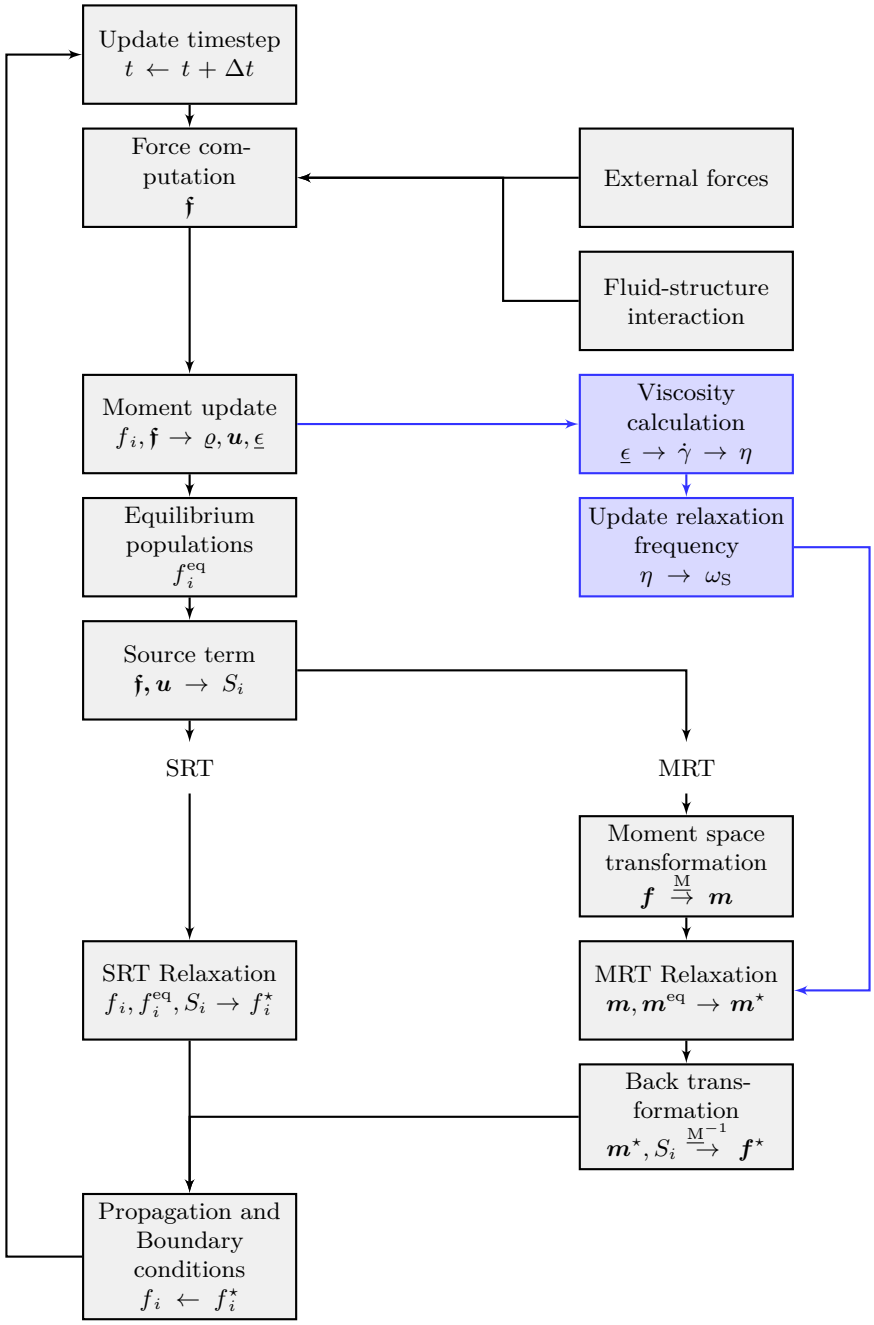

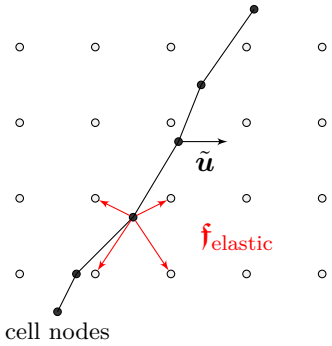

Figure 8.5: A cell consisting of nodes immersed into the uniform lattice. The membrane is advected with the interpolated macroscopic fluid velocity $\tilde{\boldsymbol{u}}(\boldsymbol{x})$. The deformation of the cell due to this motion, in turn, causes the elastic restoring forces $\mathbf{f}_{\text{elastic}}(\boldsymbol{r})$ to react on the fluid. This is done by spreading the force to the adjacent lattice nodes.

8.7 Immersed-boundary method

Later in this thesis, stem cells will be represented using spherical membranes. Therefore, this section briefly summarizes the idea behind the immersed-boundary method that is used to model fluid-structure interactions. A detailed derivation of the governing equations can be found in [35] and [36].
If one considers a cell in a fluid, both the cell is deformed by the hydrodynamic forces of the surrounding fluid and the elastic restoring forces of the cell, in turn, react on the fluid. This behavior can be formulated in the (continuous) equation

$$\frac{\partial \boldsymbol{r}}{\partial t} = \boldsymbol{u}(\boldsymbol{r}(t), t) \quad , \tag{8.39}$$

where $\boldsymbol{r}(t)$ denotes the position of the cell membrane at time t and $\boldsymbol{u}$ is the macroscopic velocity field of the fluid. The cell is therefore simply advected with the velocity of the surrounding fluid that in turn depends on the current shape of the cell. This affects the fluid due to its deformation and the resulting elastic restoring forces. That is equivalent to saying that a no-slip boundary condition is fulfilled at the cell surface $\boldsymbol{r}$.
The cell, however, needs to be discretized in order to simulate it. Several methods for object discretization are mentioned in [37], in the present thesis, a triangulated mesh as shown in fig. 8.6 is used.
In Lattice Boltzmann simulations, an arbitrary shape could in principle be discretized using a staircase approximation of the structure, but the immersed boundary method is easy to implement and makes for a smoother and more accurate representation of the cell's shape.
Fig. 8.5 shows an arbitrarily shaped membrane that is immersed into the uniform Lattice Boltzmann grid. In order to calculate the cell movement correctly, the macroscopic velocity field is interpolated to obtain values between neighboring lattice nodes using an eight-point stencil. Then, the elastic forces that react on the fluid due to the cell deformation are spread to the neighboring lattice nodes for each membrane node.

In the context of this thesis, it is important to note that the fluid inside the cell is the same as outside, i. e. in general a non-Newtonian fluid.

Figure 8.6: Discretization and subdivision of the spherical cell model. Starting from an icosahedron, every surface triangle is split into 4 triangles which are then radially shifted to match the circumsphere of the cell. The number of faces is given by N_f. (cf. [36])

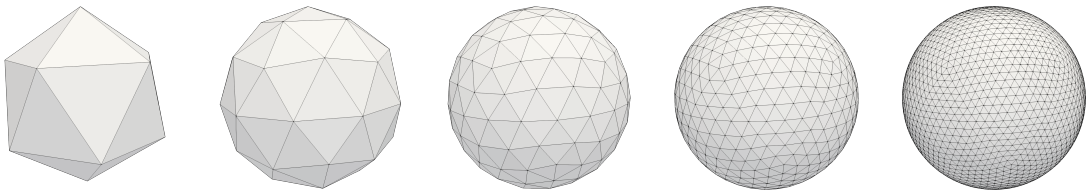

$N_f = 20$ $N_f = 80$ $N_f = 320$ $N_f = 1280$ $N_f = 5120$

8.8 Cell model

The above mentioned elastic restoring forces of the discretized cell are the last simulation-related part that needs to be defined in the following. The implementation used in this thesis is oriented at Krüger's PhD thesis [36].
To account for local forces due to shear elasticity and area dilatation, the Skalak model [38] is employed. It models the energy density as

$$\varepsilon_{\mathrm{S}} = \frac{\kappa_1}{12}\left(\mathrm{I}_D^2 + 2\mathrm{I}_D - 2\mathrm{II}_D\right) + \frac{\kappa_2}{12}\mathrm{II}_D^2 \quad , \tag{8.40}$$

where the coefficients κ_1 and κ_2 are the elastic shear modulus and area dilation modulus, respectively. I_D and II_D are the first and second invariant of the *displacement gradient tensor* $\underline{\mathrm{D}}$, which is a measure for the deformation of the cell with respect to its reference shape.
To account for the bending rigidity of the lipid bilayer of a cell, the Helfrich model [39] for the bending energy density ε_{B} is utilized, its scale given by the bending modulus κ_{B}:

$$\varepsilon = \frac{\kappa_{\mathrm{B}}}{2}\left(H - H^{(0)}\right)^2 \tag{8.41}$$

Here, H and $H^{(0)}$ are the trace of the surface curvature tensor and the spontaneous curvature, respectively. The implementaion used in this thesis is the one of Gompper and Kroll [40], which is also described as "Method B" in [41].
Finally, the volume of the cell is kept approximately constant using

$$E_{\mathrm{V}} = \frac{\kappa_{\mathrm{V}}}{2}\frac{\left(V - V^{(0)}\right)^2}{V^{(0)}} \tag{8.42}$$

as expression for the volume energy E_{V} [42]. This term introduces an energetic penalty for deviations from the reference volume $V^{(0)}$ that is scaled via the empirical volume modulus κ_{V}.

Part III

Implementation of shear thinning fluid models into ESPResSo

9 The software package ESPResSo

The software package ESPResSo [43] is originally a molecular dynamics program for simulations of coarse-grained atomistic models for soft matter research, but it has been extended with a lot of other features, including a Lattice Boltzmann and immersed-boundary algorithm. The GPU implementation and the parallelized CPU implementation are its main advantages, as they make large scale simulations possible in a considerable amount of time.
The control interface in the present version is realized using the script language TCL.
The main LB implementation uses the D3Q19 velocity set as depicted in fig. 8.1 and the MRT algorithm. It includes external forces, a bounce-back boundary algorithm, extended bounce-back (only for GPU) and an immersed-boundary algorithm, to just mention the parts used in the present work.
The time step algorithm follows in principle the depiction in fig. 8.4, the only notable difference is that ESPResSo combines the back-transformation and the propagation step.

Figure 9.1: The logo of the ESPResSo software package was made by the developers using the software itself.[1]

10 Implementation of the shear thinning fluid models

This chapter provides a brief overview of how the actual implementation of the shear thinning viscosity models is realized. The first section is meant to serve as a short usage guide, explaining the implemented commands that the user is able to execute during initialization and simulation. The remaining parts focus on the actual modification of the source code of the ESPResSo software package.

10.1 Usage

This section explains all the commands that can be used in the `tcl`-script to activate the `SHEAR_THINNING` features to define the fluid properties or print specified output data, respectively. Every instruction *must* begin with `stmodel` and is followed by one of the commands listed in tab. 10.1.
An example for setting up a the fluid with the power-law model would be:

```
stmodel PowerLaw 1.2e-3 0.4
```

This sets the consistency parameter to 1.2×10^{-3} and the power-law exponent to 0.4.
Two of the implemented models need some further explanation:

1. The actual implementation of the truncated power-law model does not use the limiting shear rates $\dot{\gamma}_0$ and $\dot{\gamma}_\infty$ as in the definition in eq. (5.13), but rather expects the user to set a minimum and maximum viscosity, $\nu_{\min}$ and $\nu_{\max}$, respectively. It is, nevertheless, possible to convert these parameters into each other by simply calculating

$$\nu_{\max} = \tfrac{1}{\varrho}\eta_0 = \tfrac{1}{\varrho} m \dot{\gamma}_0^{n-1} \quad \text{and}$$
$$\nu_{\min} = \tfrac{1}{\varrho}\eta_\infty = \tfrac{1}{\varrho} m \dot{\gamma}_\infty^{n-1} \quad .$$

   Also note that this equation is only true for a shear thinning fluid, i. e. $n < 1$. For shear thickening behavior, $\nu_{\max}$ and $\nu_{\min}$ switch places.

2. The `inout` model is not primarily part of the `SHEAR_THINNING` feature, but utilizes its function to set different Newtonian viscosites at a given positions. It can be used to account for the viscosity difference between the inside and outside of cells and is part of the method presented in [44].

To output macroscopic quantities in a VTK-format, the keywords are

```
stmodel print vtk <quantity> <filename> <conversion-factor>  .
```

The available fields for output are the velocity vector field and the scalar fields shear rate, viscosity and relaxation frequency. Additional to the output file, a conversion factor is required. This is done for convenience: Converting simulation output data between the different formats can get tedious, providing the conversion factor is rather simple. If nevertheless the output in simulation units is desired, the conversion factor is simply 1. Another useful output that comes in handy if the viscosity is hard to approximate analytically for a simulation, e. g. if a complicated geometry is used, is provided using the command

```
stmodel print timestep_recommendation <filename>  .
```

It prints the maximum and minimum viscosity present in the simulation box and gives a rough estimate on how large time step should be chosen. During the tests performed on the power-law model, a time step chosen too large resulted in the velocity profile shifted about a constant value. It appeared, however, that the minimum viscosity was a sufficient reference to tune the time step according to the method presented in section 13.5.

Table 10.1: All possible commands that can be used to incorporate the features of the `SHEAR_THINNING` extension with the corresponding arguments and their meaning. Each command must begin with `stmodel`. $\tilde{q}$ denotes the quantity q in dimensionless simulation units, with c_q being the conversion factor.

command	arguments					effect
`Standard` (`std`)	$\tilde{\nu}$					Sets up the internal data structures for the chosen viscosity model with the given parameters. For the model definitions see chap. 5.3
`PowerLaw` (`pl`)	$\tilde{m}$	$\tilde{n}$				
`Truncated` (`trunc`)	$\tilde{m}$	$\tilde{n}$	$\tilde{\nu}_{\min}$	$\tilde{\nu}_{\max}$		
`Carreau-Yasuda` (`cy`)	$\tilde{K}$	$\tilde{a}_1$	$\tilde{\nu}_0$	$\tilde{\nu}_\infty$	$\tilde{a}_2$	
`Sisko` (`sisko`)	$\tilde{m}$	$\tilde{n}$	$\tilde{\nu}_\infty$			
`Cross` (`cr`)	$\tilde{K}$	$\tilde{a}$	$\tilde{\nu}_0$	$\tilde{\nu}_\infty$		
`Inout` (`io`)	$\tilde{\nu}_{\text{in}}$	$\tilde{\nu}_{\text{out}}$				
`print vtk velocity`	`<filename>`	c_u				Output data in VTK-format, scaled with the provided conversion factor. For output in simulation units type `1.0`
`print vtk shearrate`	`<filename>`	$c_{\dot{\gamma}}$				
`print vtk viscosity`	`<filename>`	c_ν				
`print vtk relaxfreq`	`<filename>`	c_{ω_S}				
`print timestep_recommendation`	`<filename>`					Prints the maximum and minimum viscosity in the system and give an estimate on how large to choose the time step
`info`						Prints the commands and their usage in the terminal

10.2 Modified files

This is a list containing the hierarchy of the added and modified files of the ESPResSo software package:

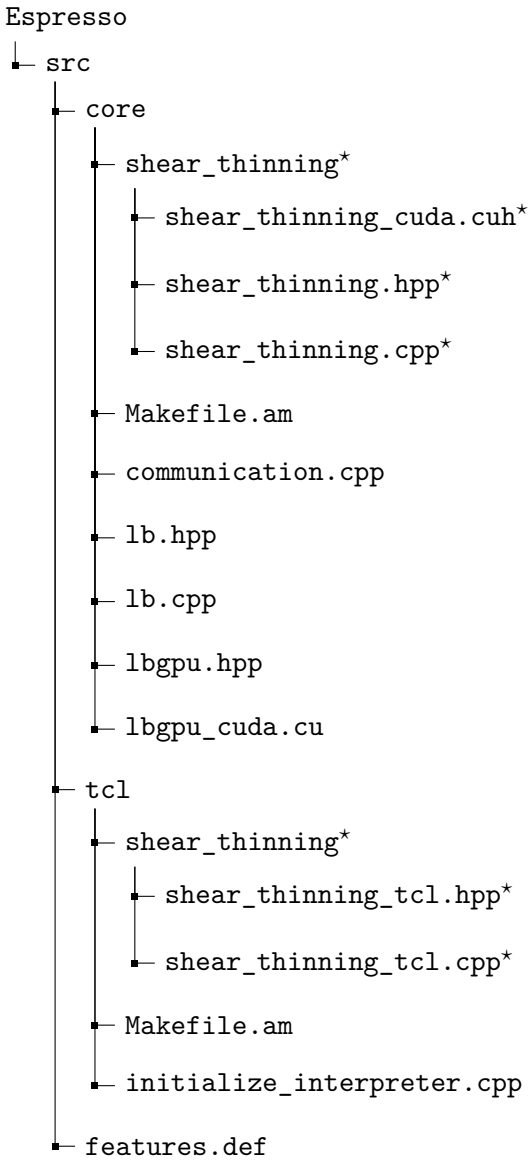

All changes apply only if `SHEAR_THINNING` is defined in `build/myconfig.hpp`.
The modifications to the main ESPResSo code are all embraced by the following keywords:

```
#ifdef SHEAR_THINNING
 /* code */
#endif
```

Part IV

Simulations

11 Overview

This part presents the results of the simulations that have been performed during the work on this thesis.
The first chapter contains a series of benchmarking simulations, providing a qualitative comparison between simulation data and analytical flow and shear rate profiles for simple geometries. Afterwards, the scaling of the relative error of the simulation method is investigated quantitatively.
The next chapter explains the analysis methods that are utilized to obtain a measure for the deformation of a cell. Two of the methods can be employed for arbitrarily shaped cells: The maximum elongation of a cell and its asphericity. The third method is only applicable to spherical cells with conserved volume.
Another important point to treat before the simulations is the non-dimensionalization, explaining how real physical quantities can be transferred to their dimensionless equivalents in the simulation. This includes the introduction of the two main dimensionless numbers used in this work, the Reynolds number Re and the Capillary number Ca. Furthermore, certain ways of fixing other parameters will be presented, e. g. the flow rate or the maximum velocity.
Afterwards, cells are included into a periodic cylindrical channel and their deformation is analyzed with respect to the shear thinning strength of the fluid. Simulations with a single cell provide knowledge about the general influence of the fluid itself and of the radial position of the cell. Adding more cells gives insight to the effects of cell-cell interactions on the deformation and provides statistical data.
The last part concentrates on the numerical realization of a 3D-printer nozzle using no-slip and free-slip boundary conditions. The flow behavior of a single cell and its deformation is investigated in the setup, especially at the transition between the two boundary types. An interesting aspect at this is the behavior of a cell for even stronger shear thinning fluids, as the flow profiles in the two regions get more and more similar and the transition decreases.

12 Benchmarking and error analysis

12.1 Simulation setup

For this chapter, a series of benchmarking simulations is performed to determine the accuracy of the implemented method. The setup as depicted in fig. 12.1 is applied: A channel constrained by two planes at $y = 0$ and $y = y_{\max}$ with periodic boundary conditions in x- and z-direction. All simulations are performed for a channel with fixed number of nodes $N_x = 10$ and $N_z = 10$ in x- and z-direction, respectively. The number of lateral nodes N_y is varied between 10 and 200. To obtain a velocity profile solely depending on y, the simulation output data is averaged over the remaining directions.

12.2 Benchmarking

At first, the actual simulation output shall be compared to the analytical solution qualitatively. For this purpose, fig. 12.2 and 12.3 plot the simulated velocity and shear rate profile with respect to the lateral channel position and the corresponding analytical solution. The number of lateral nodes is $N_y = 50$. Furthermore, the profiles are normalized using the maximum velocity at the channel center and the maximum shear rate at the channel wall, respectively. This is only for convenience, as the maximum velocities for $n = 1$ and $n = 0.4$ are ten orders of magnitude apart and the normalization makes it easier to look at all curves at once.
So far, there is no unit conversion employed to transfer the simulation units into actual physical quantities. However, these non-dimensional units are only used in this chapter as it is sufficient for the comparison of simulation and analytical solution.

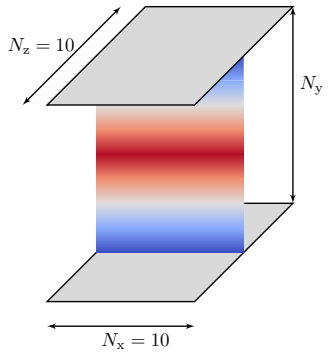

Figure 12.1: The simulation box setup for the benchmarking simulations. Two parallel (x, z)-planes with periodic boundary conditions and a flow in x-direction. The number of lateral nodes N_y is varied.

12.2.1 Power-law model

In fig. 12.2, the velocity and shear rate profile is plotted for power-law exponents ranging from $n = 0.4 - 1.0$. It can be seen that simulation and analytical solution agree very well. The (dimensionless) simulation input parameters and some important derived quantities are listed in the following table for the maximum and minimum power-law exponent:

n	0.4	1.0
m	10^4	
G	10^{-3}	
$u_{\max}$	6.1×10^{-14}	2.9×10^{-5}
Re	1.7×10^{-24}	7.2×10^{-6}

The Reynolds number Re will be defined in chap. 13 about non-dimensionalization. The huge difference at this point is due to the consideration of n in this definition. As $\mathrm{Re} \ll 1$, the flow can be considered laminar.

12.2.2 Truncated power-law model

The simulation and analytical solution also agree very well for the truncated power-law model, which is shown in fig. 12.3. In addition to the simple power-law model, the viscosity limits ν_0 and ν_∞ have to be defined. They are chosen in a way that the regions of Newtonian and power-law behavior are the same for all power-law exponents by simply inverting the analytical expression for the limits in the channel from eq. (6.35) and eq (6.45) and solving them for the viscosity limits. Therefore,

$$\nu_0 \varrho = m \left(-\frac{G}{2m} r_0 \right)^{1-\frac{1}{n}} \quad \text{and} \tag{12.1}$$

$$\nu_\infty \varrho = m \left(-\frac{G}{2m} r_\infty \right)^{1-\frac{1}{n}} \quad . \tag{12.2}$$

Similar to the power-law, the range of these parameters is very large for the different exponents, as shown in the following table:

n	0.4	1.0
m	10^4	
G	10^{-3}	
ν_0	3.0×10^{13}	10^4
ν_∞	3.8×10^{12}	10^4
$u_{\max}$	5.6×10^{-14}	2.9×10^{-5}
Re	1.7×10^{-24}	7.2×10^{-6}

For the Reynolds number the same definition is used as before.

Figure 12.2: Comparison of the simulated velocity and shear rate (squares) and the corresponding analytical profile (lines) in dependence of the power-law exponent for the simple power-law model. The black curve denotes the Newtonian case, which is similar to $n = 1.0$. A good agreement between simulation and analytical solution can be seen.

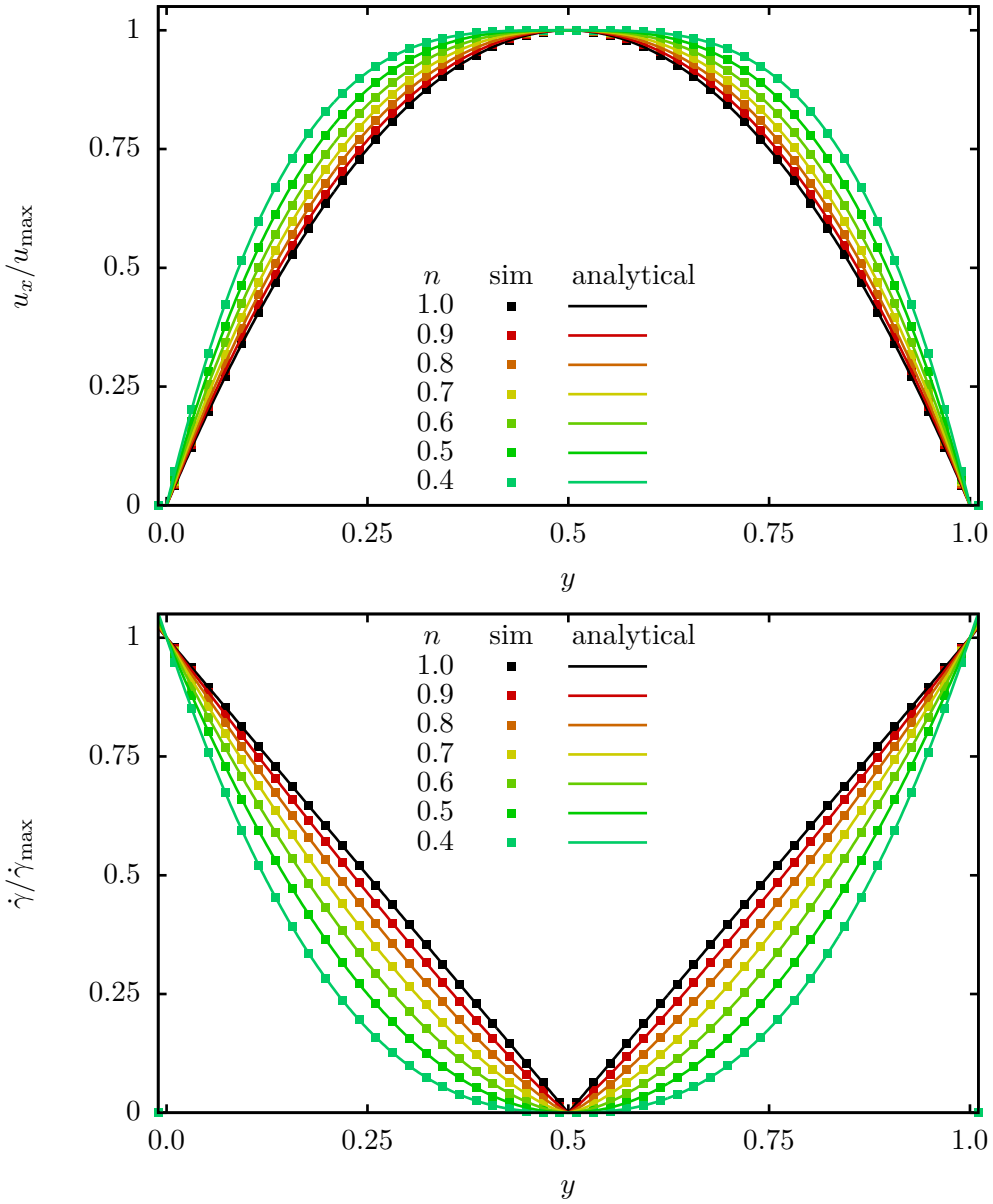

Figure 12.3: Comparison of the simulated velocity and shear rate (squares) and the corresponding analytical profile (lines) in dependence of the power-law exponent for the truncated power-law model. The black curve denotes the Newtonian case, which is similar to $n = 1.0$. The Newtonian and power-law regions are indicated by the gray vertical lines. The Newtonian regions can easily be seen in the shear rate plot, where they appear as straight lines. Simulation and analytical profiles agree very well.

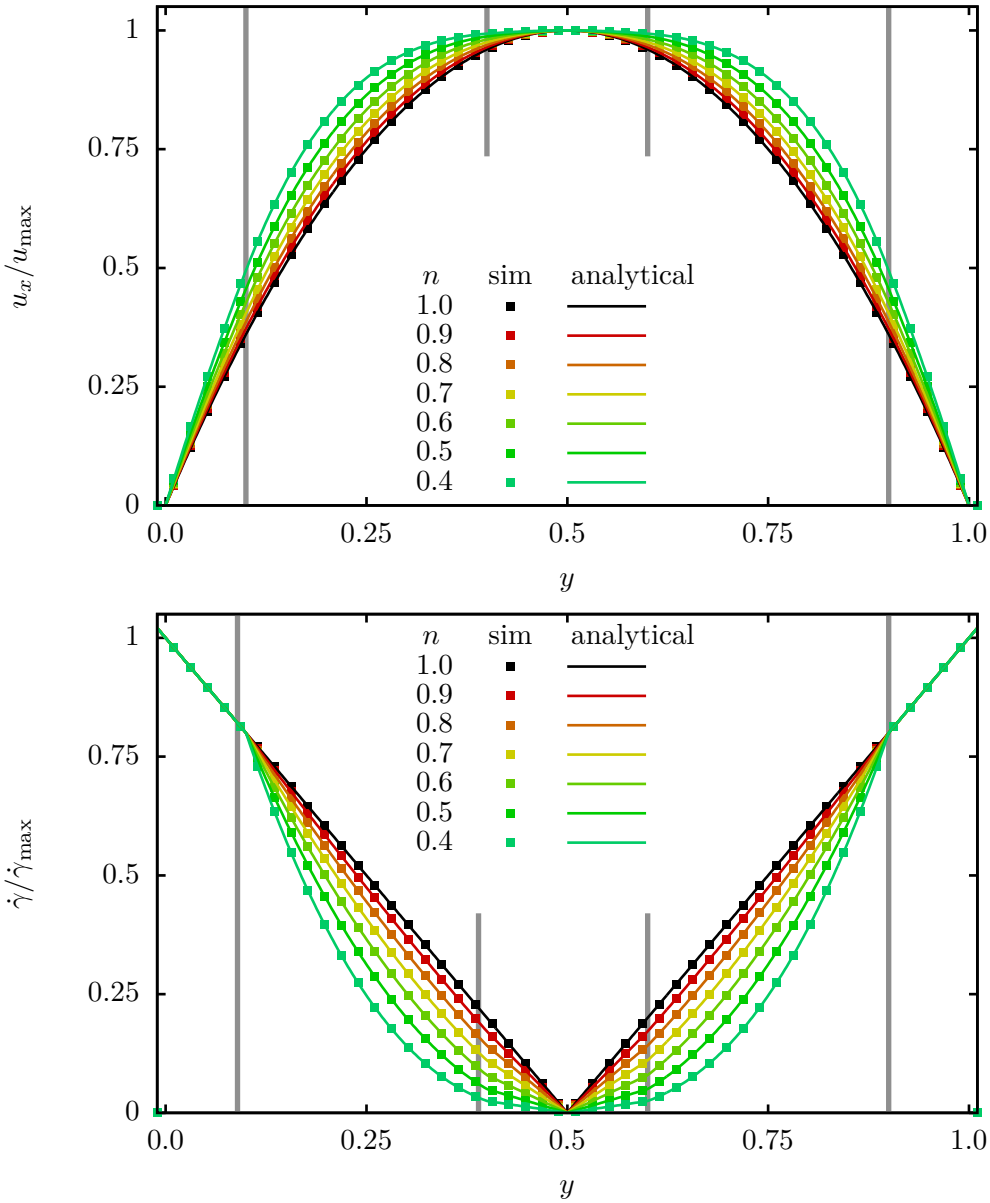

12.3 Error analysis

Now, a quantitative analysis of the error of the simulation method is utilized. Therefore, simulations are performed with varying number of lateral nodes. The accuracy of the unmodified LBM implementation is of second order [7], i. e. $\varepsilon \propto N_y^{-2}$. Several works determined the accuracy of 2D SRT Lattice Boltzmann simulations for power-law fluids in a similar setup as second order accurate [18, 45]. For a 2D MRT model, second order accuracy has been shown for a lid-driven cavity flow [34].
In the following, $\boldsymbol{u}_\mathrm{s}(y)$ denotes the averaged simulated velocity and $\boldsymbol{u}_\mathrm{a}(y)$ the analytical solution for the corresponding viscosity model. One of the assumptions in the derivation of the analytical profile is an uniaxial flow, thus, only the component in flow direction exists. This is not given for the simulation output and there are still non-zero components in the other directions, but those are usually at least two orders of magnitude smaller.
The relative error ε of a simulation is then calculated via the deviation of the simulation from the analytical solution, scaled with the maximum velocity:

$$\varepsilon = \sqrt{\sum_{y=0}^{N_y-1} \left\| \frac{\boldsymbol{u}_\mathrm{s}(y) - \boldsymbol{u}_\mathrm{a}(y)}{u_\mathrm{a}^\mathrm{max}} \right\|^2} \quad . \tag{12.3}$$

Written out, this equation gives the final form of the error calculation used in this chapter:

$$\varepsilon = \sqrt{\sum_{y=0}^{N_y-1} \frac{\left(u_\mathrm{s}^x(y) - u_\mathrm{a}(y)\right)^2 + \left(u_\mathrm{s}^y(y)\right)^2 + \left(u_\mathrm{s}^z(y)\right)^2}{\left(u_\mathrm{a}^\mathrm{max}\right)^2}} \tag{12.4}$$

12.3.1 Power-law model

Fig. 12.4 shows the scaling of the simple power-law model with the number of lateral nodes and a line indicating second order accuracy. It can be seen that the error fulfills the expectation and scales as $\varepsilon \propto N_y^{-2}$. The error is below 1 % for all power-law exponents for more than 20 nodes. In general, the error increases for lower power-law exponents, i. e. with higher shear thinning. The deviation for low n and N_y, here $N_y = 10, n = 0.4$, has also be observed in [18] for a 2D flow. For some reason which is yet to investigate, the error increases again if $N_y > 70$.

12.3.2 Truncated power-law model

The same analysis for the simulations with the truncated power-law model yield the plot in fig. 12.5. Also here, the error shows the second order scaling with the number of lateral nodes as well as an increasing error with decreasing power-law exponent. However, the error is less compared to the power-law model. This might be a consequence of the Newtonian regions that prevent the viscosity and therefore the shear relaxation frequency to assume very low or high values that might cause numerical issues. Similar to the power-law model, the error increases here for $N_y > 70$ as well.

Figure 12.4: The scaling of the relative error ε with the number of lateral nodes N_y is approximately of second order for the power-law model. The error increases with decreasing power-law exponent, i. e. higher shear thinning.

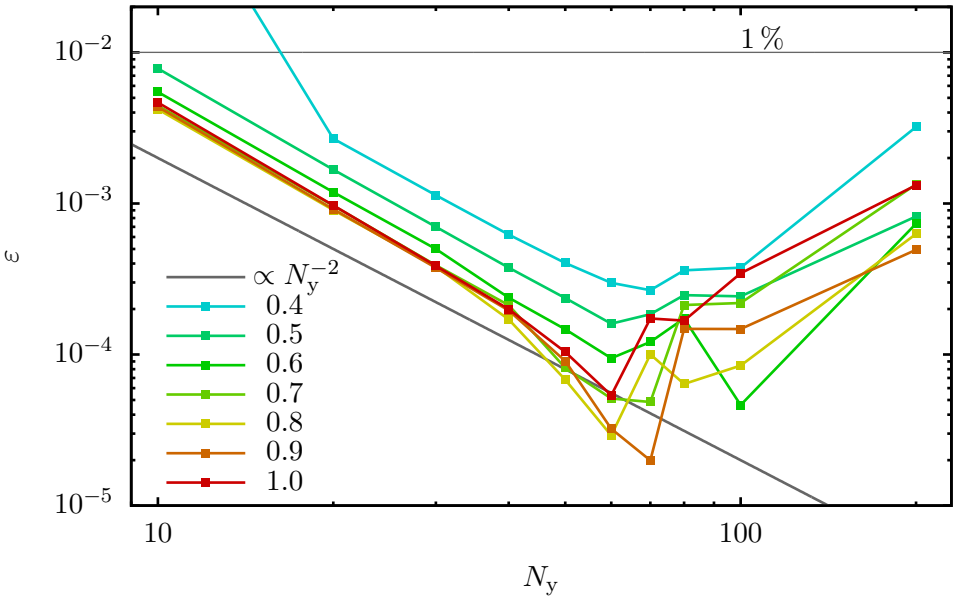

Figure 12.5: The scaling of the relative error ε with the number of lateral nodes N_y is also approximately of second order for the truncated power-law model. The error does not increase so strong with decreasing power-law exponent as in the simple power-law model. This might be a consequence of the Newtonian regions that prevent numerical stabilities.

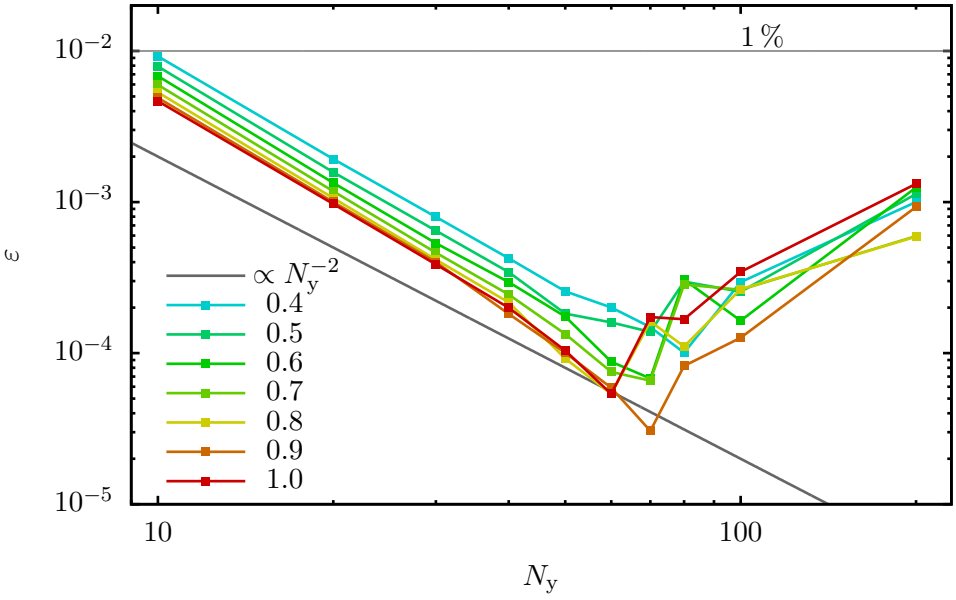

13 Non-dimensionalization

In this chapter, a brief introduction into the basic principles of non-dimensionalization is given based on [8] and [7]. The *law of similarity* will be employed to choose the simulation parameters in a way that they represent the dynamics of the real physical system. At first, the important dimensionless numbers for this thesis, i. e. the Reynolds number and the capillary number, will be defined considering a power-law viscosity model for the fluid. Afterwards, the choice of the simulation parameters will be explained in detail.

13.1 Notation

The following notation will be used for distinguishing between simulation units, physical units and their conversion factors. Assume a physical quantity q, then

- q denotes the physical quantity in SI-units,
- $\tilde{q}$ denotes the dimensionless simulation quantity and
- c_q denotes the conversion factor including the unit.

The conversion is given by the equation

$$q = \tilde{q}\, c_q \quad . \tag{13.1}$$

13.2 Dimensionless numbers

In general, a physical system can be non-dimensionalized by fixing a certain number of independent scales in the system. For a hydrodynamic system, it is common to scale with respect to the fluid density $\hat{\rho}$, a length $\hat{L}$, typically the width of a channel or a cell diameter, and a viscosity $\hat{\nu}$. Another possibility is to fix the velocity scale instead of the viscosity. Either way, three independent scales are fixed and the conversion factors for other quantities can be derives, e. g. the time scale can be derived from length and velocity as

$$\tilde{t} = t \left(\frac{\hat{L}}{\hat{u}} \right)^{-1} \quad . \tag{13.2}$$

As non-Newtonian fluids are topic of this work, the following derivations of the Reynolds and capillary number assume the kinematic viscosity according to the power-law model,

i. e.

$$\nu = m\,\dot{\gamma}^{n-1} \quad . \tag{13.3}$$

In this work, the Navier-Stokes equations are non-dimensionalized fixing the three scales for

- the fluid mass density ϱ in $\frac{\mathrm{kg}}{\mathrm{m}^3}$,
- the typical system length $\hat{L}$ in m and
- the (kinematic) power-law consistency index m in $\frac{\mathrm{m}^2}{\mathrm{s}^{2-\mathrm{n}}}$, which is depending on the power-law exponent n.

13.2.1 Reynolds number

Reynolds number is given as the ratio of inertial to viscous forces in a fluid. Generally, a low Reynolds number implies a more laminar flow while a high Reynolds number describes rather turbulent dynamics. This thesis will only consider the first case, i. e. $\mathrm{Re} \ll 1$. Starting point of the derivation is the Navier-Stokes equation

$$\frac{\partial \boldsymbol{u}}{\partial t} + (u \cdot \boldsymbol{\nabla})\, u = -\frac{1}{\varrho}\boldsymbol{\nabla} p + \boldsymbol{\nabla} \cdot \left[m\,\dot{\gamma}^{n-1}\ (\boldsymbol{\nabla}\boldsymbol{u} + (\boldsymbol{\nabla}\boldsymbol{u})^{\intercal}) \right] + \frac{1}{\varrho}\mathfrak{f} \tag{13.4}$$

Dimensionless expressions for the remaining parameters according to the fixed scales are found through combination:

$$\tilde{\boldsymbol{u}} = \boldsymbol{u}\left(m\hat{L}^{-n}\right)^{-\frac{1}{2-n}} = \frac{\boldsymbol{u}}{c_{\boldsymbol{u}}} \qquad [c_{\boldsymbol{u}}] = \frac{\mathrm{m}}{\mathrm{s}} \tag{13.5}$$

$$\tilde{\dot{\gamma}} = \dot{\gamma}\left(\frac{c_{\boldsymbol{u}}}{\hat{L}}\right)^{-1} = \frac{\dot{\gamma}}{c_{\dot{\gamma}}} \qquad [c_{\dot{\gamma}}] = \frac{1}{\mathrm{s}} \tag{13.6}$$

$$\tilde{\mathfrak{f}} = \mathfrak{f}\left(\frac{\varrho c_{\boldsymbol{u}}^2}{\hat{L}}\right)^{-1} = \frac{\mathfrak{f}}{c_{\mathfrak{f}}} \qquad [c_{\mathfrak{f}}] = \frac{\mathrm{kg}}{\mathrm{m}^2\,\mathrm{s}^2} \tag{13.7}$$

$$\tilde{p} = p\left(\varrho c_{\boldsymbol{u}}^2\right)^{-1} = \frac{p}{c_p} \qquad [c_p] = \frac{\mathrm{kg}}{\mathrm{m}\,\mathrm{s}^2} \tag{13.8}$$

Furthermore, the derivatives are non-dimensionalized according to

$$\frac{\partial}{\partial \tilde{t}} = \left(\frac{\hat{L}}{c_{\boldsymbol{u}}}\right)\frac{\partial}{\partial t} \quad \text{and} \tag{13.9}$$

$$\tilde{\boldsymbol{\nabla}} = \hat{L}\boldsymbol{\nabla} \quad . \tag{13.10}$$

Inserting the above into the NSE yields

$$\frac{\partial}{\partial \tilde{t}}\tilde{\boldsymbol{u}} + \left(\tilde{\boldsymbol{u}} \cdot \tilde{\boldsymbol{\nabla}}\right)\tilde{\boldsymbol{u}} = -\tilde{\boldsymbol{\nabla}}\tilde{p} + \underbrace{\frac{m c_{\boldsymbol{u}}^{n-2}}{\hat{L}^n}}_{=\frac{1}{\mathrm{Re}}} \tilde{\boldsymbol{\nabla}} \cdot \left[\tilde{\dot{\gamma}}^{n-1}\left(\tilde{\boldsymbol{\nabla}}\tilde{\boldsymbol{u}} + \left(\tilde{\boldsymbol{\nabla}}\tilde{\boldsymbol{u}}^{\mathsf{T}}\right)\right)\right] + \tilde{\mathfrak{f}} \quad , \tag{13.11}$$

and the Reynolds number can be obtained as

$$\mathrm{Re} := \frac{c_{\boldsymbol{u}}^{2-n}\hat{L}^n}{m} \quad . \tag{13.12}$$

This form is also used for power-law fluids in the literature, e. g. in [46].
The usual expression for the Reynolds number in a Newtonian fluid follows by setting the power-law exponent to $n = 1$, which sets the consistency parameter m equal to the kinematic viscosity ν, hence

$$\mathrm{Re}_{\mathrm{Newtonian}} = \frac{c_{\boldsymbol{u}}\hat{L}}{\nu} \quad . \tag{13.13}$$

Alternatively, the Reynolds number for the power-law model can be directly obtained from the expression for the Newtonian fluid by replacing the kinematic viscosity with $\nu = m c_{\dot{\gamma}}^{n-1}$:

$$\begin{aligned} \mathrm{Re} &= \frac{c_{\boldsymbol{u}}\hat{L}}{\nu} = \frac{c_{\boldsymbol{u}}\hat{L}}{m c_{\dot{\gamma}}^{n-1}} \\ &= \frac{c_{\boldsymbol{u}}\hat{L}}{m}\left(\frac{\hat{L}}{c_{\boldsymbol{u}}}\right)^{n-1} = \frac{c_{\boldsymbol{u}}^{2-n}\hat{L}^n}{m} \end{aligned} \tag{13.14}$$

13.2.2 Capillary number

The second important dimensionless number in this thesis is the so called *capillary number*, denoted by Ca, which is defined as the ratio of fluid forces and elastic forces of a cell. A detailed derivation of the formula below can be found in [47]. For this thesis, an approach similar to the alternative way to construct the power-law Reynolds number is chosen.
The Capillary number is given as [36]

$$\mathrm{Ca} = \frac{\nu \varrho c_{\boldsymbol{u}}}{\kappa_{\mathrm{S}}} \quad , \tag{13.15}$$

where κ_{S} denotes one of the elastic moduli in the cell model. Here, it is chosen as the elastic shear modulus κ_1 from the Skalak model explained in 8.8. If the kinematic viscosity is then, like above, expressed as $\nu = m c_{\dot{\gamma}}^{n-1}$, an expression for the capillary number for cells in a power-law fluid is obtained:

$$\mathrm{Ca} := \frac{\varrho m c_{\boldsymbol{u}}^{n}}{\kappa_1 \hat{L}^{n-1}} \tag{13.16}$$

This form is also used in [48].

13.3 Fixed scales in the simulation

Given the theory of non-dimensionalization, the following sections provide the numbers that are used in the actual simulation. Most parameters are chosen in the very same way in all simulation as it makes for better comparability.

13.3.1 Length

The simulated cell are spheres with radius R that consist of 1280 surface triangles. The radius in physical units is chosen to be approximately the long radius of a red blood cell. By choosing the radius of the cell in lattice distances, the conversion factor c_L for the length of a grid cell is determined.

$$r_{\text{cell}} = 4.0 \times 10^{-6}\,\text{m} \tag{13.17}$$

$$\tilde{r}_{\text{cell}} = 7 \tag{13.18}$$

$$c_L = 5.714 \times 10^{-7}\,\text{m} \tag{13.19}$$

Therefore, the physical length of a grid cell is $\Delta x = 5.714 \times 10^{-7}\,\text{m}$. The radius also serves as the typical length $\hat{L}$ in the system for the calculation of Re and Ca.

13.3.2 Density

The mass density of the fluid is chosen to be that of water, or roughly that of blood plasma, which would serve as a typical fluid that encounters with cells.

$$\rho = 1.0 \times 10^3\,\frac{\text{kg}}{\text{m}^3} \tag{13.20}$$

$$\tilde{\rho} = 1 \tag{13.21}$$

$$c_\rho = 1.0 \times 10^3\,\frac{\text{kg}}{\text{m}^3} \tag{13.22}$$

13.3.3 Power-law consistency parameter

The last fixed parameter is the consistency index, which is chosen to be 1 in simulation units:

$$\tilde{m} = 1 \tag{13.23}$$

$$\tag{13.24}$$

To be more consistent with the idea of simulating bioinks, m is chosen in a way that the viscosity is never less than that of blood plasma ($1.2 \times 10^{-3}\,\text{Pa}\,\text{s}$) in a cylindrical channel. As long as the analytical solution of the flow is valid and not disturbed too much by the

presence of cells, the following approaches are used to determine m for a system with fixed maximum velocity $u_{\max}$ or fixed flow rate Ω, respectively.

13.3.3.1 Fixed maximum velocity

At first, the analytical profile for the viscosity in a channel is constructed by inserting the solution of the shear rate profile (cf. eq. 6.19) into the power-law model equation, which yields

$$\nu(r) = m\,[\dot{\gamma}(r)]^{n-1} = m\left[\frac{u_{\max}\left(1+\frac{1}{n}\right)}{r}\right]^{n-1} \quad . \tag{13.25}$$

The minimum viscosity ν_0 for a shear thinning fluid is at the channel wall, i. e. $r = R$, hence

$$\nu_0 = m\left[\frac{u_{\max}\left(1+\frac{1}{n}\right)}{R}\right]^{n-1} \quad . \tag{13.26}$$

This equation is solved for m to obtain the consistency index as

$$m(n) = \nu_0\left[\frac{u_{\max}\left(1+\frac{1}{n}\right)}{R}\right]^{\frac{1}{n-1}} \quad . \tag{13.27}$$

13.3.3.2 Fixed inflow rate

As the maximum velocity obviously depends on the power-law exponent n the above approach is only valid if the maximum velocity is fixed and the remaining parameters are derived from it.
Another possibility is to fix the rate of inflow Ω at the channel entrance. It is defined as

$$\Omega = \pi R^2 u_{\text{avg}} = \pi R^2 u_{\max}\left(1+\frac{2}{3+\frac{1}{n}}\right) \quad , \tag{13.28}$$

using the expression for u_{avg} derived in eq. (6.22). Thus, the consistency parameter is computed as

$$m(n) = \nu_0\left[\frac{u_{\max}\left(1+\frac{1}{n}\right)}{\frac{2R}{3+\frac{1}{n}}}\right]^{\frac{1}{n-1}} \quad . \tag{13.29}$$

13.3.3.3 Fixed pressure gradient

If instead the pressure gradient G is fixed, the consistency parameter is calulated via:

$$m\left(n\right) = \left[\nu_0 \left(-\frac{GR}{2}\right)^{\frac{1}{n}}\right]^{\frac{1}{1-\frac{1}{n}}} \tag{13.30}$$

13.4 Fixed cell parameters

The parameters of the cell are fixed in all simulations, as only the influence of the shear thinning effects in the fluid is to be investigated. To be able to compare the cell behavior with other work from our research group, the properties are chosen to be those of red blood cells.
The elastic moduli of the Skalak law are chosen as follows:[49]

$$\kappa_1 = 5.0 \times 10^{-6} \frac{\mathrm{N}}{\mathrm{m}} \tag{13.31}$$

$$\kappa_2 = 5.0 \times 10^{-4} \frac{\mathrm{N}}{\mathrm{m}} = 100\kappa_1 \tag{13.32}$$

$$\kappa_\mathrm{B} = 3.0 \times 10^{-19} \,\mathrm{N\,m} \tag{13.33}$$

$$\kappa_\mathrm{V} = 5.0 \times 10^{-4} \frac{\mathrm{N}}{\mathrm{m}} \tag{13.34}$$

13.5 Time step adjustment

The given maximum or average flow velocity also determines the analytical viscosity profile in the channel, which is used to tune the time step. If the time step is too large, the simulated data can have an offset or the simulation can get unstable.
Simulations with pure fluid have shown that it is sufficient to choose the minimal viscosity as a reference for the time step.
The time step is then calculated, with $\tau = 1$, as [36]

$$\Delta t = \frac{\Delta x^2}{6\tilde{\nu}_\mathrm{min}} = (\tau - \tfrac{1}{2})\frac{\Delta x^2}{3\tilde{\nu}_\mathrm{min}} \quad . \tag{13.35}$$

14 Analysis methods for cell deformation

This chapter gives an overview of the different methods that are used to get a measure for the deformation of a cell.

14.1 Maximum elongation

This method finds the maximum distance between two nodes of the cell. With N being the total number of nodes on the cell surface, i and j numbering the nodes and $\boldsymbol{r}_k$ denoting the vector pointing to the k-th node, the mathematical formulation of this analysis method is

$$d_{\max} := \max_{i,j} \{\|\boldsymbol{r}_j - \boldsymbol{r}_j\| \mid 0 \leq i, j < N\} \quad . \tag{14.1}$$

The implemented algorithm simply loops over the surface N times, calculating the distance between the i-th and j-th surface point and storing the maximum distance found. Obviously, the maximum elongation has the unit of a length, but it can be nondimensionalized, e. g. by using the diameter of a reference sphere.

14.2 Deviation from reference sphere

This method results in similar output as the calculation of the asphericity, given that the reference shape is a sphere and volume is conserved.
Let R_{ref} be the radius of the reference sphere, e. g. the initial shape, N the number of surface nodes and $\boldsymbol{r}_k$ a vector pointing from the center of mass (COM) towards the k-th node. The deviation from the sphere Γ is then defined by the averaged difference between the radial position of a node and the reference sphere radius

$$\Gamma := \frac{1}{N} \sum_{i=0}^{N-1} |\|\boldsymbol{r}_i\| - R_{\text{ref}}| \quad . \tag{14.2}$$

The absolute is taken to ensure that elongation and contraction in different regions do not cancel each other.

Figure 14.1: Depiction of the maximum elongation of a cell (left) and the average deviation from a sphere (right).

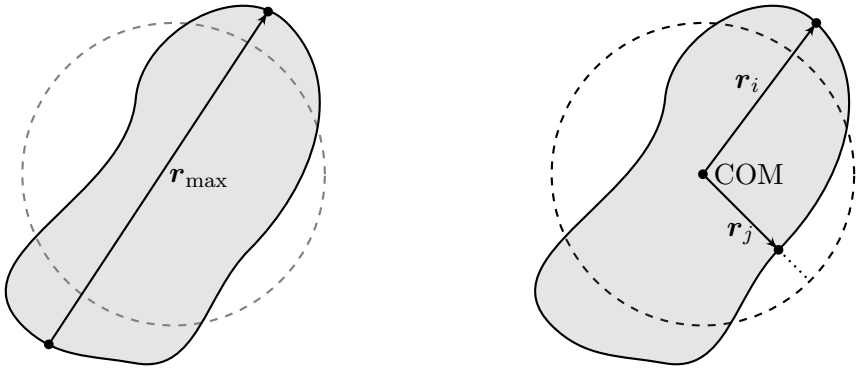

14.3 Asphericity

The asphericity characterizes the deviation from a spherical shape without the necessity of a given spherical reference shape. It is defined as [50]

$$\alpha := \frac{1}{2R_G^4}\left[(\lambda_1-\lambda_2)^2+(\lambda_2-\lambda_3)^2+(\lambda_3-\lambda_1)^2\right] \quad , \tag{14.3}$$

where $\lambda_1 \leq \lambda_2 \leq \lambda_3$ are the eigenvalues of the gyration tensor $\underline{\mathrm{G}}$ and

$$R_G^2 = \lambda_1+\lambda_2+\lambda_3 \tag{14.4}$$

is the sum of its eigenvalues.
The gyration tensor is given by the second moments of position of the surface nodes:

$$\underline{\mathrm{G}} := \frac{1}{N}\sum_{i=0}^{N-1} \boldsymbol{r}_i\boldsymbol{r}_i \tag{14.5}$$

Like above, the number of nodes is given by N and $\boldsymbol{r}_k$ denotes the position vector of the k-th surface point. For a sphere, all eigenvalues are equal and the asphericity vanishes.

15 Simulations of cells in a cylindrical channel

In this chapter, the deformation of cells in a power-law fluid with respect to the strength of the shear thinning will be investigated in a cylindrical channel. Before the bioink reaches the printer nozzle, fluid and cells need to stream a much longer way through supply channels. Therefore, the corresponding simulations model an infinitely long cylindrical pipe.
After an introduction to the simulation setup, the first section focuses on the behavior of a single cell and provides reference values for the deformation with respect to the power-law exponent. Afterwards, simulations with four and nine cells are performed to investigate additional effects that originate in cell-cell interaction.

15.1 Simulation setup

The channel is a cylinder of 41.14 µm length with a radius of 13.14 µm. The total width and height of the simulation channel are 27.43 µm each. The radius of the inserted cells is 4 µm, according to chap. 13.
As periodic boundary conditions are used in x-direction, the pressure gradient G is chosen to match an inflow rate with average velocity $u_{\text{avg}} = 0.5\,\frac{\text{mm}}{\text{s}}$ for the single cell simulations and $u_{\text{avg}} = 2.5\,\frac{\text{mm}}{\text{s}}$ for the simulations with multiple cells. As the flow rate determines the speed of the bioprinting process, the latter value seems more realistic.

15.2 Single spherical cell

15.2.1 Centered in channel

At first, simulations are performed with a single cell that is centered in y- and z-direction. Due to the axial symmetry, the radial position of the cell does not change during the

Table 15.1: Reynolds number and capillary number in the simulations with a single cell in the cylindrical channel. The capillary number for $n = 0.4$ is nearly twice as large as in the Newtonian case.

n	1.0	0.9	0.8	0.7	0.6	0.5	0.4
Re	0.011	0.010	0.009	0.008	0.007	0.006	0.005
Ca	0.24	0.26	0.28	0.31	0.36	0.42	0.51

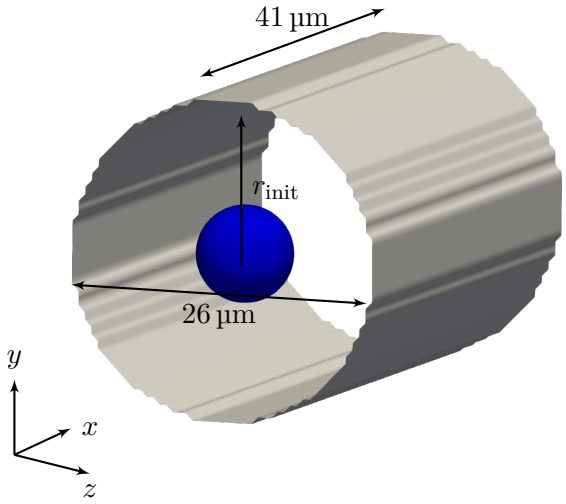

Figure 15.1: Simulation setup for a single cell in a cylindrical channel. The initial offset in y-direction is given by r_{init}. The cylinder length and radius measured in grid cells are 72 and 23, respectively.

simulation.
The plots in fig. A.1 depict the temporal evolution of the three measures for deformation, i. e. the maximum elongation $d_{\max}$, the deviation from a sphere Γ and the asphericity α. The red colors corresponds to a centered initial position, darker colors indicate a more shear thinning fluid, i. e. lower n. It can be seen that the deformation increases strongly in the beginning of the simulation, but reaches a rather stable value after a certain amount of simulation steps. For Γ and α, a trend regarding the power-law exponent is visible: Starting from the Newtonian case ($n = 1.0$), the deformations increase with stronger shear thinning, but decrease again for lower n. This means that a fluid that exhibits more of a plug flow deforms the cell greater than a Poiseuille-flow. What seems counterintuitive at first glance is easily explained if one considers the Capillary number in the different cases, listed in tab. 15.1. For decreasing n, Ca increases up to twice the value in the Newtonian case, which means that the viscous fluid forces are twice as strong as the elastic restoring forces trying to remain the cell shape. As long as the velocity gradients in the region $r \in [-r_{\text{cell}}, r_{\text{cell}}]$ are significant, the cell deformation is higher than in the Newtonian case. For $n = 0.4$, the plug flow region is wide enough to fit in a cell, resulting in a lower deformation.
The average deformation of the cell in the stationary flow with respect to n is shown in fig. 15.2 and also listed in tab. 15.2. The trend mentioned above is clearly visible. It is worth noting that the values of the asphericity α are very small for symmetrical deformations. Even for deformations that visibly differ from a spherical shape, it is in the order of 10^{-6}. To quantify the symmetrical deformations, Γ seems a better choice. However, the difference between the maximum and minimum deformation is roughly just 5 %. Nevertheless, the maximum elongation of a cell decreases with the shear thinning and the time series shows a clear trend that the stationary shape of this deformation is not fully reached during the simulation.
That the actual dependency on the power-law exponent is not so strong in the end can also be seen in fig. 15.3, where the shape of the cell is shown for different n. There is no significant difference visible in the stationary shape.

Figure 15.2: Average deformations of a single cell in channel center with respect to the power-law exponent. The error bars indicate the standard deviation. The data is obtained by processing the deformation data in fig. A.1 over the second half of the simulation. This is done to discard the effects of the equilibration, which takes quite long for the lowest power-law exponent. The data is also listed in tab. 15.2.

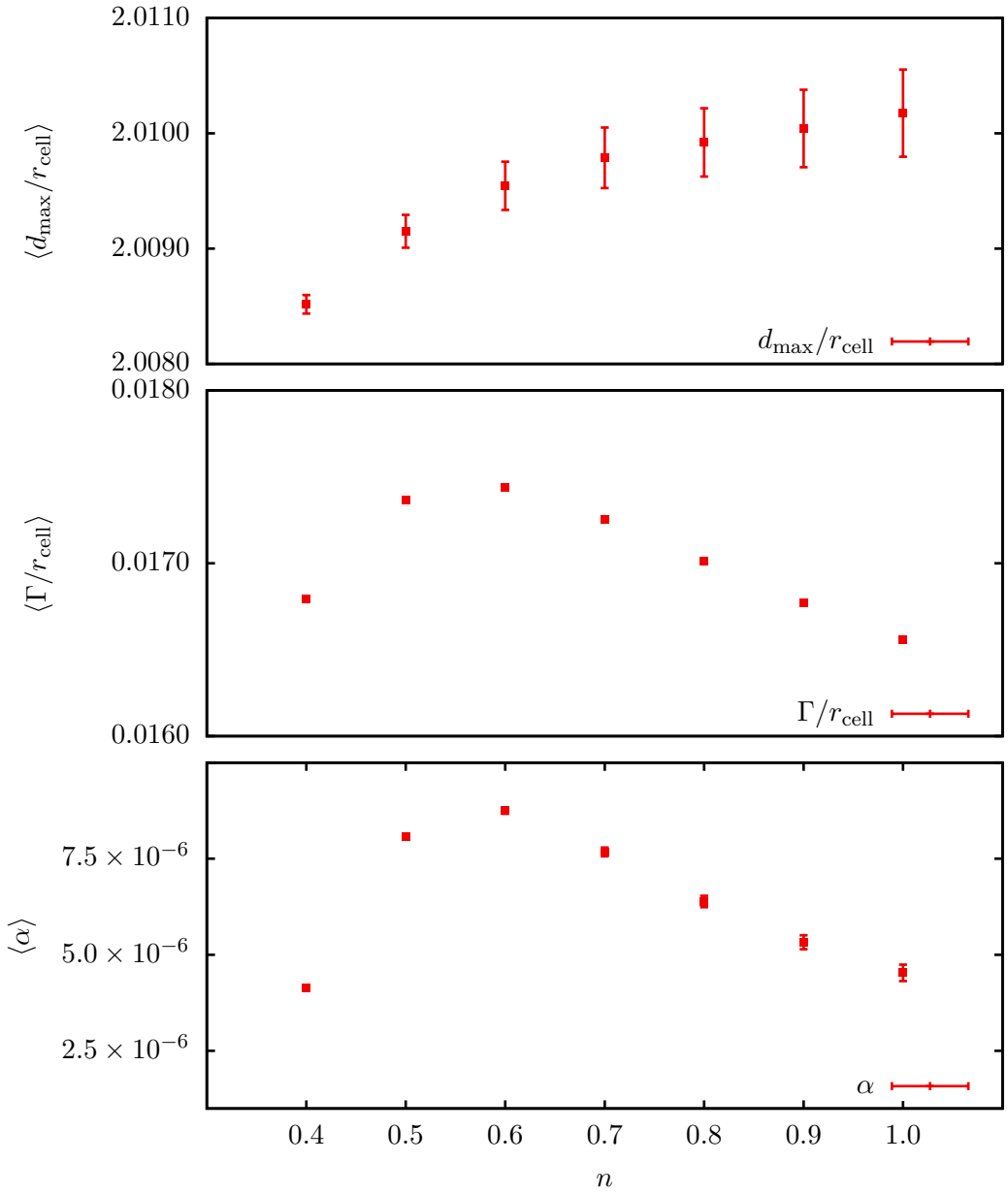

Figure 15.3: Depiction of the stationary cell shape at channel center for different shear thinning strength - a darker blue indicates a lower power-law exponent. A significant difference is barely visible.

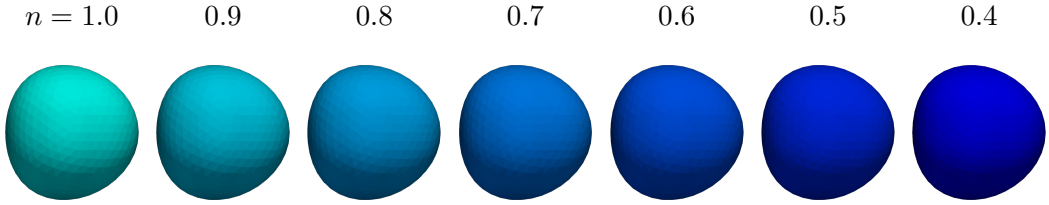

Table 15.2: Average deformation data of a single cell in channel center as depicted in fig. 15.2. σ_q denotes the respective standard deviation.

n	$\alpha \pm \sigma_\alpha$	$\frac{1}{r_{\text{cell}}}(\Gamma \pm \sigma_\Gamma)$	$\frac{1}{r_{\text{cell}}}(d_{\max} \pm \sigma_d)$
1.0	$(4.5 \pm 0.2) \times 10^{-6}$	$0.016\,56 \pm 0.000\,01$	2.0102 ± 0.0004
0.9	$(5.3 \pm 0.2) \times 10^{-6}$	$0.016\,773 \pm 0.000\,004$	2.0100 ± 0.0003
0.8	$(6.4 \pm 0.2) \times 10^{-6}$	$0.017\,010 \pm 0.000\,001$	2.0099 ± 0.0003
0.7	$(7.7 \pm 0.1) \times 10^{-6}$	$0.017\,256 \pm 0.000\,002$	2.0098 ± 0.0003
0.6	$(8.75 \pm 0.08) \times 10^{-6}$	$0.017\,439 \pm 0.000\,002$	2.0095 ± 0.0002
0.5	$(8.08 \pm 0.04) \times 10^{-6}$	$0.017\,366 \pm 0.000\,001$	2.0092 ± 0.0001
0.4	$(4.14 \pm 0.04) \times 10^{-6}$	$0.016\,793 \pm 0.000\,001$	2.0085 ± 0.0001

15.2.2 Near channel wall

Due to the velocity gradients, soft particles tend to marginate in a channel towards the center, where the maximum velocity and the lowest shear rates are present. In the following simulation, the same setup as before is used, but the cell is initialized very close to the channel boundary.
The margination of the cell is depicted in the figures 15.4 and 15.5 for the Newtonian case and $n = 0.4$. Additionally, the left-hand side shows the magnitude of the velocity field and the right-hand side the shear rate. The differences in the latter are clear: Near the wall, the cell is exposed to significantly higher shear rates, while the shear rate is very low in the central region. Looking at the cell shapes, there is again no great difference visible considering n. The cell shape is much more determined by its radial position in the channel.
This behavior is also clearly visible in the time series in fig. A.2. The data for all deformation measures show the same characteristics, and, again, a consistently higher deformation for lower power-law exponents.
If the simulations were run for a much longer time, the full margination could be visible, with the deformations reaching their stationary value.

Figure 15.4: Depiction of the different cell shapes during the margination of the cell towards the channel center in a Newtonian fluid. The velocity profile is indicated at the left, the shear rate at the right. In the Newtonian case, shear rates are significantly smaller at the channel wall, which explains the cell's quantitatively smaller deformation

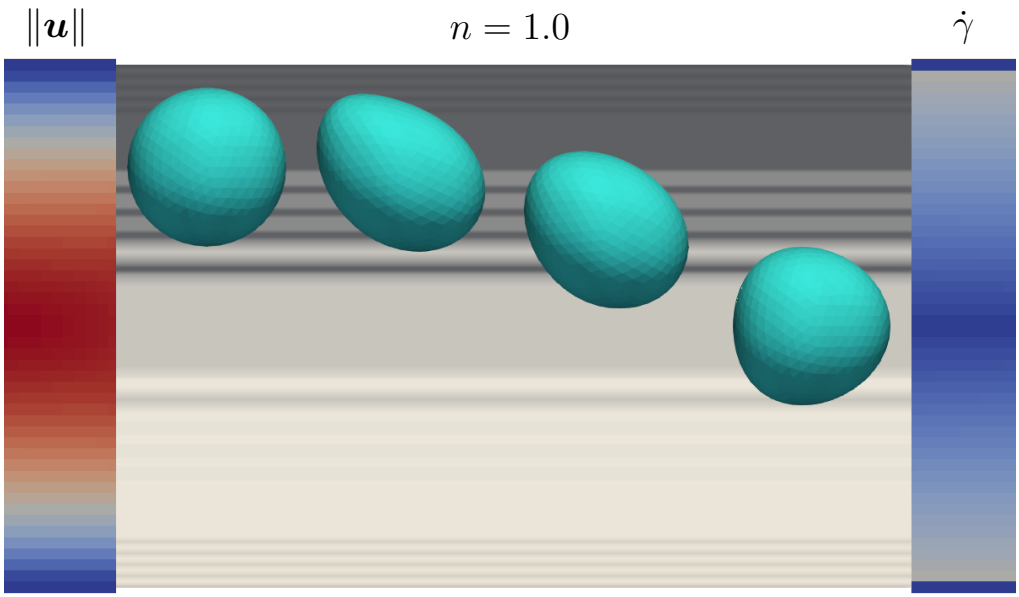

Figure 15.5: Depiction of the different cell shapes during the margination of the cell towards the channel center in a power-law fluid with $n = 0.4$.

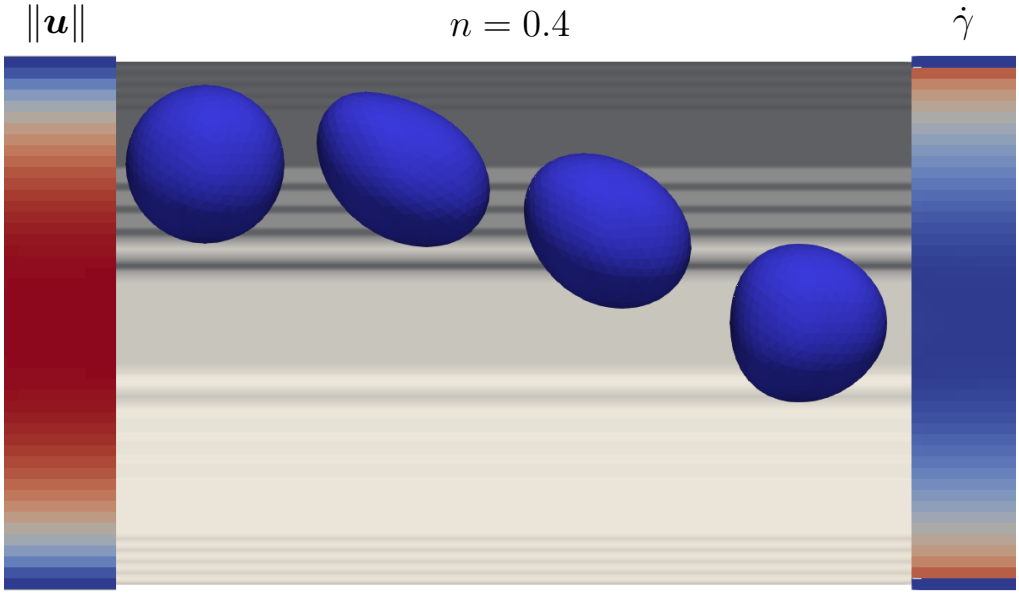

Table 15.3: Reynolds number and capillary number in the simulations with four and nine cells in the cylindrical channel. The capillary number for $n = 0.4$ is nearly twice as large as in the Newtonian case.

n	1.0	0.9	0.8	0.7	0.6	0.5	0.4
Re	0.055	0.051	0.047	0.042	0.037	0.032	0.026
Ca	1.2	1.3	1.4	1.6	1.8	2.1	2.5

15.3 Multiple spherical cells

Now, that the influences of the capillary number and radial position on the deformation are identified for a single cell in the channel, one can add more cells to investigate their behavior. In the following, the results of simulation series with four and nine cells in the channel are presented.
The cells are initialized at positions along a helix in the channel. The radial offset in the beginning is 6.4 µm in the simulations with nine cells and 5.2 µm with four cells, respectively. In x-direction, an equal distance of all cells is chosen.

15.3.1 Four cells

The figures A.3 and A.4 show the deformation averaged over all four cells during the simulation for two different initial distributions. It is clearly visible that the different measures for the deformation show the same characteristics: As in the simulation with a single cell, stronger shear thinning results in a higher deformation. In fig. A.4, some of the simulations show a margination of the four cells towards the channel center and therefore a decreasing deformation compared to the cells that stay farther outside. This is also depicted in fig. 15.6, showing the initial and final position of the cells.

15.3.2 Nine cells

The same procedure is applied in the simulations with nine cells. The figures A.5, A.6 and A.7 show the deformation during the simulation, again, consistently showing a significantly higher deformation for lower power-law exponents. Compared to the first two, the deformation data of the last series is less noisy and rather constant during the first half of the simulation. This can again be explained by looking at the initial position. As depicted in fig. 15.7, the cells are initialized directly behind each other and they maintain this configuration during the whole simulation. Compared to the other series, the cells do not marginate significantly during the simulation. The difference in deformation from the Newtonian case to $n = 0.4$ can be be seen by comparing the elongation of the cyan-colored ($n = 1.0$) and blue-colored ($n = 0.4$) cells.

Figure 15.6: Initial position of 4 cells in the channel shown from the side (top) and in flow direction (middle). The images at the bottom show a state during the simulation. Pictures are taken from two different simulation series with $n = 0.7$. The red cells show a margination into the channel center while the green cells stay further away.

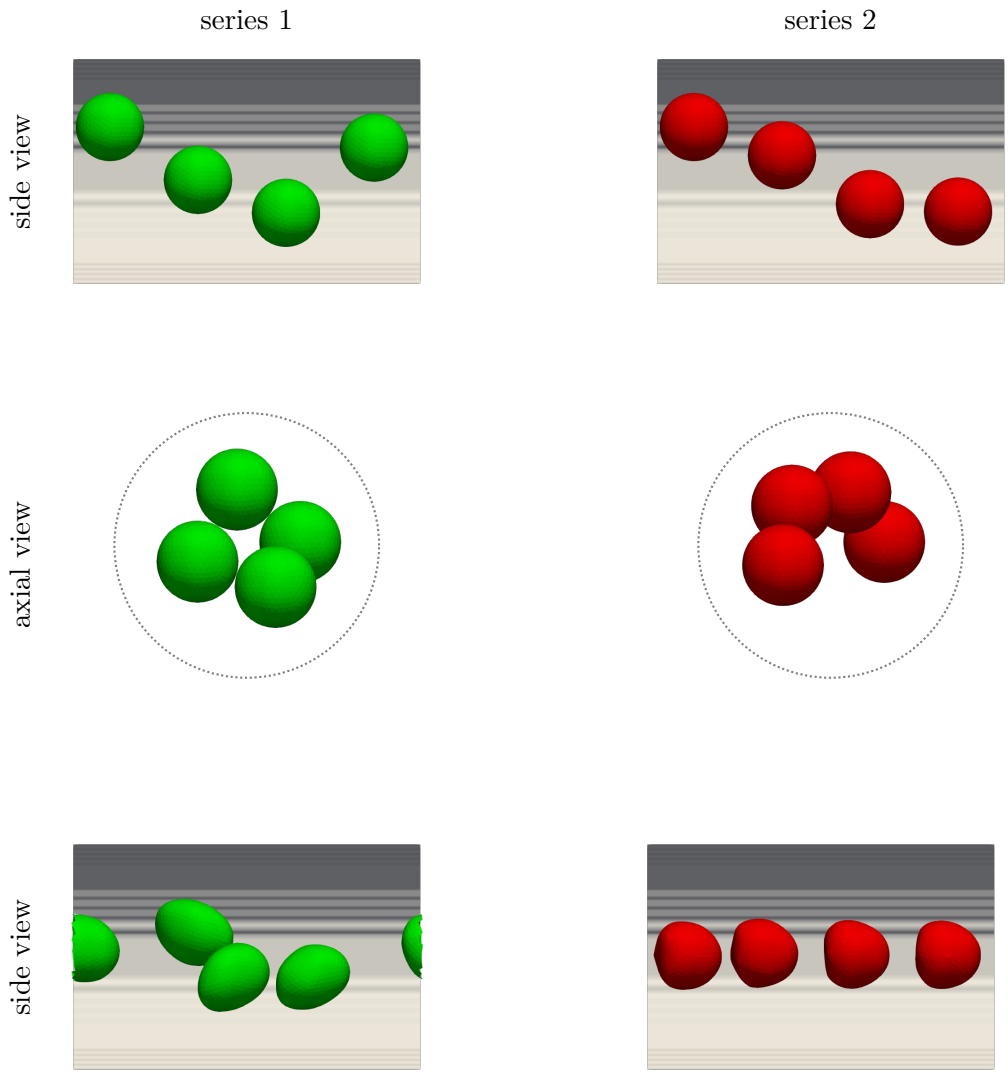

Figure 15.7: Initial position of the three simulation series performed with nine cells viewed from the side (top) and in flow direction (middle). The bottom images show a snapshot of the cells in Newtonian fluid (cyan) and power-law fluid with $n = 0.4$ (blue) in the same box for comparison. It can be seen that only little margination is happening. The images on the right show that the regular pattern of the initialization stays stable during the simulation in both cases.

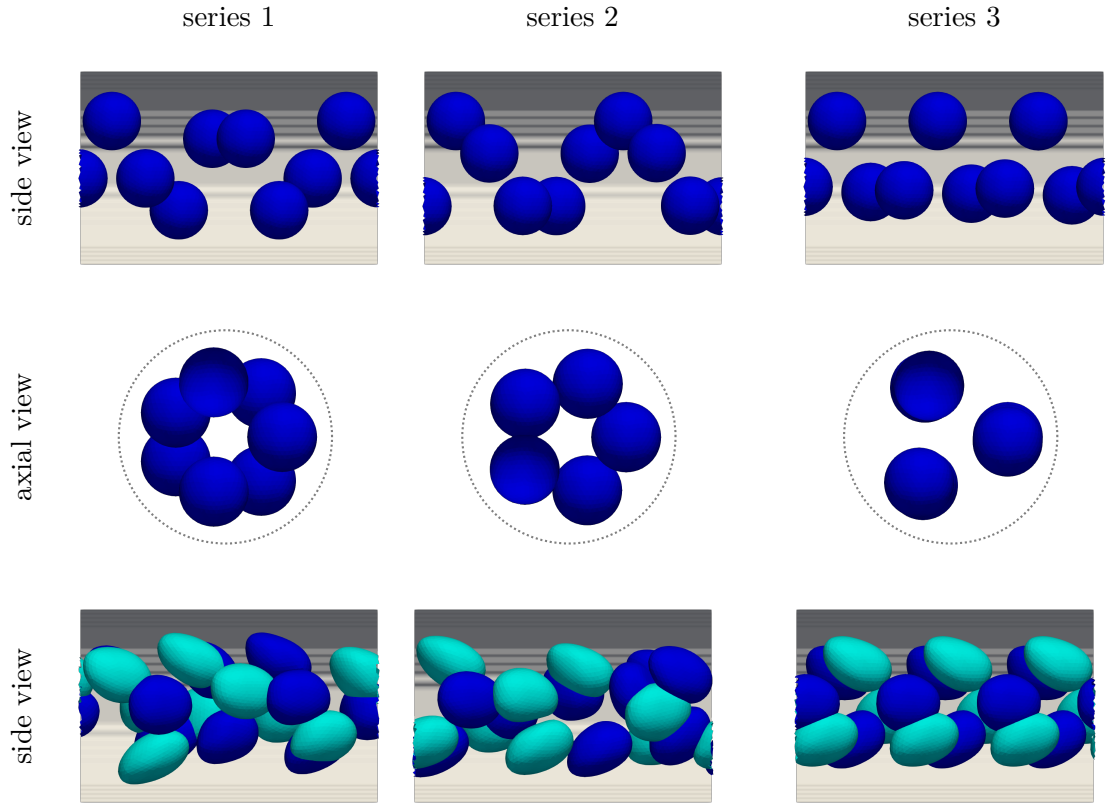

Table 15.4: Average deformation data of four cells in a cylinder as depicted in fig. A.3 and A.4. σ_q denotes the respective standard deviation.

n	$\alpha \pm \sigma_\alpha$	$\frac{1}{r_{\text{cell}}}(\Gamma \pm \sigma_\Gamma)$	$\frac{1}{r_{\text{cell}}}(d_{\max} \pm \sigma_d)$
		series 1	
1.0	0.019 ± 0.004	0.066 ± 0.006	2.32 ± 0.04
0.9	0.015 ± 0.006	0.059 ± 0.009	2.28 ± 0.05
0.8	0.017 ± 0.005	0.062 ± 0.009	2.29 ± 0.05
0.7	0.022 ± 0.005	0.070 ± 0.007	2.34 ± 0.04
0.6	0.021 ± 0.004	0.068 ± 0.006	2.33 ± 0.04
0.5	0.023 ± 0.004	0.070 ± 0.006	2.34 ± 0.04
0.4	0.023 ± 0.005	0.071 ± 0.007	2.35 ± 0.04
		series 2	
1.0	0.021 ± 0.005	0.068 ± 0.008	2.33 ± 0.04
0.9	0.019 ± 0.005	0.064 ± 0.008	2.30 ± 0.04
0.8	0.004 ± 0.003	0.037 ± 0.008	2.15 ± 0.05
0.7	0.003 ± 0.003	0.035 ± 0.007	2.14 ± 0.04
0.6	0.004 ± 0.002	0.038 ± 0.006	2.16 ± 0.03
0.5	0.003 ± 0.002	0.035 ± 0.005	2.14 ± 0.03
0.4	0.02 ± 0.01	0.07 ± 0.01	2.35 ± 0.08

15.3.3 Comparison between the simulations with four and nine cells

The graphs above have shown that the behavior of the cells during the simulation strongly depends on the initialization. Qualitatively, the same results as for the simulations with one cell have been observed. A quantitative view is provided in fig. 15.8. Here, the average of the deformation measures is shown with respect to the power-law exponent. With the only exception being the simulation series with four cells in which some are marginating towards the channel center, the same tendency is given for all simulation series: With decreasing power-law exponent n, the cell deformation is increasing. The explanation for this behavior can be found in the power-law profile, because the plateau-region in the channel center is not large enough to fit multiple cells in. A lower power-law exponent has to be chosen to achieve the desired results, as it will be shown in the next chapter.

Figure 15.8: Average deformation of cells with respect to the power-law exponent for simulation series with four and nine cells. The deformation clearly increases with decreasing power-law exponent.

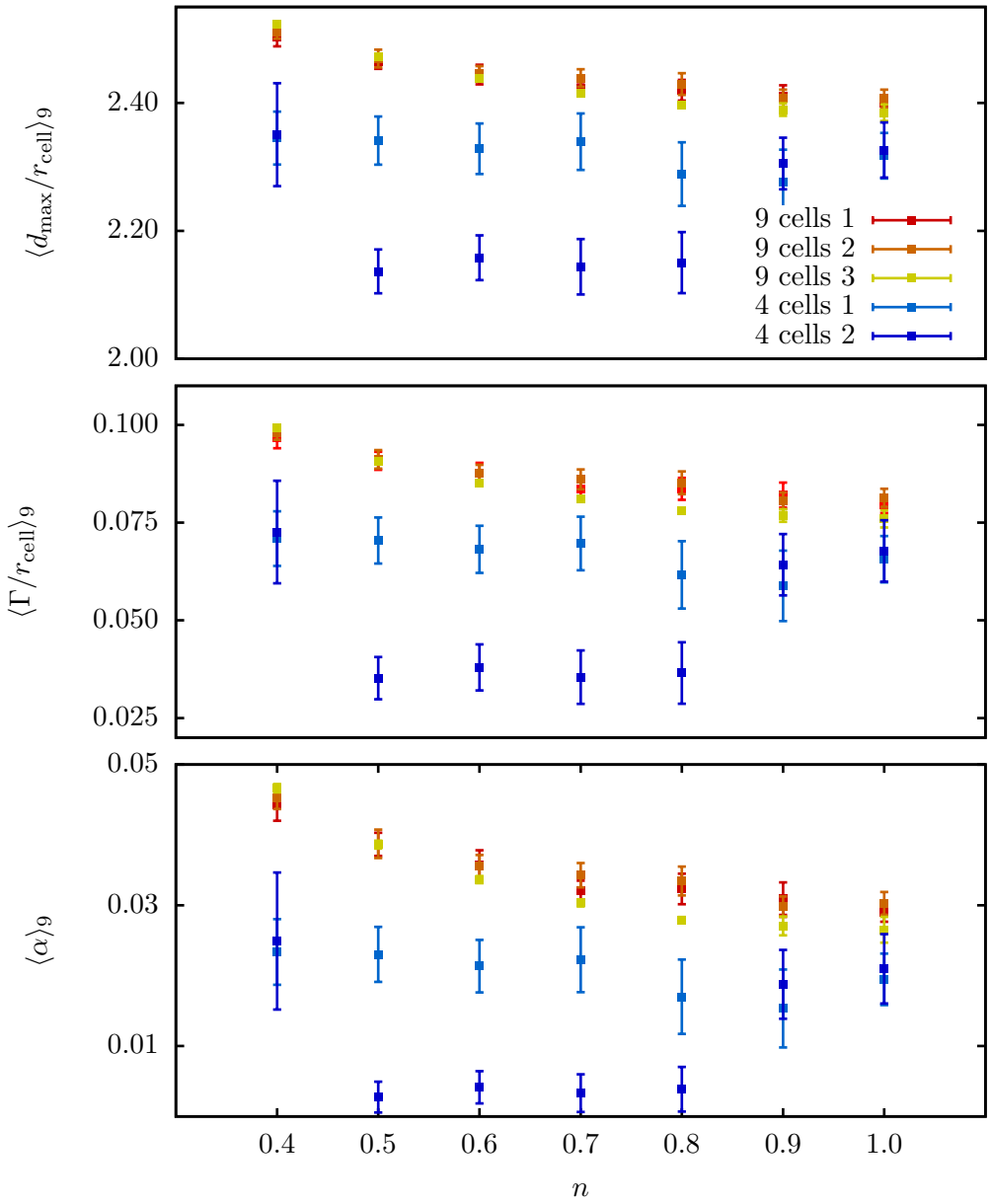

Table 15.5: Average deformation data of nine cells in a cylinder as depicted in fig. A.5, A.7 and A.6. σ_q denotes the respective standard deviation.

n	$\alpha \pm \sigma_\alpha$	$\frac{1}{r_{\text{cell}}}(\Gamma \pm \sigma_\Gamma)$	$\frac{1}{r_{\text{cell}}}(d_{\max} \pm \sigma_d)$
		series 1	
1.0	0.029 ± 0.001	0.080 ± 0.002	2.34 ± 0.01
0.9	0.031 ± 0.002	0.082 ± 0.003	2.41 ± 0.02
0.8	0.032 ± 0.002	0.084 ± 0.003	2.42 ± 0.02
0.7	0.032 ± 0.001	0.083 ± 0.002	2.42 ± 0.01
0.6	0.036 ± 0.002	0.088 ± 0.003	2.44 ± 0.02
0.5	0.039 ± 0.002	0.091 ± 0.002	2.46 ± 0.01
0.4	0.044 ± 0.002	0.098 ± 0.003	2.50 ± 0.01
		series 2	
1.0	0.030 ± 0.002	0.081 ± 0.002	2.41 ± 0.01
0.9	0.030 ± 0.001	0.081 ± 0.002	2.41 ± 0.01
0.8	0.033 ± 0.002	0.085 ± 0.003	2.43 ± 0.02
0.7	0.034 ± 0.002	0.086 ± 0.003	2.44 ± 0.01
0.6	0.036 ± 0.002	0.088 ± 0.002	2.45 ± 0.01
0.5	0.039 ± 0.002	0.091 ± 0.002	2.47 ± 0.01
0.4	0.045 ± 0.002	0.098 ± 0.002	2.51 ± 0.01
		series 3	
1.0	0.027 ± 0.002	0.076 ± 0.002	2.38 ± 0.01
0.9	0.027 ± 0.001	0.077 ± 0.002	2.39 ± 0.01
0.8	0.028 ± 0.001	0.078 ± 0.001	2.396 ± 0.004
0.7	0.030 ± 0.001	0.081 ± 0.001	2.414 ± 0.004
0.6	0.034 ± 0.001	0.085 ± 0.001	2.439 ± 0.004
0.5	0.039 ± 0.001	0.091 ± 0.001	2.473 ± 0.004
0.4	0.047 ± 0.001	0.099 ± 0.001	2.524 ± 0.004

16 Simulation of a 3D printer nozzle

This chapter is about the modeling of the nozzle of a real 3D bioprinter and the behavior of cells in this geometry in dependency of the strength of shear thinning.
The first section explains the general setup of the simulation and how parameters are chosen. Then, the effects of the transition on the fluid are investigated, characterizing the width of the transition with respect to the power-law exponent.
Afterwards, a cell is included into the channel at different radial offsets and its deformation is analyzed using different methods.

16.1 Simulation setup

The 3D printer nozzle is modeled using a cylindrical channel with radius 23 (13 µm) and length 256 (146 µm) along the x-axis, like depicted in fig. 16.1. The caps of the cylinder are used for inflow and outflow boundary conditions, i. e. an average fluid velocity is given for each node of the first and last cross section of the cylinder. Further, the transition from nozzle inside (e. g. a metal tube) to nozzle outside (e. g. air) is modeled with different boundary conditions. The usual bounce-back algorithm is applied to the first region to account for the no-slip boundary condition, the second region employs an extended version of the algorithm that still ensures a vanishing radial flow component but allows for a finite tangential component. This way a free-slip boundary condition is created. Note that this setup is only a valid representation of the transition from tube to air if the width of the liquid jet behind the transition is of the same size as the inner tube diameter.
The parameters are chosen as in chap. 13. The flow is driven using inflow and outflow boundary conditions with an average velocity of $u_{\text{avg}} = 0.2\,\frac{\text{mm}}{\text{s}}$ for the characterization of the transition width and $u_{\text{avg}} = 0.5\,\frac{\text{mm}}{\text{s}}$ for the cell simulations.

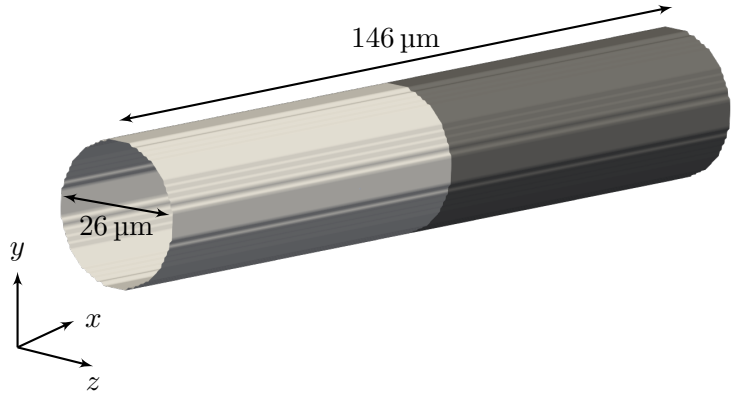

Figure 16.1: Simulation setup for the 3D printer nozzle. A cylindrical channel with a length and a diameter of 256 and 46 grid cells. The lighter color dentoes the no-slip region in the first half of the channel, the darker color the free-slip region.

16.2 Characterization of the transition width

This section focuses on the behavior of the fluid in dependency of the power-law exponent, i. e. the strength of shear thinning. The transition from the no-slip power-law profile to the free-slip plug flow is one of the influences which the cells are exposed to during the printing process. The present simulations are conducted to obtain a measure for the width of the transition, i. e. the x-interval in which the power-law profile changes over to a plug flow.
The figures 16.3 and 16.4 depict how such a measure can be defined. Both figures show a range in x-direction in front of and behind the change of the boundary condition indicated by the vertical gray line.
Fig. 16.3 plots the ratio of the channel center velocity u_{center} and the velocity u_{wall} at the first node next to the wall. This fraction equals 1 if a plug flow is fully developed, i. e. the velocity is the same for all lateral nodes at a given x-position. In the power-law region, this ratio has a constant value that depends on the power-law exponent.
To simplify the analysis, the second fig. 16.4 plots the absolute of the derivative of this fraction, calculated from the data using finite differences. Doing so, the range of influence of the transition can be seen easily: The power-law and the plug flow region show a constant in the $\frac{u_{\text{center}}}{u_{\text{wall}}}$-plot, thus, the derivative vanishes there. What stays is a clear peak of certain hight and width, that can be used to quantify the transition width. Since the maximum height of the peaks depends on n, it is obvious that a fixed threshold for the derivative would lead to a transition width that strongly depends on n. Instead using the width at a certain percentage of the maximum height of each curve leads to the data shown in fig. 16.2. If the full width at half maximum (FWHM) is considered, the transition width is approximately constant and independent of the power-law exponent. For lower percentages, the width of the transition decreases with n, i. e. more shear thinning fluids exhibit a wider transition.
To get a qualitative impression of the transition, fig. 16.5 shows the x-component of the velocity field in the whole simulation channel for different power-law exponents n. The influence of the transition at the center and the inflow boundary at the very beginning can be distinctly seen. It is also clear that the maximum velocity in the channel center in the no-slip region must decrease with decreasing n, as the flow profile gets more and more flat like the plug flow present in the right half. Fig.16.6 further shows the y-component of the velocity field, i. e. the lateral flow components that affect the cell in later simulations.

16.3 Cell deformation during transition

As in the simulations with spherical cells in a cylinder, this section presents the results of the nozzle simulations. The deformation of the cell is again characterized using the techniques in 14.
It has already been shown that the radial position of the cell has a strong influence on the deformation. Therefore, simulations with three different offsets are performed. As it is depicted in fig. 16.7, *offset 0* denotes a cell starting at the center of the channel and is colored red in all plots. *Offset 1*, colored in green, is shifted one cell radius r_{cell}. The third

Figure 16.2: Transition width calculated by measuring the full width of the peak in fig. 16.4 at a given percentage of the maximum height.

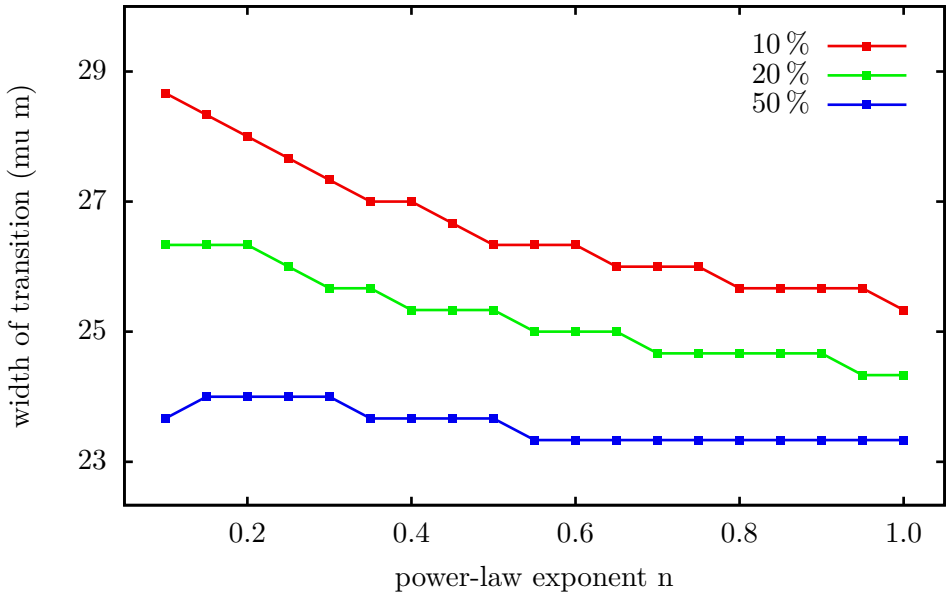

one, *offset 2*, is placed very close to the physical boundary and is colored blue. Note, that the wall is approximately halfway between the two outer nodes.

16.3.1 Newtonian fluid

First of all, the effects of the nozzle geometry and the boundary conditions in a Newtonian fluid have to be identified to later distinguish these from effects due to the shear thinning fluid properties.
Fig. 16.9 shows the velocity profile in a part of the channel around the transition including the cells for different initial offsets.
The first image shows the centered cell, which remains a axisymmetric shape during the simulation. In front of the transition, a cone like shape is attained. This is due to the symmetrical flow profile around the cell that has its maximum in the channel center. During the transition, the cell is pushed together in axial and stretched in radial direction, resulting in an ellipsoidal shape. In the plug flow region behind the transition, the shape relaxes toward the original sphere.
The green cell in the second image depicts the deformation of an off-centered cell. The shape in front of the transition is not symmetric, the center of mass (COM) being pulled towards the channel center. During the transition, while being elongated in radial direction as the centered cell, it moves radially outwards. After the transition, the cell shape relaxes, the final offset being visibly larger than the initial.
Very similar looking to the second image is the blue cell with the highest offset in the last image. However, in front the transition the deformation is visibly stronger than for smaller offsets, which has already be seen for the simulations in a cylindrical channel and

Table 16.1: Reynolds number and capillary number for the nozzle simulations for the corresponding power-law exponents.

n	1.0	0.9	0.8	0.7	0.6	0.5	0.4
Re	0.011	0.010	0.009	0.008	0.007	0.006	0.005
Ca	0.24	0.26	0.28	0.31	0.36	0.42	0.51

is a results of the higher shear rate at the channel wall. During the transition, there is again a shift in the radial offset observed.

16.3.2 Power-law exponent ranging from 0.4 to 1.0

16.3.2.1 Lateral shift during transition

Before analyzing the deformation, the shift in the radial offset of the cell is investigated depending on the shear thinning strength. Fig. 16.10 shows the relative lateral position of the center of mass of the cells during the transition, with a darker color indicating stronger shear thinning.
In front of the transition in the middle of the channel, the cells with larger offset marginate towards the center much stronger than the ones closer to the center. It is also visible that the margination is weaker for lower power-law exponents.
During the transition, the lateral shift is clearly visible with the final offset being significantly higher than the initial. The green curves show, furthermore, that the radial shift is less for increasing shear thinning strength. This is not observed for the blue curves, because the cells are already initialized very close to the boundary and the interaction between wall and cell does not allow the cells for penetrating the boundary. Nevertheless, an indication of the same trend is visible by looking closely at the blue curves behind the transition: For the Newtonian case, the COM moves further outside than for the shear thinning fluid, but after that it relaxes to approximately the same value as the other curves. This behavior can also be observed in fig. 16.9, where the blue cell shows a clear indentation at the side facing the boundary. This makes the COM move outside before the cell relaxes back to its spherical shape.
The lateral movement of the cell can be explained considering the lateral velocity components during the transition: The depiction in fig. 16.6 shows that the lateral components of the flow velocity have the same magnitude but deceasing thickness with decreasing n. Therefore, cells are dragged outwards less if the fluid is more shear thinning.

16.3.2.2 Cell velocity during transition

Another quantity helpful for analyzing the cell behavior is the center of mass velocity u_{COM} shown in fig. 16.11. There are three things to note in this plot:
First of all, it can be seen that the assumption of the analytical profile in the no-slip region is still approximately valid, because the average velocity that is derived from the analytical expression and used for the inflow condition corresponds to the cell velocity in

the plug flow region.
Secondly, for the red and green curves, which are closer to the center, the velocity in the no-slip half is significantly higher with increasing n. This can be understood by considering the velocity profiles in this region. As the flow rate is kept constant, the shear thinning profiles exhibit a smaller maximum velocity than the Poiseuille profile. A cell moving close to the center will therefore have a higher velocity in the Newtonian case.
The exact opposite is seen at the blue curves. The high offset means that the cell is in a region where the velocity of the power-law profiles is above the Poiseuille profile and therefore attains a greater speed. Due to the margination of the cell, however, the velocity of the cell in Newtonian fluid increases stronger than the others.

16.3.2.3 Deformation during transition

The deformation during the transition is now analyzed with respect to the power-law exponent n of the fluid. Like in the last chapter, the maximum elongation $d_{\max}$, the deviation from a spherical reference Γ and the asphericity α as defined in 14 are investigated. By looking at fig. 16.12, it is clear that the different methods show again the same characteristics. The only significant difference is given by the red curves in front of the transition. Solely Γ shows a clear deviation from zero, $d_{\max}$ only little, and α nearly vanishes in this case. This has already be seen in the simulations of a single cell in the cylinder, where the asphericity is of order 10^{-6} (cf. fig. 15.2).
As expected from the simulations before, a higher offset results in a stronger deformation in the no-slip region. Decreasing the power-law exponent results in a higher deformation for the blue curves, and a rather constant value for the green ones. The green and red curves do in most cases not reach a stable value before entering the transition.
During the transition, all cells show the same behavior: Immediately before the transition the deformation decreases a bit to then increase strongly up to a maximum value and finally relax back to the original shape. It is clearly visible that the deformation is consistently higher for lower n and that the relaxation takes significantly longer, likewise. This longer relaxation is a consequence of the chosen viscosity model. Applying a power-law in the plug region, the viscosities become very large causing the viscous fluid forces to dominate the cell's elastic forces. The indentation right in front of the transition for the blue and green curves is deeper for the Newtonian fluid. This is most probably due to the lateral movement of the cell, which is also more significant in the Newtonian case.
The maximum value of the deformation seems to be very similar for both the red and green curves, and for some cases of the blue curve as well. This can be coincidentally, or could be identified as a pure influence of the shear thinning fluid in this geometry. The assumption can be supported by the other analysis methods which show similar behavior and further simulations in the next section, where the same is observed.
This result is especially counterintuitive regarding the behavior of the cell moving along the central axis. Consider the velocity profiles in fig. 16.5: First of all, the difference in maximum velocity from no-slip to free-slip region is much smaller for $n = 0.4$ than for the Newtonian fluid. Furthermore, when considering the lateral flow during the transition as depicted in fig. 16.6, the region where the radial flow can influence the cell movement is visibly narrower.

Table 16.2: Reynolds and capillary number for the simlations with Newtonian and strongly shear thinning fluid. The capillary number in the latter case is nearly nine times higher.

n	1.0	0.1
Re	0.011	0.001
Ca	0.24	2.1

An approach to explain this behavior is given by the value of the capillary number, listed in tab. 16.1. As in the cylinder simulations, Ca is roughly twice as large for the lowest power-law exponent compared to the Newtonian case. With the lateral flow velocity having the same magnitude and the cell passing the transition with a lower velocity for $n = 0.4$, a qualitative explanation for the higher deformation can be given.

16.3.3 Comparison between Newtonian and strongly shear thinning fluid

In this section, the shear thinning properties are chosen even stronger than before, comparing a Newtonian to a power-law flow with $n = 0.1$. The simulated profiles in the no-slip region are depicted in fig. 16.7. Both the red and green cell are experiencing vanishing velocity gradients and should not deform significantly in the no-slip region. As the velocity profile for the shear thinning fluid is even closer to a plug flow than in the previous simulations, one would expect less deformation during the transition if n is chosen small enough.
Simulations have been performed for $n = 1.0, 0.1, 0.01, 0.001$, but the latter two appeared to be unstable, and, considering the error of the method as discussed in chap. 12, the simulation data would not be reliable either.
A look at the deformation data in fig. 16.8 confirms the expectation of the cells with offset 0 and 1 being nearly undeformed in the no-slip region in front of the transition. The blue curve shows similar behavior like in the previous section. This can also be seen in fig. 16.13, which shows the cell shapes during the simulation.
Nevertheless, when the cells reach the transition, they show no difference in behavior to the previous simulations. The deformation is still increasing with decreasing n and the red and green curves reach the same maximum deformation during the transition for a given power-law exponent and relax very similar.
This effect is still explainable by the ratio of the fluid forces to the cell's elastic forces that is nine times higher for $n = 0.1$ (cf. tab. 16.2) and the lateral flow components at the transition.
But as this effect must drop down if the no-slip region power-law profiles equals more and more the free-slip plug profile, the expected behavior can possibly be observed if the simulation setup is changed: A channel with a larger diameter and still a very low power-law exponent could help reducing the lateral flow, at least in the central region with the cell. This simulations are still to be performed and are, unfortunately, not part of this thesis.

Figure 16.3: The ratio between the velocity at the channel center u_{center} and near the channel wall u_{wall} as a measure for the developed plug flow.

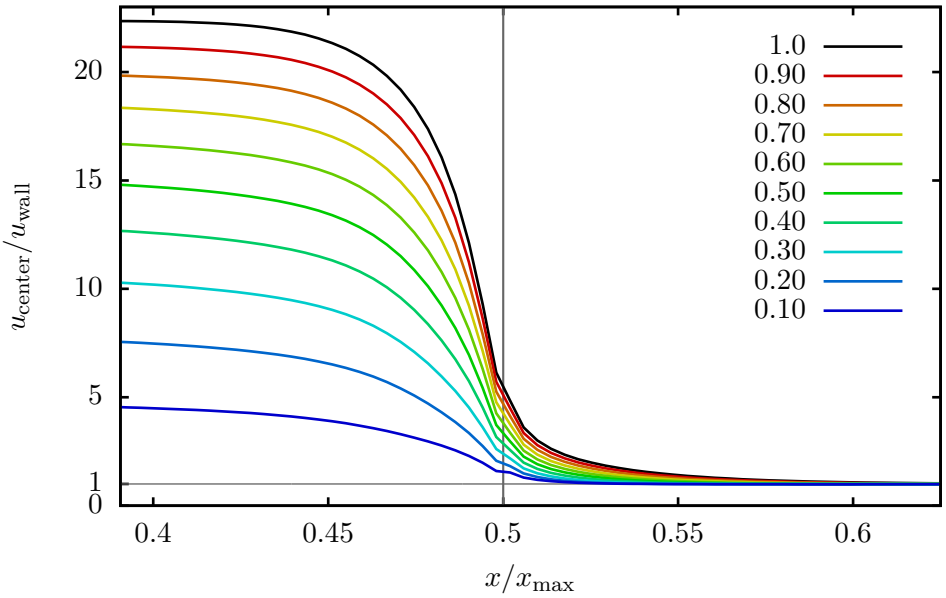

Figure 16.4: Derivative of the velocity ratio calculated from the data in the above figure using finite differences.

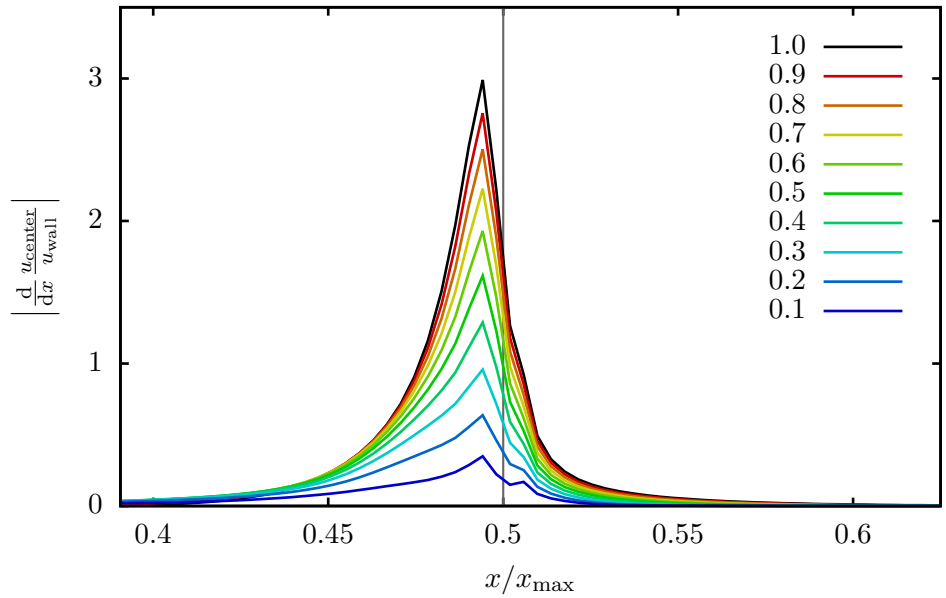

Figure 16.5: Magnitude of the velocity field from no-slip to free-slip transition. The influence of the inflow boundary at the left and the transition are less significant for lower n. The plug flow region has the same velocity for all exponents.

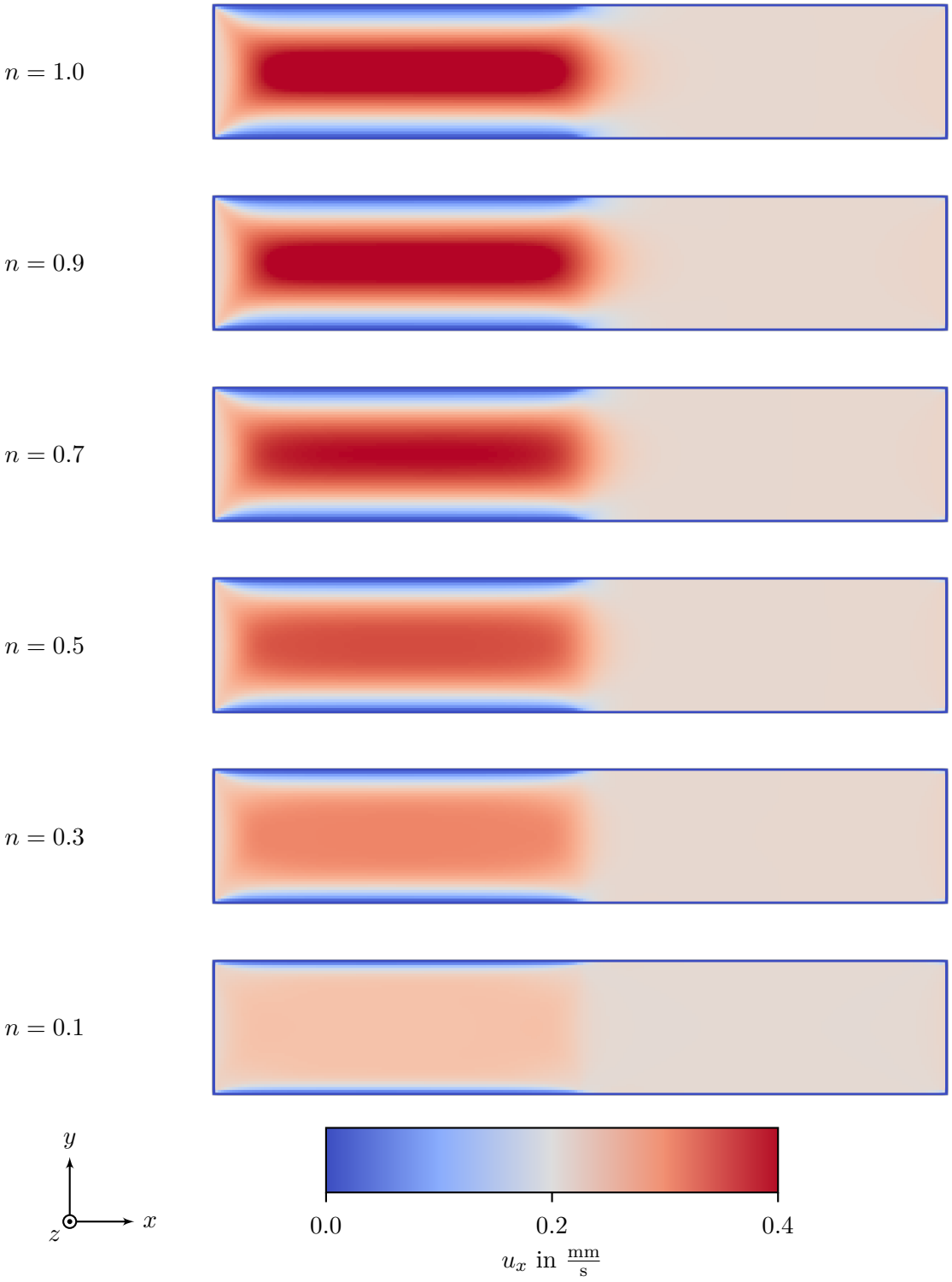

Figure 16.6: Magnitude of the lateral flow velocity. Red color denotes upward streaming, blue downwards. The thickness of the lateral flow region at the transition decreases with decreasing power-law exponent, but the maximum magnitude is the same.

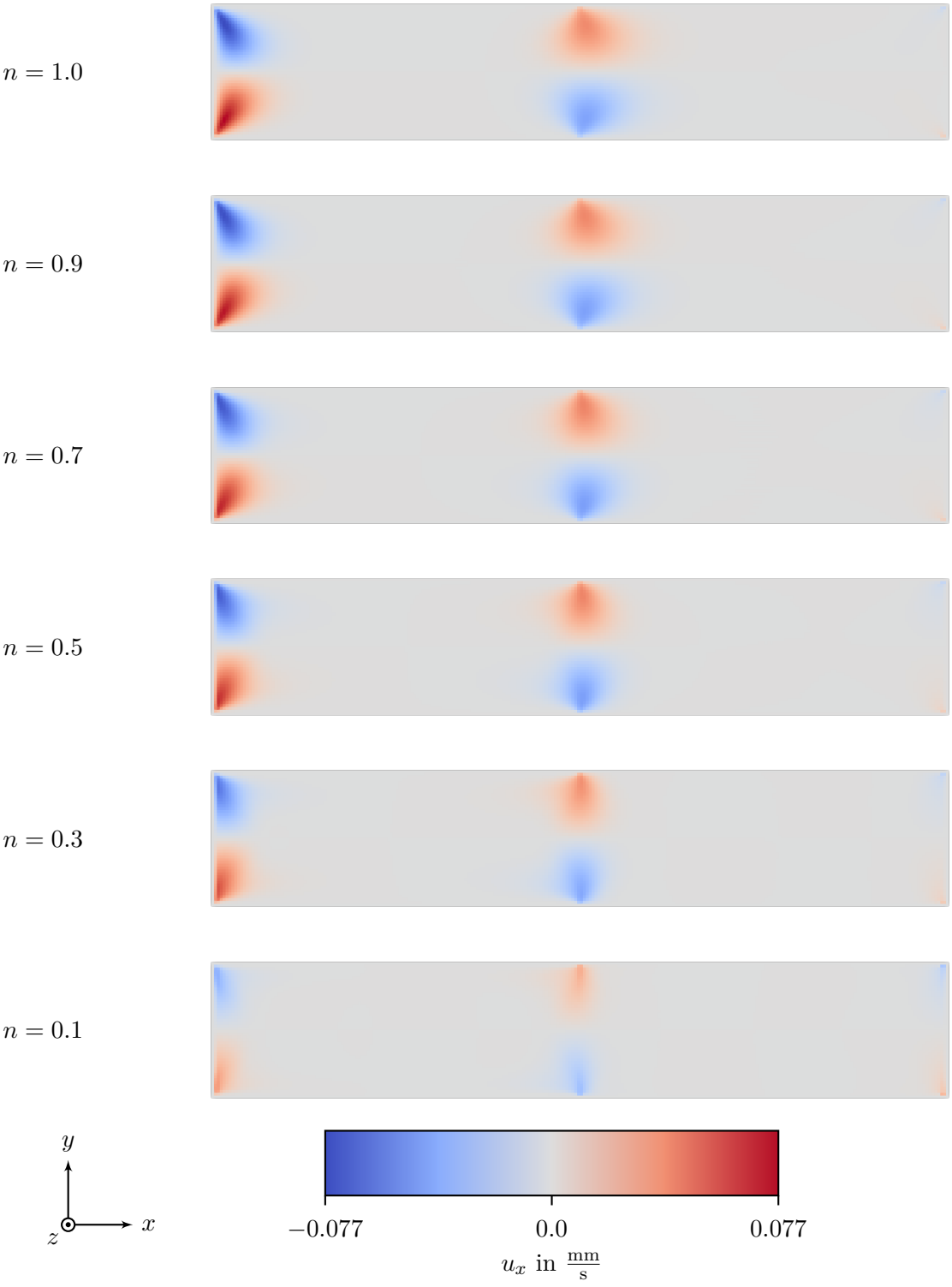

Figure 16.7: Color coding for the different offsets and a Newtonian ($n = 1.0$) and a strongly shear thinning velocity profile ($n = 0.1$) obtained from simulation. They gray vertical line indicates the channel center.

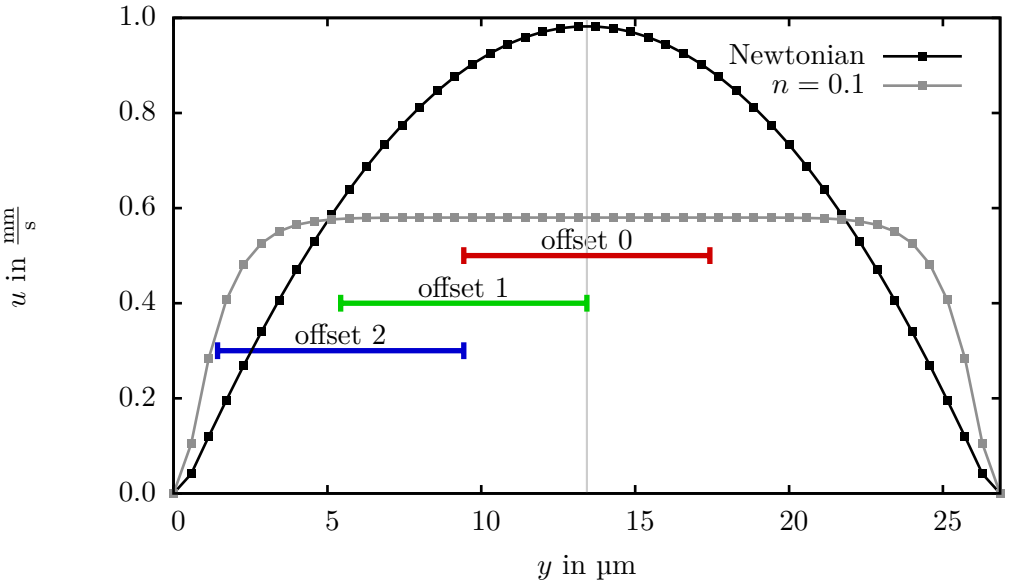

Figure 16.8: Deviation Γ from the spherical reference for a Newtonian and strongly shear thinning fluid ($n = 0.1$). Even though the flow profiles is close to a plug flow, the deformations still show the same characteristics as for higher n. Nevertheless, the nearly vanishing deformation of the red and green curves corresponds to the expectation.

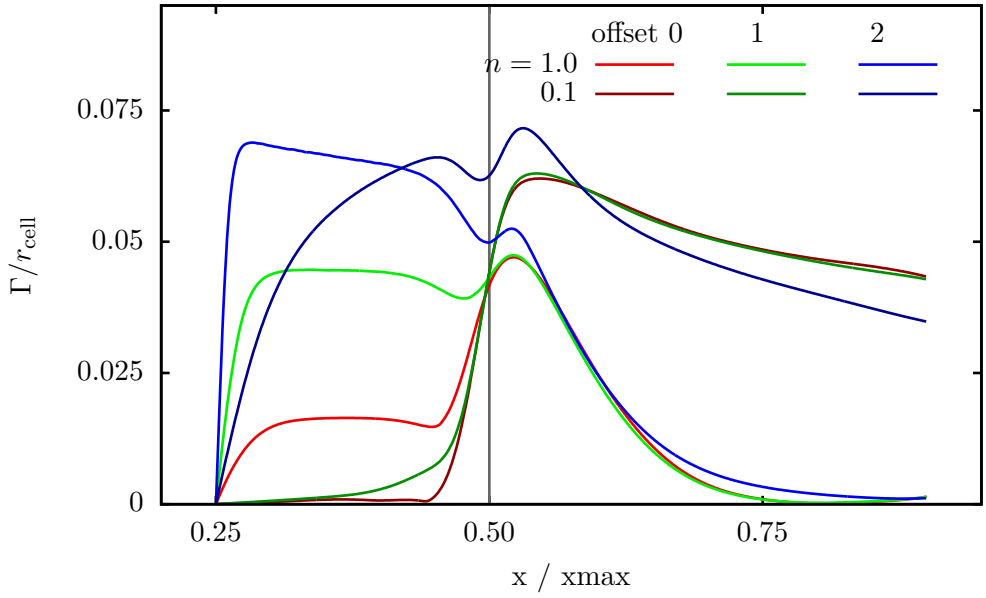

Figure 16.9: Deformation of the cell in a Newtonian fluid during the transition from no-slip to free-slip boundary for different intial radial offsets. The shift in lateral offset is significant for the green and blue colored cell. The blue cell is furthermore visibly dented in right behind the transition as a consequence of the cell-boundary repulsion.

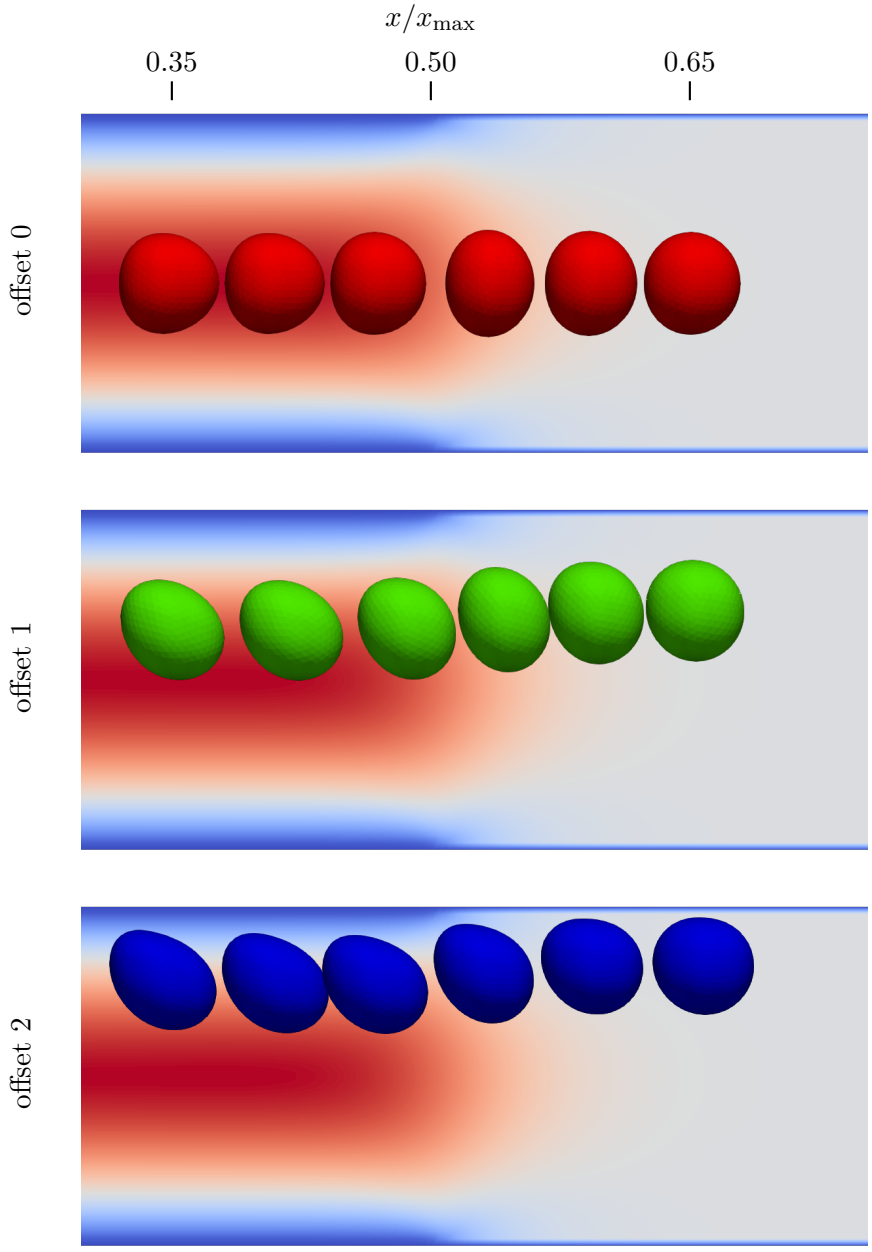

Figure 16.10: Center of mass position with respect to the channel radius of the cell during the transition for different n. The green curves show a clear trend with decreasing shift for decreasing exponent. The blue curves converge as the maximum offset is reached considering the cell-wall repulsion.

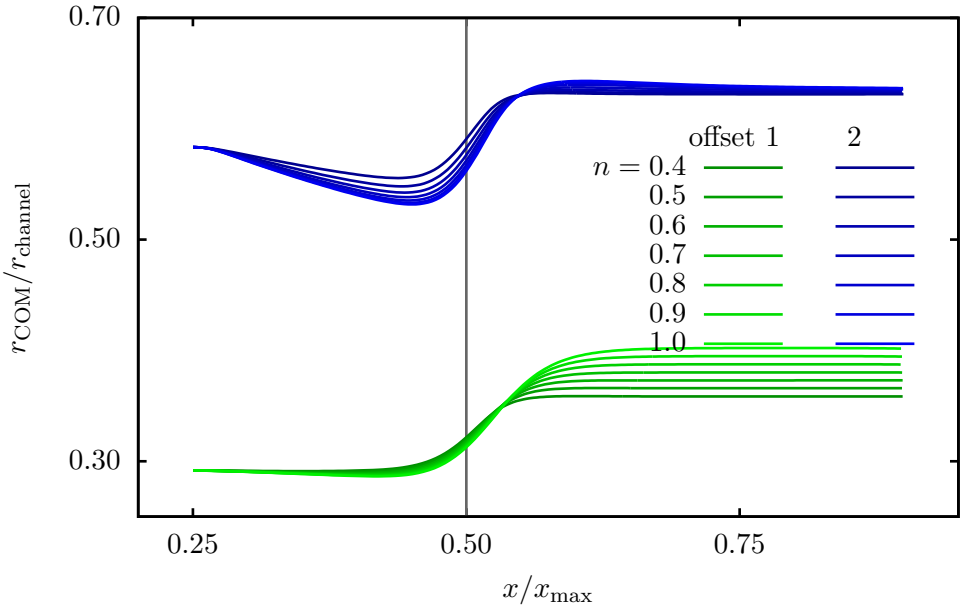

Figure 16.11: x-component of the COM velocity of the cell during the transition. Centered cells move faster as they are closer to the flow maximum, which decreases with decreasing n. The blue curves show the influence of the sharper edge of the power-law profile at the channel wall, making cells faster for stronger shear thinning. As a consequence of the fixed flow rate, all cells relax to the same velocity in the plug flow region.

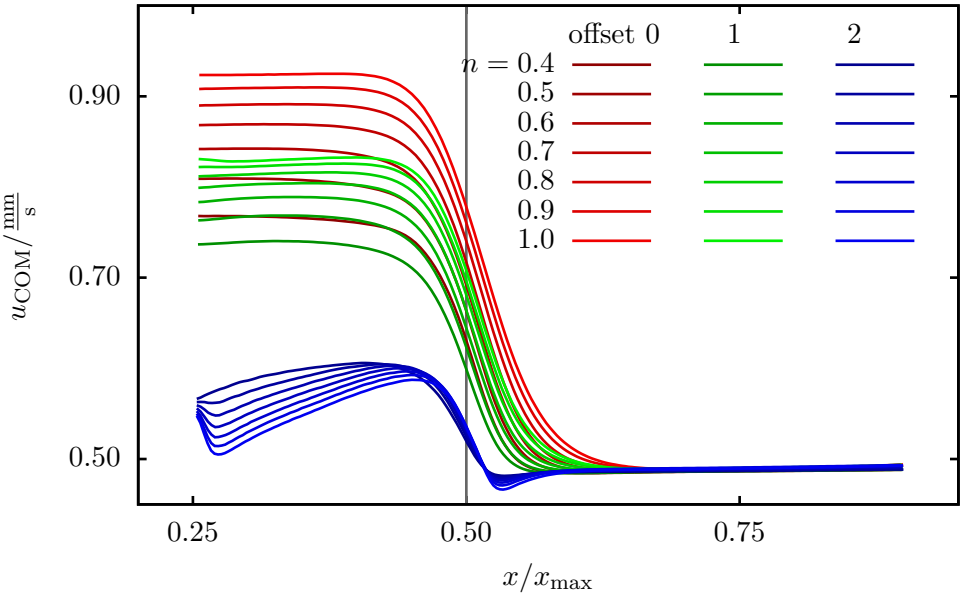

Figure 16.12: Deformation of the cell during transition. In front of the transition, cells are deformed less with increasing shear thinning when they are closer to the center. At the transition the deformation is consistently higher for lower n and the relaxation to the original shape behind the transition takes longer as a consequence of the higher velocity. Despite there is visible deformation in front of the transition, the asphericity is very small for the red curves. However, the other methods show the expected behavior of a decreased deformation for lower n.

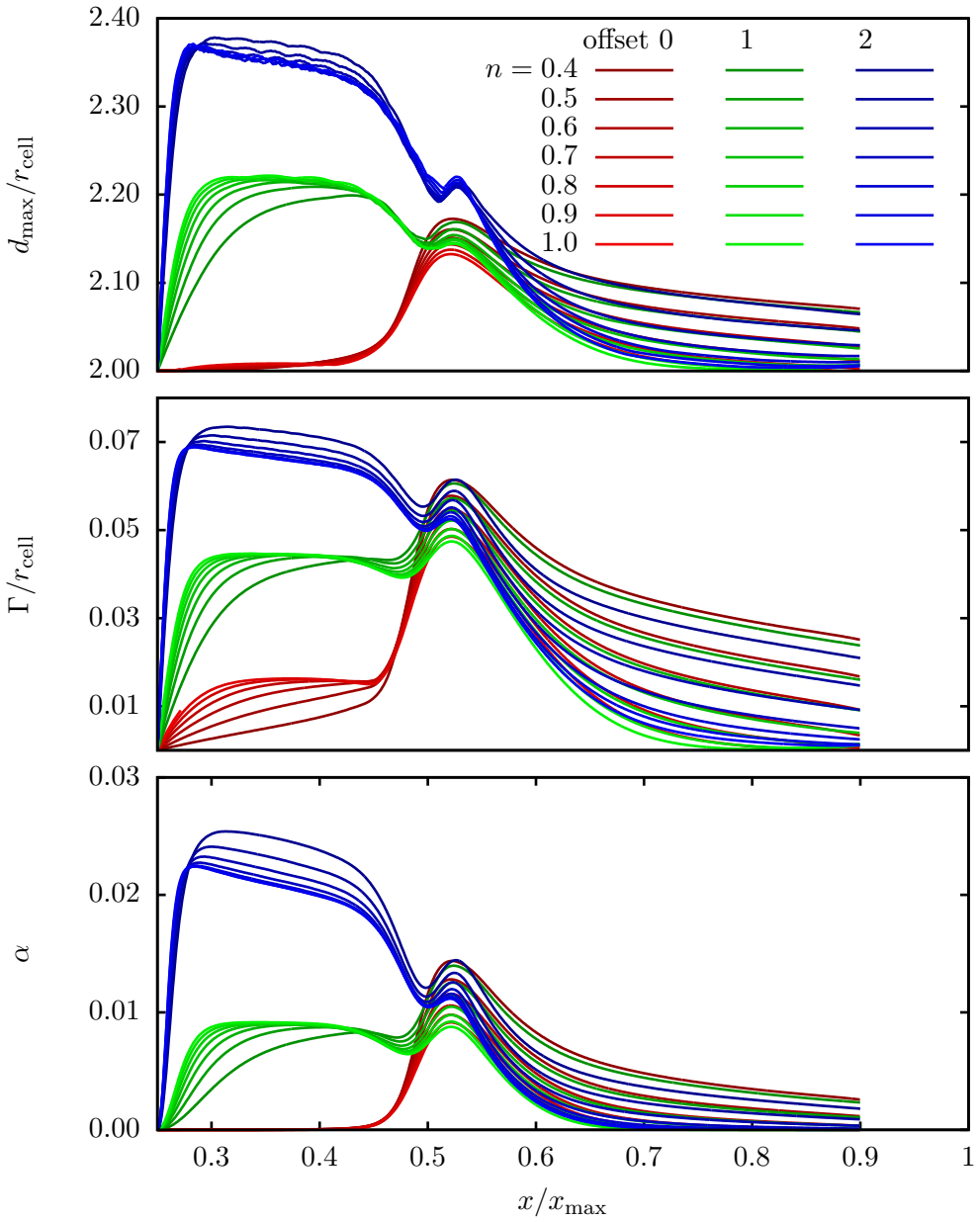

Figure 16.13: Deformation of the cell in a strongly shear thinning fluid ($n = 0.1$) during the transition from no-slip to free-slip boundary for different intial radial offsets. Due to the broad velocity profile, the red and green cells are nearly undeformed in front of the transition. During the transition, the are stretched laterally. The offset shift for the green cell is significantly less than in fig. 16.9. The blue cells are still deformed as they are close to the boundary.

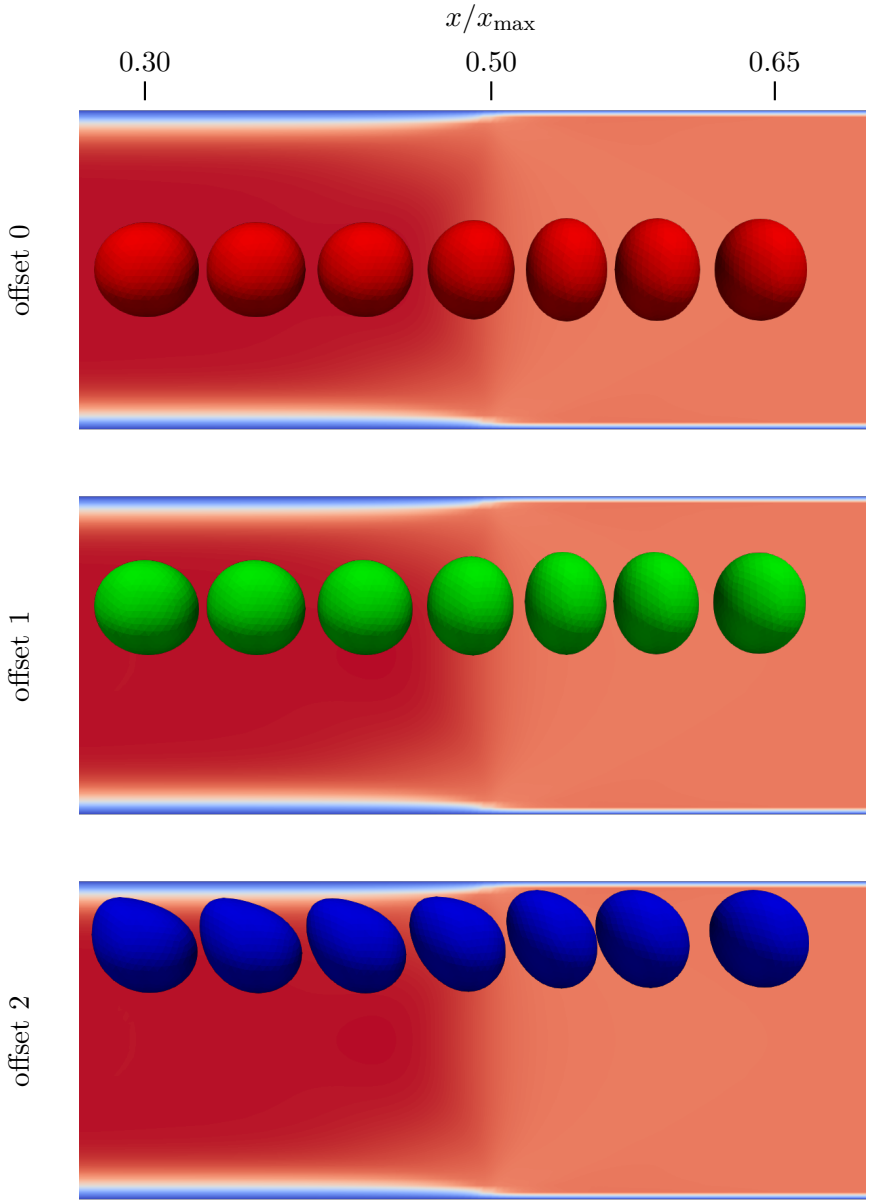

Part V

Conclusion and outlook

The aim of this thesis has been the investigation of the deformation of cells in a shear thinning fluid. It has been shown that the expected decreasing deformation for cells in shear thinning fluids can only be observed for cells located in the plateau region of the flow. In contrast, the deformation of a cell passing the nozzle transition is significantly larger than in a Newtonian fluid, irrespective of its radial position.

During this thesis, the behavior of spherical cells in a flow of shear thinning fluids has been investigated using the ESPResSo simulation software, which was therefore extended with several viscosity models.
The power-law model and the truncated power-law model have been shown to produce second order accurate results for smaller systems by comparison of the simulation data with analytical flow profiles.
The deformation of one and multiple cells in a cylindrical setup has been investigated and it has been shown that the initial position and the radial position of cells during the simulation have a strong influence on the deformation. When initialized in a certain way, cells may migrate towards the channel center or stay off-center. Furthermore, cells that are closer to the channel center are significantly less deformed, especially for low power-law exponents, when the plug-flow region is large enough to fit a cell in. With increasing shear thinning strength, however, the cell's average deformation increases likewise. This is a result of the power-law flow profile, which exhibits larger shear rates near the boundary.
The simulations of the cells passing through a 3D printer nozzle have shown that the deformations in front of the transition still depend strongly on the radial position of the cell. The more shear thinning the fluid is, the wider is the radial interval where a cell is significantly less deformed than in a Newtonian fluid. Passing the transition off-centered results in a radial shift that is larger for Newtonian fluids. This is followed by the relaxation of the cell to its original shape, which takes significantly longer in a shear thinning fluid as the viscosities are much larger. It has further been shown that the cells are more deformed passing the transition when the shear thinning is stronger. This is explained by the higher capillary number, which tells that the viscous fluid forces dominate the cells' elastic restoring forces. Thus, the lateral flow components stretching on the cell at the transition are stronger for increasing shear thinning.

This thesis presents a first approach to simulating cells in shear thinning fluids and shall lay the foundation for future studies on this topic. Since a big part of the work on this thesis was the implementation and validation of the method, the parameters in

the simulation were chosen in a way that – first of all – simulation stability is achieved. Consequently, there is still a lot of room for possible improvements. Starting from this point, focus can be shifted to a more detailed reproduction of a real 3D printer. This includes the rheological properties of actually used bioinks and the elastic properties of other cell types. Not least does the geometrical realization of the nozzle affect the fluid as well, which can be considered in the simulations.

Appendix

Figure A.1: Deformation of a single cell flowing at the center of a cylinder. After an equilibration, nearly stationary values are assumed in all simulations. With increasing shear thinning, the deformation first increases due to the stronger fluid forces, then it decreases again, when the power-law profile is wide anough to fit a cell.

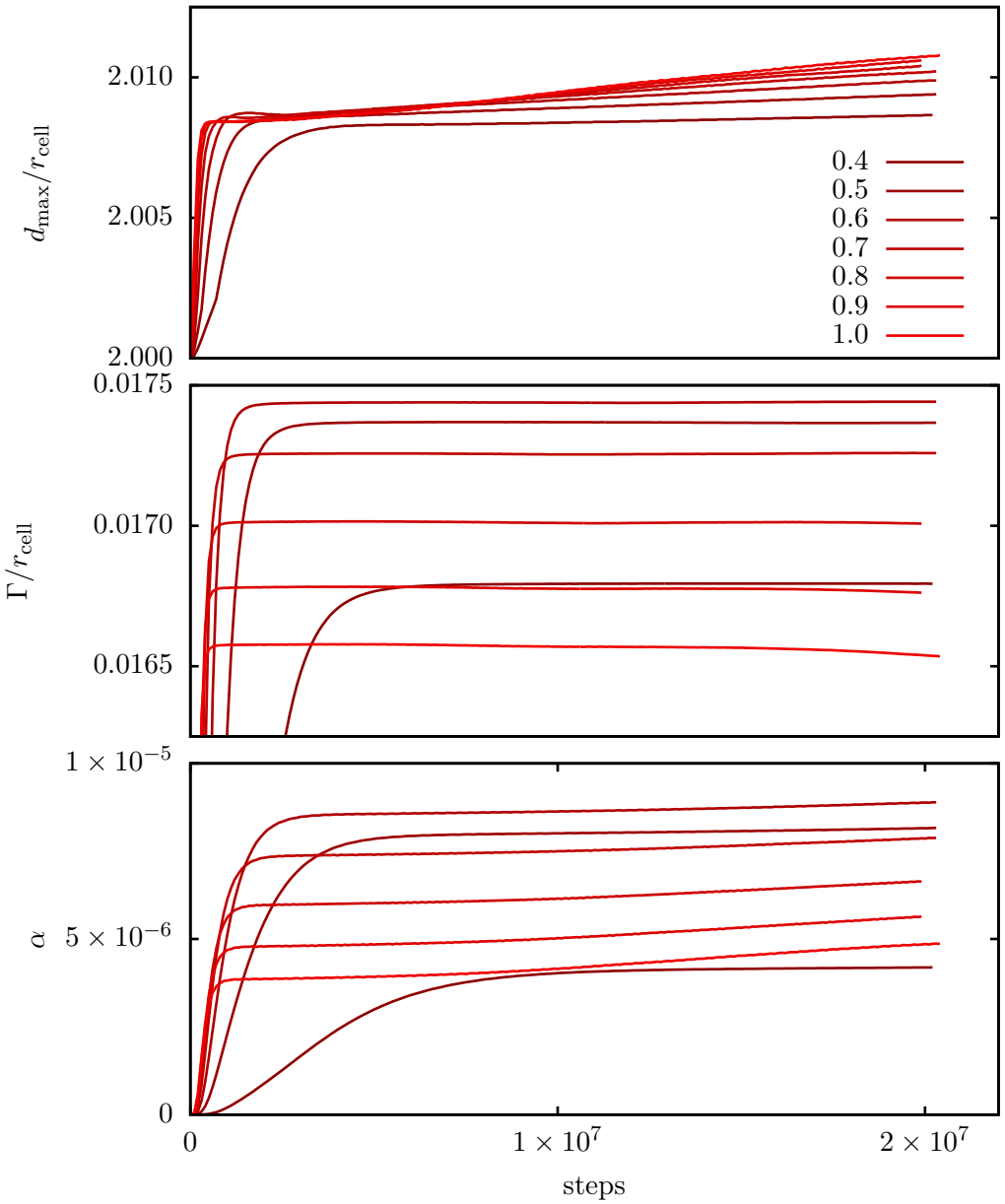

Figure A.2: Deformation of a single cell flowing through a cylinder initialized near the boundary. The radial position of the cell is the major influence on the deformation. For increasing shear thinning strength, the deformation is nevertheless consistently higher.

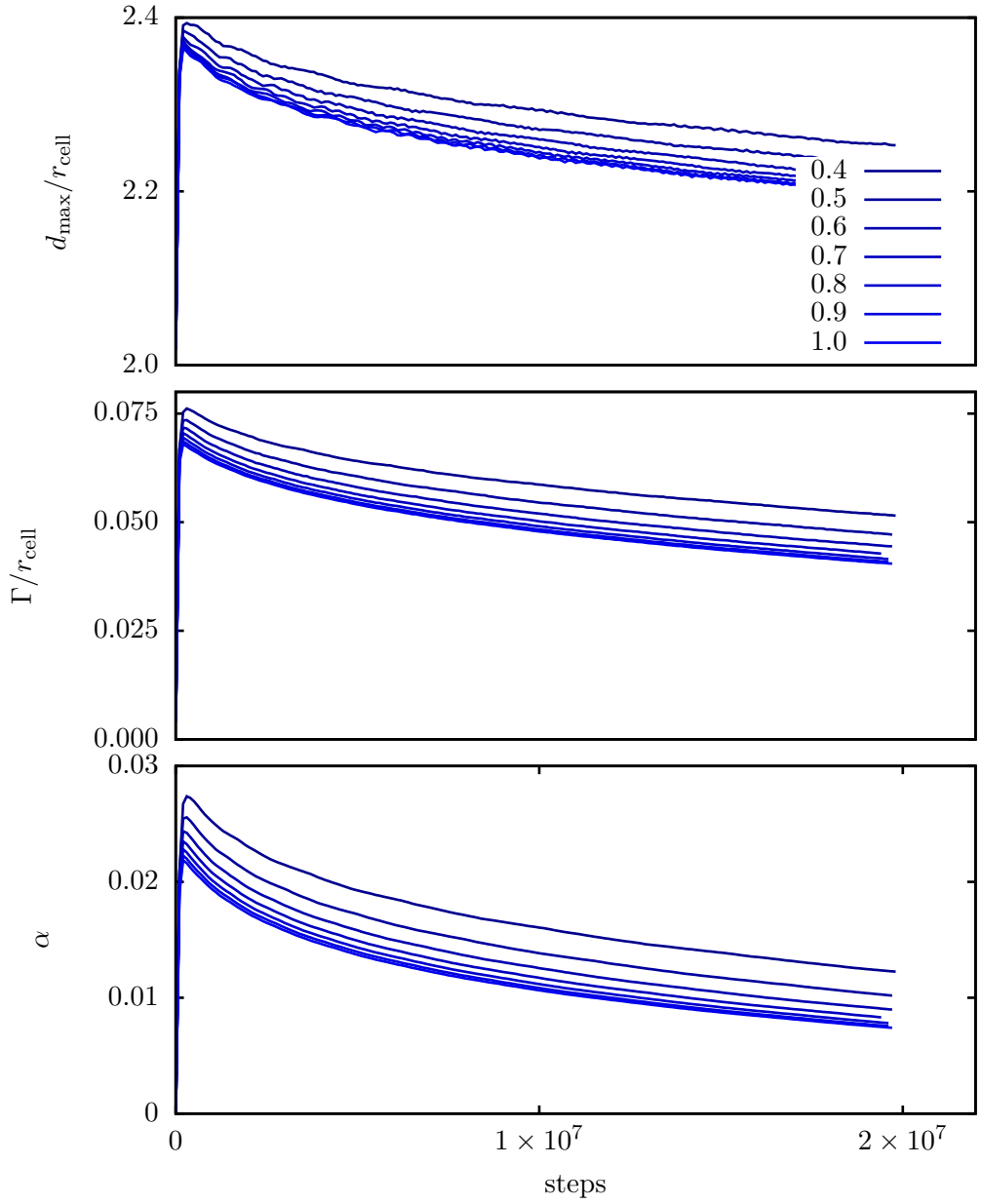

Figure A.3: Series 1: Average deformation of four cells in a cylinder. Due to the strong fluctuations, a clear result is not visible. But looking closely reveals that darker curves – representing stronger shear thinning – attain higher values.

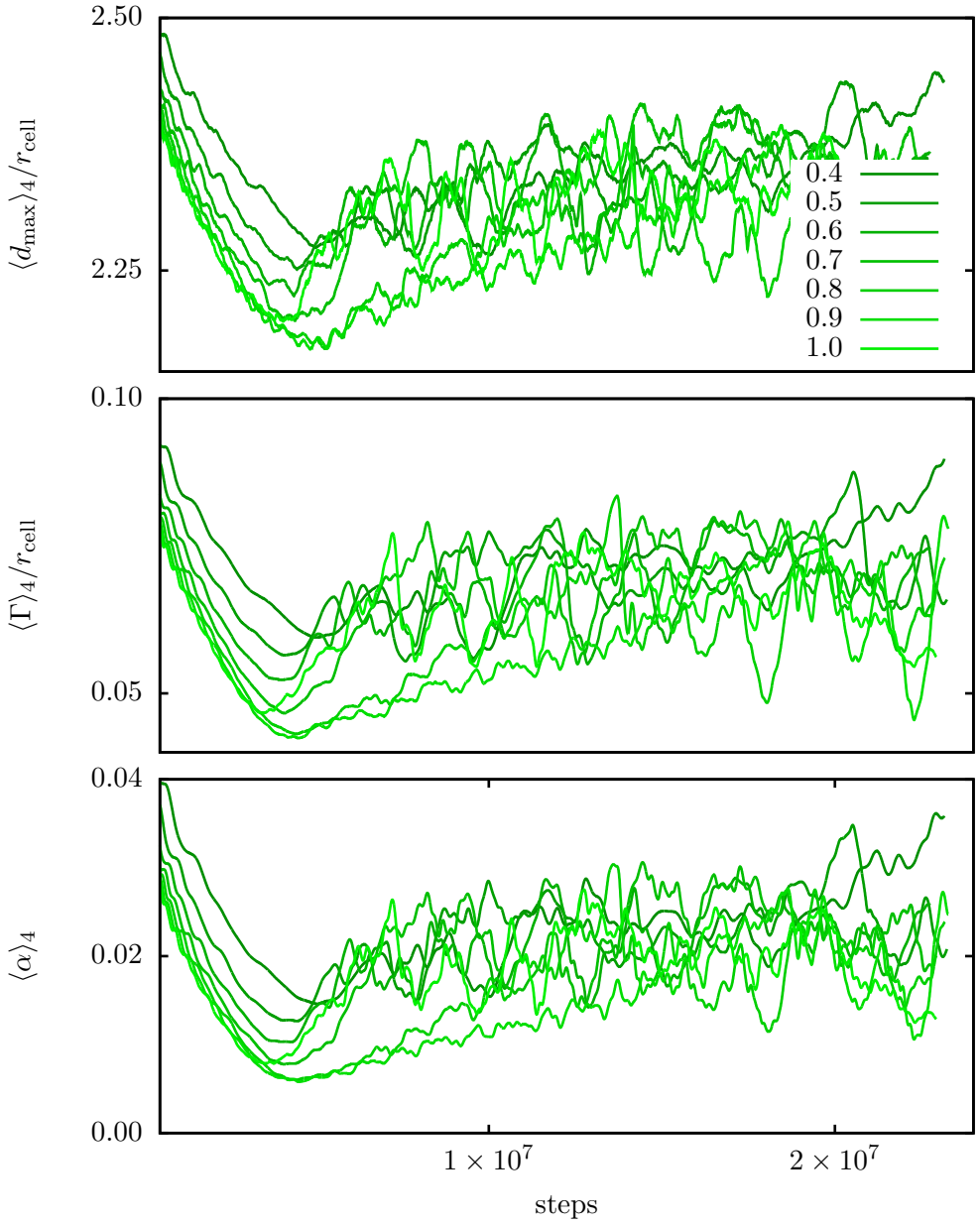

Figure A.4: Series 2: Average deformation of four cells in a cylinder. Most probably due to the initialization, the cells in several of these simulations marginate towards the channel center and line up, resulting in the decreasing deformation.

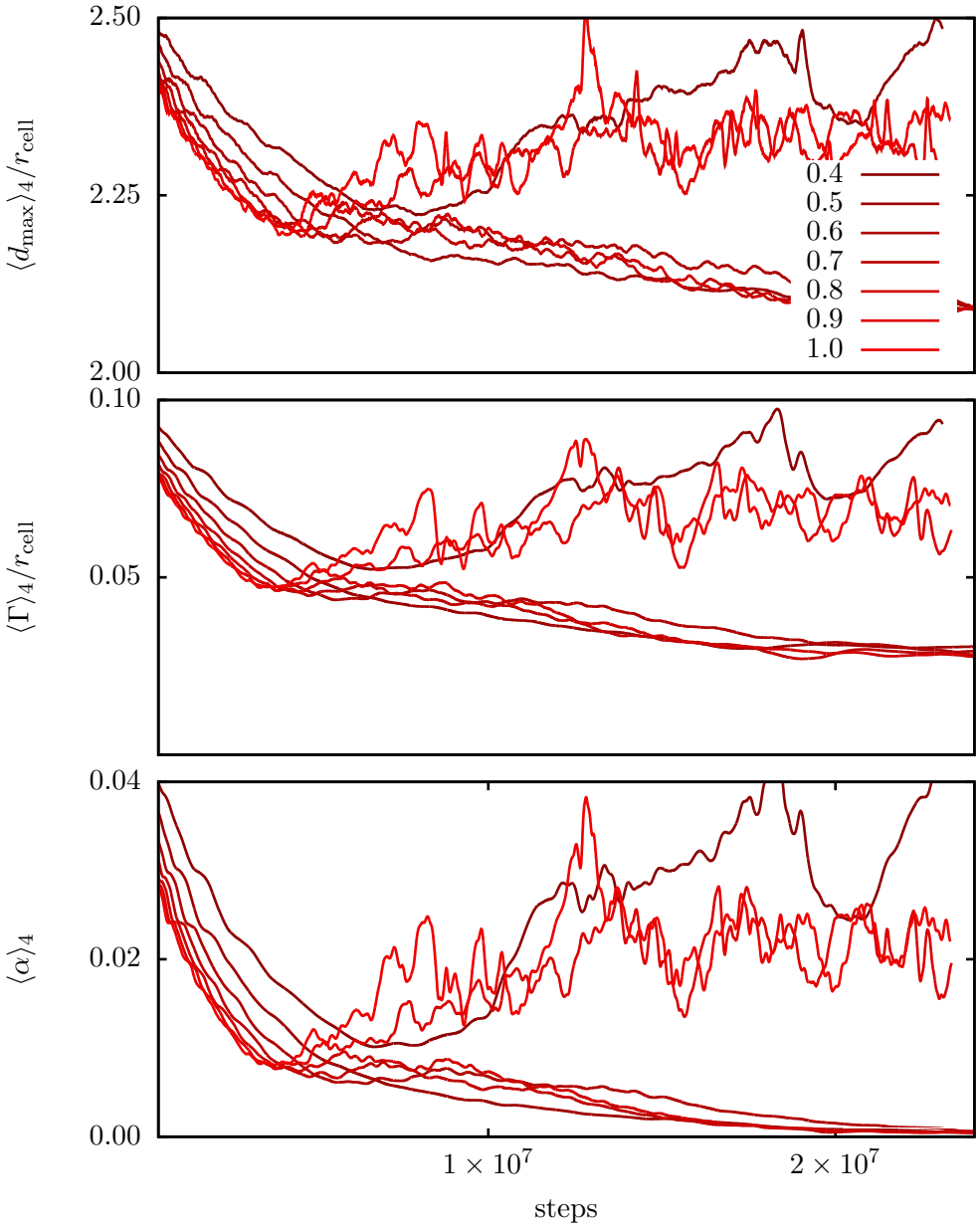

Figure A.5: Series 1: Average deformation of nine cells in a cylinder. Although strongly fluctuating curves, the shear thinning fluid can be seen to cause higher cell deformation on average.

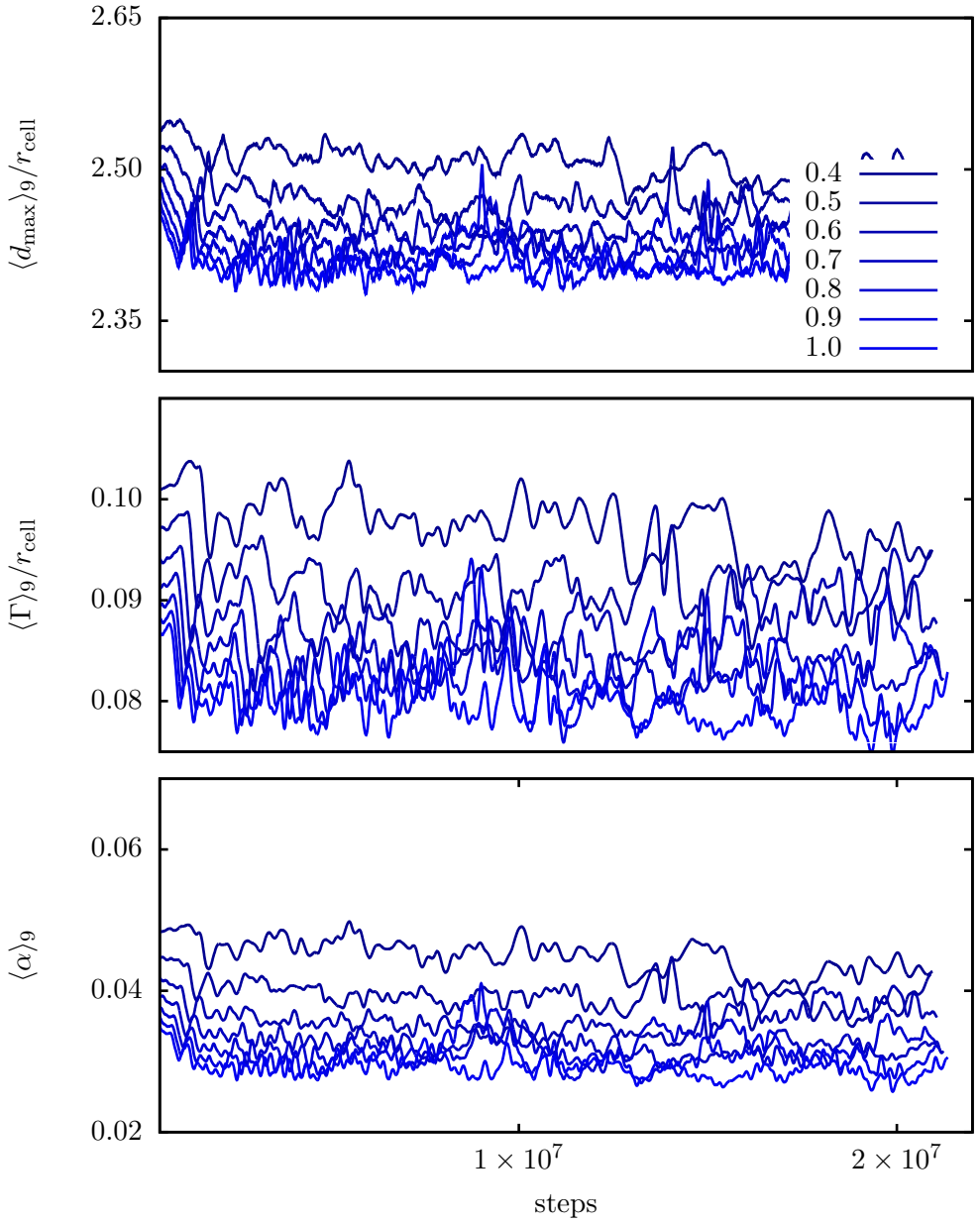

Figure A.6: Series 2: Average deformation of nine cells in a cylinder. Basically the same behavior as in fig. A.5.

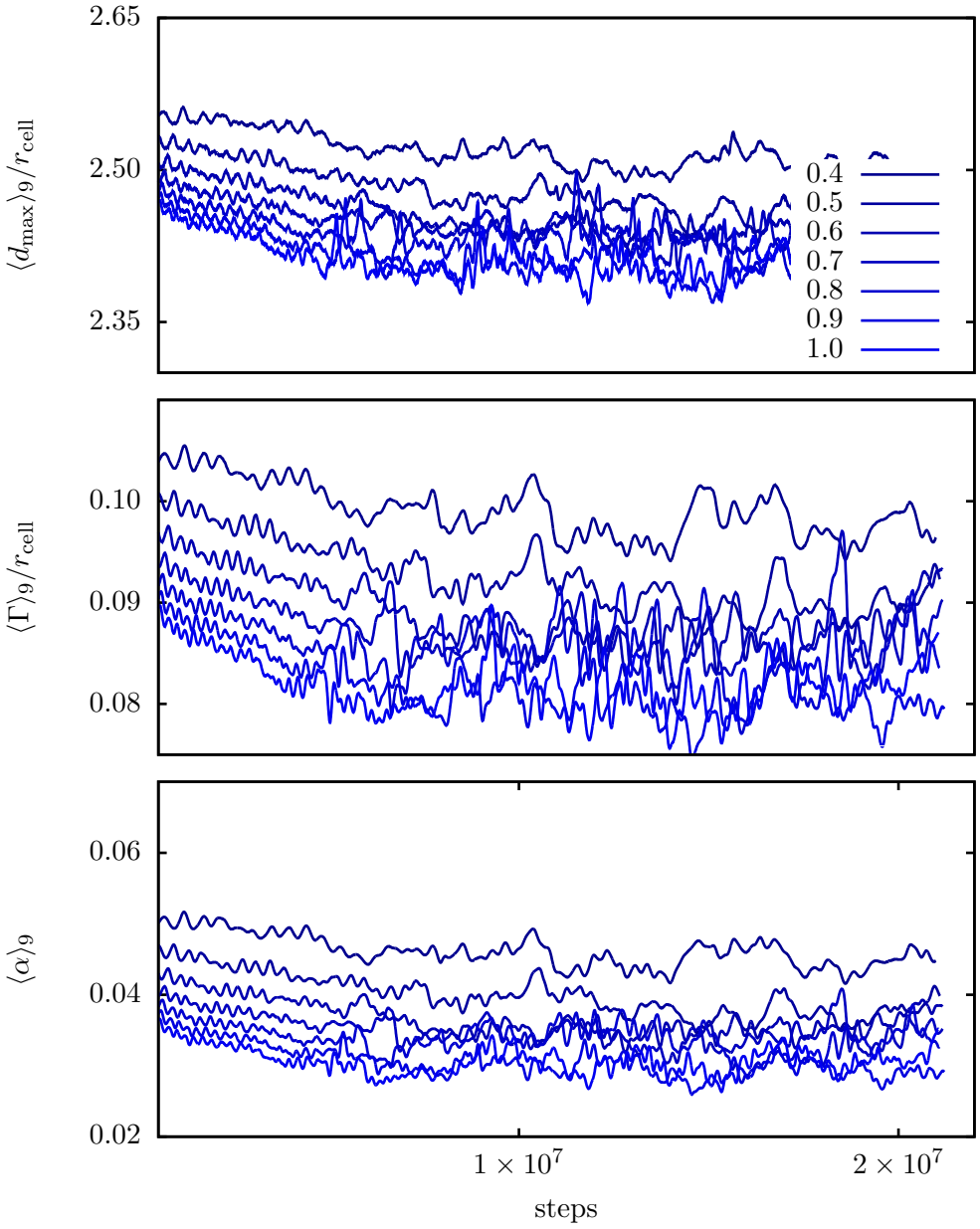

Figure A.7: Series 3: Average deformation of nine cells in a cylinder. Due to the special initial positions, the cells line up at fixed radial offset an maintain this state through the simulation. This causes the deformation data to be significantly less noisy than in the other two series. Consequently, it can be distinctly seen that the deformation is higher for stronger shear thinning fluid for all analysis methods.

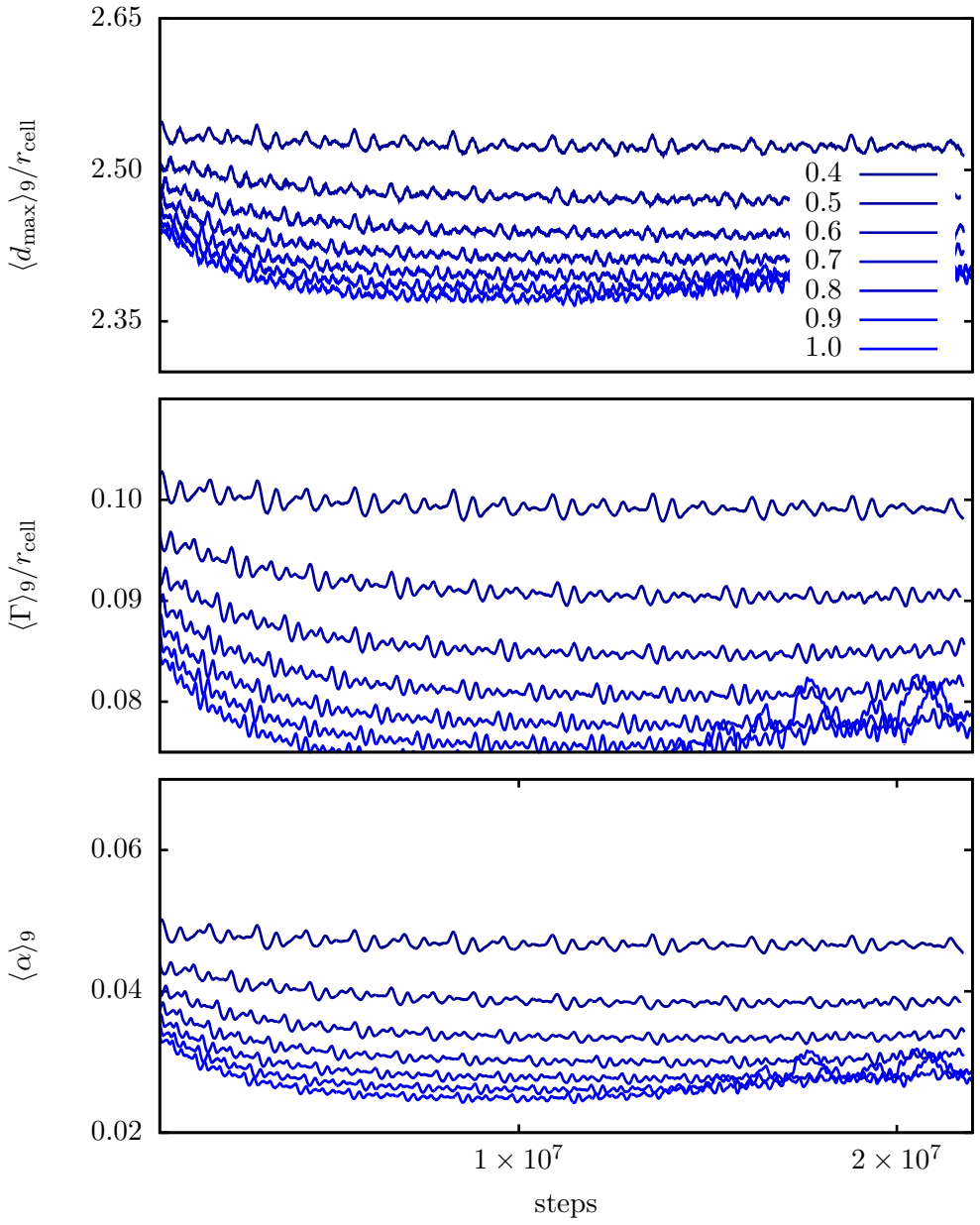

List of Figures

List of Tables

References

[1] *ESPResSo*. ESPResSo - Extensible Software Package for Research on Soft Matter. URL: espressomd.org (accessed on 08/29/2018).

[2] *ParaView*. ParaView. URL: www.paraview.org (accessed on 08/29/2018).

[3] *GIMP*. GNU Image Manipulation Program. URL: www.gimp.org (accessed on 08/29/2018).

[4] *Gnuplot*. Gnuplot homepage. URL: http://gnuplot.info/ (accessed on 08/29/2018).

[5] I. Donderwinkel et al. "Bio-inks for 3D bioprinting: recent advances and future prospects." In: *Polymer Chemistry* 8.31 (2017), pp. 4451 – 4471. ISSN: 1759-9954, 1759-9962. DOI: 10.1039/C7PY00826K.

[6] J. Gopinathan et al. "Recent trends in bioinks for 3D printing." In: *Biomaterials Research* 22.1 (2018). ISSN: 2055-7124. DOI: 10.1186/s40824-018-0122-1.

[7] T. Krüger et al. *The Lattice Boltzmann Method*. Cham: Springer International Publishing, 2017. ISBN: 978-3-319-44647-9. DOI: 10.1007/978-3-319-44649-3.

[8] L. D. Landau et al. *Fluid mechanics*. 2nd ed., 2nd English ed., rev. Course of theoretical physics v. 6. Oxford, England ; New York: Pergamon Press, 1987. 539 pp. ISBN: 978-0-08-033933-7 978-0-08-033932-0.

[9] K. Walters. *An Introduction to Rheology, Volume 3 (Rheology Series)*. Elsevier Science, 1989. ISBN: 0-444-87140-3.

[10] S. D. Holdsworth. "Applicability of rheological models to the interpretation of flow and processing behaviour of fluid food products." In: *Journal of Texture Studies* 2.4 (1971), pp. 393 – 418. ISSN: 0022-4901, 1745-4603. DOI: 10.1111/j.1745-4603.1971.tb00589.x.

[11] J. Šesták et al. "Simple rheological models of food liquids for process design and quality assessment." In: *Journal of Food Engineering* 2.1 (1983), pp. 35 – 49. ISSN: 02608774. DOI: 10.1016/0260-8774(83)90005-5.

[12] M. A. Rao. *Rheology of fluid and semisolid foods: principles and applications*. 2. ed. Food engineering series. OCLC: 255760007. New York, NY: Springer, 2007. 481 pp. ISBN: 978-0-387-70930-7 978-0-387-70929-1.

[13] G. Viggiani, ed. *Geotechnical Aspects of Underground Construction in Soft Ground*. CRC Press, 2012. ISBN: 978-0-415-68367-8 978-0-203-80358-5. DOI: 10.1201/b12748.

[14] T. Sochi. "Non-Newtonian Rheology in Blood Circulation." In: *arXiv:1306.2067 [physics]* (2013). arXiv: 1306.2067.

[15] H. Giesekus. *Phänomenologische Rheologie. Eine Einführung*. Springer, 1994. ISBN: 3-540-57513-8.

[16] G. Astarita et al. *Principles of non-Newtonian fluid mechanics*. London, New York: McGraw-Hill, 1974. 289 pp. ISBN: 978-0-07-084022-5.

[17] X. Hu et al. "A time-dependent power law viscosity model and its application in modelling semi-solid die casting of 319s alloy." In: *Acta Materialia* 124 (2017), pp. 410 – 420. ISSN: 13596454. DOI: 10.1016/j.actamat.2016.11.031.

[18] T. N. Phillips et al. "Lattice Boltzmann models for non-Newtonian flows." In: *IMA Journal of Applied Mathematics* 76.5 (2011), pp. 790 – 816. ISSN: 0272-4960. DOI: 10.1093/imamat/hxr003.

[19] D. Kehrwald. "Lattice Boltzmann Simulation of Shear-Thinning Fluids." In: *Journal of Statistical Physics* 121.1 (2005), pp. 223 – 237. ISSN: 0022-4715. DOI: 10.1007/s10955-005-5963-z.

[20] C.-H. Wang et al. "A lattice Boltzmann approach for the non-Newtonian effect in the blood flow." In: *Computers & Mathematics with Applications* 62.1 (2011), pp. 75 – 86. ISSN: 0898-1221. DOI: 10.1016/j.camwa.2011.04.051.

[21] S. S. Shibeshi et al. "The Rheology of Blood Flow in a Branched Arterial System." In: *Applied Rheology (Lappersdorf, Germany: Online)* 15.6 (2005), pp. 398 – 405. ISSN: 1617-8106. DOI: 10.1901/jaba.2005.15-398.

[22] C. Pichler et al. "Apparent power-law fluid behavior of vibrated fresh concrete: Engineering arguments based on Stokes-type sphere viscometer measurements." In: *Journal of Non-Newtonian Fluid Mechanics* 240 (2017), pp. 44 – 55. ISSN: 03770257. DOI: 10.1016/j.jnnfm.2016.12.007.

[23] J. Boyd et al. "Analysis of the Casson and Carreau-Yasuda non-Newtonian blood models in steady and oscillatory flows using the lattice Boltzmann method." In: *Physics of Fluids* 19.9 (2007), p. 093103. ISSN: 1070-6631. DOI: 10.1063/1.2772250.

[24] T. Osswald et al. *Polymer rheology: fundamentals and applications*. OCLC: 897338324. Munich Cincinnati: Hanser, 2014. 225 pp. ISBN: 978-1-56990-517-3 978-1-56990-523-4.

[25] S. R. D. Groot et al. *Non-Equilibrium Thermodynamics (Dover Books on Physics)*. Dover Publications, 2011. ISBN: 0-486-64741-2.

[26] R. Zwanzig. *Nonequilibrium Statistical Mechanics*. Oxford University Press, 2001. ISBN: 0-19-514018-4.

[27] S. Harris. *An Introduction to the Theory of the Boltzmann Equation* -. New York: Courier Corporation, 2012. ISBN: 978-0-486-14382-8.

[28] S. Chen et al. "Lattice Boltzmann Method for Fluid Flows." In: *Annual Review of Fluid Mechanics* 30.1 (1998), pp. 329 – 364. ISSN: 0066-4189. DOI: 10.1146/annurev.fluid.30.1.329.

[29] P. L. Bhatnagar et al. "A Model for Collision Processes in Gases. I. Small Amplitude Processes in Charged and Neutral One-Component Systems." In: *Physical Review* 94.3 (1954), pp. 511 – 525. ISSN: 0031-899X. DOI: 10.1103/physrev.94.511.

[30] T. Krüger et al. "Shear stress in lattice Boltzmann simulations." In: *Physical Review E* 79.4 (2009). ISSN: 1539-3755. DOI: 10.1103/physreve.79.046704.

[31] D. d'Humieres et al. "Multiple-relaxation-time lattice Boltzmann models in three dimensions." In: *Philosophical Transactions of the Royal Society A: Mathematical, Physical and Engineering Sciences* 360.1792 (2002), pp. 437 – 451. ISSN: 1364-503X. DOI: 10.1098/rsta.2001.0955.

[32] B. Dünweg et al. "Statistical mechanics of the fluctuating lattice Boltzmann equation." In: *Physical Review E* 76.3 (2007). ISSN: 1539-3755. DOI: 10.1103/physreve.76.036704.

[33] W. Zhang et al. "The computation of strain rate tensor in multiple-relaxation-time lattice Boltzmann model." In: *arXiv:1704.07559 [physics]* (2017). arXiv: 1704.07559.

[34] Z. Chai et al. "Multiple-relaxation-time lattice Boltzmann model for generalized Newtonian fluid flows." In: *Journal of Non-Newtonian Fluid Mechanics* 166.5 (2011), pp. 332 – 342. ISSN: 0377-0257. DOI: 10.1016/j.jnnfm.2011.01.002.

[35] C. S. Peskin. "The immersed boundary method." In: *Acta Numerica* 11 (2002). ISSN: 0962-4929, 1474-0508. DOI: 10.1017/S0962492902000077.

[36] T. Krüger. *Computer Simulation Study of Collective Phenomena in Dense Suspensions of Red Blood Cells under Shear*. Wiesbaden: Vieweg+Teubner Verlag, 2012. ISBN: 978-3-8348-2375-5. DOI: 10.1007/978-3-8348-2376-2.

[37] J. B. Freund. "Numerical Simulation of Flowing Blood Cells." In: *Annual Review of Fluid Mechanics* 46.1 (2014), pp. 67 – 95. ISSN: 0066-4189, 1545-4479. DOI: 10.1146/annurev-fluid-010313-141349.

[38] R. Skalak et al. "Strain Energy Function of Red Blood Cell Membranes." In: *Biophysical Journal* 13.3 (1973), pp. 245 – 264. ISSN: 00063495. DOI: 10.1016/S0006-3495(73)85983-1.

[39] W. Helfrich. "Elastic properties of lipid bilayers: theory and possible experiments." In: *Zeitschrift Fur Naturforschung. Teil C: Biochemie, Biophysik, Biologie, Virologie* 28.11 (1973), pp. 693 – 703. ISSN: 0341-0471.

[40] G. Gompper et al. "Random Surface Discretizations and the Renormalization of the Bending Rigidity." In: *Journal de Physique I* 6.10 (1996), pp. 1305 – 1320. ISSN: 1155-4304, 1286-4862. DOI: 10.1051/jp1:1996246.

[41] A. Guckenberger et al. "On the bending algorithms for soft objects in flows." In: *Computer Physics Communications* 207 (2016), pp. 1 – 23. ISSN: 00104655. DOI: 10.1016/j.cpc.2016.04.018.

[42] U. Seifert. "Configurations of fluid membranes and vesicles." In: *Advances in Physics* 46.1 (1997), pp. 13 – 137. ISSN: 0001-8732, 1460-6976. DOI: 10.1080/00018739700101488.

[43] H. Limbach et al. "ESPResSo—an extensible simulation package for research on soft matter systems." In: *Computer Physics Communications* 174.9 (2006), pp. 704 – 727. ISSN: 00104655. DOI: 10.1016/j.cpc.2005.10.005.

[44] M. Lehmann. "Fast discrete Cell Volume Tracking for Blood Flow Simulations using the Lattice Boltzmann Method." Bachelor thesis. Universität Bayreuth, 2018. 35 pp.

[45] J. Boyd et al. "A second-order accurate lattice Boltzmann non-Newtonian flow model." In: *Journal of Physics A: Mathematical and General* 39.46 (2006), pp. 14241 – 14247. ISSN: 0305-4470. DOI: 10.1088/0305-4470/39/46/001.

[46] Q. Li et al. "Simulation of Power-Law Fluid Flows in Two-Dimensional Square Cavity Using Multi-Relaxation-Time Lattice Boltzmann Method." In: *Communications in Computational Physics* 15.1 (2014), pp. 265 – 284. ISSN: 1815-2406. DOI: 10.4208/cicp.160212.210513a.

[47] C. Pozrikidis, ed. *Modeling and simulation of capsules and biological cells*. Chapman & Hall/CRC mathematical biology & medicine series v. 2. Boca Raton, FL: Chapman & Hall/CRC, 2003. 333 pp. ISBN: 978-1-58488-359-3.

[48] A. Nadim et al. "Confined motion of a long bubble through a power-law fluid." In: *Applied Mathematics Research eXpress* (2006). ISSN: 1687-1200. DOI: 10.1155/amrx/2006/36283.

[49] C. Bächer et al. "Clustering of microscopic particles in constricted blood flow." In: *Physical Review Fluids* 2.1 (2017). ISSN: 2469-990X. DOI: 10.1103/PhysRevFluids.2.013102.

[50] D. A. Fedosov et al. "Deformation and dynamics of red blood cells in flow through cylindrical microchannels." In: *Soft Matter* 10.24 (2014), pp. 4258 – 4267. ISSN: 1744-683X. DOI: 10.1039/c4sm00248b.

Eidesstattliche Erklärung

Ich versichere hiermit an Eides statt, die vorliegende Arbeit selbstständig verfasst und keine als die angegebenen Quellen und Hilfsmittel verwendet zu haben. Die Arbeit wurde nicht bereits in gleicher oder vergleichbarer Form zur Erlangung eines akademischen Grades eingereicht.
Sämtliche Stellen der Arbeit, die anderen Werken im Wortlaut oder dem Sinn nach entnommen sind, wurden durch Quellenangaben kenntlich gemacht. Dies gilt ebenso für Zeichnungen, Skizzen, bildliche Darstellungen und dergleichen sowie für Quellen aus dem Internet.
Des Weiteren versichere ich, dass die digitale und die gedruckte Version inhaltlich identisch sind.

Bayreuth, den 7. September 2018

Sebastian Johannes Müller